2016

Uncertainty Quantification In Computational Catalysis

Eric Alan Walker
University of South Carolina

UNCERTAINTY QUANTIFICATION IN COMPUTATIONAL CATALYSIS

by

Eric Alan Walker

Bachelor of Science
Georgia Institute of Technology, 2009

Master of Science
University of South Carolina, 2013

Submitted in Partial Fulfillment of the Requirements

For the Degree of Doctor of Philosophy in

Chemical Engineering

College of Engineering and Computing

University of South Carolina

2016

Accepted by:

Andreas Heyden, Major Professor

Gabriel A. Terejanu, Committee Member

Jochen Lauterbach, Committee Member

Mark Uline, Committee Member

John Weidner, Committee Member

Salai Cheettu Ammal, Committee Member

Cheryl L. Addy, Vice Provost and Dean of The Graduate School

DEDICATION

To Elina (Eleni Kyriakidou), my wife. You helped me with this dissertation in countless ways for which I am eternally grateful.

ACKNOWLEDGEMENTS

I acknowledge Dr. Heyden for his unwavering guidance. I acknowledge Dr. Terejanu for his resolute support and mentorship. I acknowledge the Heyden research group members including Salai, Sina, Faheem, Jianmin, Mamun, Vijay, Saleheen, Asif and Wenqiang and Terejanu group member Xiao. On a personal note, I acknowledge Elina, Mom and Dad. Also, I would like to acknowledge my best man, Ioannis Sgouralis and friend Carl Frisby.

ABSTRACT

This dissertation augments the field of computational catalysis with uncertainty quantification. An efficient tool to describe the energetics and structure of atomistic systems is density functional theory (DFT). DFT may be used to understand how catalysts work although DFT is inexact in nature due to approximations necessary for computational tractability. These approximations in DFT cause uncertainty in microkinetic model results for catalytic systems. Therefore, reliable model results gained from DFT include a quantification of uncertainty. The case study to examine a systematic framework for uncertainty quantification is water-gas shift (WGS $CO+H2O \rightleftharpoons CO2+H2$) reaction by $Pt/TiO2$ catalyst.

Uncertainties are represented with probabilities and a latent variable model is developed that account for errors and correlations in DFT energies. This probabilistic model is further constrained to known reaction thermodynamics, and then propagated to quantities of interest such as turnover frequency (TOF), apparent activation barrier, and reaction orders. DFT energies are obtained using four separate functionals PBE, RPBE, HSE, and M06L that each have their own justification for being appropriate for this study. Although the uncertainty in model results spans orders of magnitude, a new approach is introduced to identify the dominant catalytic cycle under uncertainty. Next three active sites of the Pt/TiO_2 catalyst are compared using uncertainty and Bayesian statistics to find which active site best explains experiments. Of the three active sites,

two involve the oxide support (TiO_2) in the mechanism of reaction. The third active site models only the metal with Pt(111). The two active sites involving the oxide support both explain the experimental data far better than the terrace Pt(111) active site. Therefore, it is concluded that the oxide support plays a mechanistic role in the WGS reaction. The selected active site is verified with separate experiments at separate pressure and temperature conditions

TABLE OF CONTENTS

LIST OF TABLES

LIST OF FIGURES

CHAPTER 1

INTRODUCTION

This dissertation is written in manuscript style. Therefore each chapter is a publication. The first publication, chapter 2, is a theoretical investigation of a fuel cell anode. This work was supported by the Energy Frontiers Research Center at the University of South Carolina. Specifically, the work investigates the mechanism of sulfur poisoning of a perovskite anode material of a solid oxide fuel cell. The model of the perovskite material has been developed in large part in the publications of Dr. Suwit Suthirakun and Dr. Salai Ammal and the dissertation of Dr. Suthirakun.

The second and third publication (the third publication is to be submitted) are at the heart of the title of this dissertation, uncertainty quantification. We use an industrially-relevant water-gas shift reaction for producing hydrogen as a case study. The second publication, chapter 3, deals with the *forward problem* in which we have some uncertainties in our model predictions. The third publication deals with an *inverse problem* in which experiments are used to update our model uncertainties. The inverse problem also helps us to select the atomistic-scale active site of the nano-particle catalyst. These publications were supported by the National Science Foundation CAREER award won by Dr. Andreas Heyden and the research in these publications also led to the Designing Materials to Revolutionize and Engineer our Future grant won by Drs. Heyden, Terejanu and Ammal

CHAPTER 2

MECHANISM OF SULFUR POISONING OF $SR_2FE_{1.5}MO_{0.5}O_{6-\delta}$ PEROVSKITE ANODE UNDER SOLID OXIDE FUEL CELL CONDITIONS[1]

[1]Walker, E.; Ammal, S. C.; Suthirakun, S.; Chen, F.; Terejanu, G. A.; Heyden, A. *J. Phys. Chem. C*, **2014**, 118, 23545–23552.

Reprinted here with permission of publisher.

2.1 ABSTRACT

The interactions between sulfur and the $Sr_2Fe_{1.5}Mo_{0.5}O_{6-\delta}$ (SFMO) perovskite anode are investigated using periodic density functional theory (DFT) calculations and constrained ab initio thermodynamic analysis under anodic solid oxide fuel cell conditions. Three surface models with different Fe:Mo ratios in the topmost layer are used to investigate the mechanism of sulfur poisoning. Sulfur prefers to interact with these surfaces by replacing existing oxygen rather than adsorbing on a metal or oxygen vacancy. Constructed phase diagrams suggest that the surface with higher Mo content on the gas exposed surface layer is highly resistant toward sulfur poisoning, whereas the FeO_2-terminated surface is more susceptible to sulfur poisoning. The presence of S in the surface has also a negative impact on the surface vacancy formation process, which is the rate-controlling step in the H_2 electro-oxidation. Adding a small Ni_3 cluster to the least active FeO_2-terminated surface promotes the oxygen vacancy formation; however, the presence of strongly adsorbed S on the Ni cluster makes this process more endergonic, which in turn will decrease the activity of the anode. Based on these results, we suggest that increasing the Mo content in the gas exposed surface layer of SFMO will improve its overall electrochemical performance while maintaining excellent sulfur tolerance.

2.2 INTRODUCTION

Over the past decade, the search for clean, renewable, and sustainable energy has moved from the periphery to the center of the global economy. Solid oxide fuel cells (SOFCs) have great potential to be the cleanest, most efficient, and versatile system for

future energy conversion because they can convert energy more efficiently than conventional heat engine systems and lower temperature polymer-based fuel cells. The capability of SOFCs to operate with a wide range of gas fuels as well as the possibility of direct utilization (or through internal reforming) of conventional fossil, biomass, and other renewable fuels facilitates SOFC's application in environmentally friendly industries.[1−5] However, a major drawback of such readily available fuels is the presence of sulfur-containing impurities, which may poison the catalytically active metal sites at the anode and thus, seriously affect the cell performance and even operational life.[6−8] During the reforming process, the sulfur compounds are converted to gaseous H2S and the most commonly used Ni-based anodes in the current SOFC systems display very poor tolerance to H2S. Significant poisoning of Ni-anodes was observed when the H2S concentration was above 5−10 ppm at 950−1000 °C and the extent of poisoning increased dramatically at lower temperatures.[7,9,10] Therefore, great efforts have been devoted to understanding the sulfur poisoning mechanism of SOFC anodes in recent years[11−17] in order to identify specific mitigation strategies against degradation and for the rational design of sulfur tolerant anodes.

In addition to the efforts made to improve the sulfur tolerance of conventional Ni based anodes, recent studies have also focused on finding alternative anode materials with improved sulfur tolerance. Among them, the mixed ionic and electronic conductor (MIEC) oxides with perovskite structure have drawn significant interest for the development of high performance sulfur tolerant anodes. Recently, the $Sr_2Fe_{1.5}Mo_{0.5}O_{6-\delta}$ (SFMO) perovskite has been proven to be an extremely efficient anode for SOFCs because it exhibits chemical compatibility with the electrolyte and under reducing

conditions, good catalytic activity, and very good ionic and electrical conductivity.[18−23] Experimental studies have shown that the SFMO anode can process both H_2 fuel and natural gas with high tolerance to sulfur.[18,19,22] Despite these advantages, a major drawback of SFMO was identified in its relatively low electro-oxidation activity, leading to an overall low cell performance. It has been shown that adding a small amount of Ni to the anode improves the overall cell performance, indicating that Ni has an electrocatalytic effect toward fuel oxidation on the SFMO surface.[19,23] However, the presence of Ni decreases the sulfur tolerance of SFMO and the cell performance of Ni−SFMO anode was found to drop by almost 18% after operating for about 20 h in a H_2 fuel with 100 ppm of H_2S at 800 °C.[23] Thus, a compromise between improved activity and sulfur tolerance of the SFMO anode has not yet been achieved.

In our recent study, we investigated the electro-oxidation mechanism of H_2 fuel on the SFMO (001) surface under SOFC operating conditions using periodic density functional theory (DFT) calculations and microkinetic modeling techniques.[24] We found that Mo plays a crucial role in improving the catalytic activity of SFMO; however, the Mo content in the SFMO surface tends to be very low under fuel cell operation conditions. On the basis of our results, we suggested that increasing the Mo content in the surface could possibly improve the overall electrochemical performance of SFMO. Herein, we investigate the sulfur poisoning mechanism of SFMO (001) surfaces with different Mo content under fuel cell operating conditions using constrained ab initio thermodynamics calculations. We aim at identifying the mechanism of S adsorption on the SFMO (001) surface and its effect on the rate-limiting step of the H_2 electrooxidation. We find that Mo not only promotes the catalytic activity as identified in our earlier

work,[24] but also dramatically improves the sulfur tolerance of the SFMO anode. However, in the presence of Ni clusters on the surface, added to promote the rate-limiting oxygen vacancy formation process, the activity will decrease with time due to Ni's strong affinity for sulfur atoms.

2.3 COMPUTATIONAL MODEL AND METHODS

All calculations presented in this work were carried out using spin-polarized DFT+U theory with periodic boundary conditions as implemented in the Vienna Ab initio Simulation Package (VASP).[25,26] The semilocal generalized gradient approximation density functional of Perdew, Burke, and Ernzerhof (PBE)[27] was used to describe exchange and correlation effects. The nuclei and core electronic states were described by projector augmented-wave (PAW) potentials,[28] while the Sr 4s4p5s, Fe 3p3d4s, Mo 4p5s4d, Ni 4s3d, O 2s2p, and S 3s3p were treated as valence electrons. The PAW−DFT wave functions are expanded in a plane wave basis, with a kinetic energy cutoff of 800 eV and a k-point sampling based on the Monkhorst-pack (MP)[29] scheme. Integration over the first Brillouin zone used Gaussian smearing (σ = 0.05 eV) during structural relaxations. The U−J parameter was employed to correct the self-interaction error inherent in pure DFT when applied to transition metals with tightly localized d-electrons, such as Fe in SFMO. In accordance with earlier computational studies on SFMO,[20,30] we set the U−J value for Fe to 4.0 eV and used no U−J parameter for Mo, as validated on the parent SrFeMoO6 compound.

The three SFMO (001) surface models, referred as plane-Mo,diagonal-Mo, and FeO_2^- terminated surface, used to investigate sulfur poisoning mechanism are shown in Figure 2.1. We chose these surface models based on our previous constrained ab initio thermodynamic analysis on the stability of SFMO surface models under fuel cell operating conditions. The details of these calculations can be found elsewhere.[24] The number of Mo atoms in the top surface layer of the plane-Mo, diagonal-Mo, and FeO_2^- terminated surfaces are 2, 1, and 0, respectively. Our thermodynamic analysis[24] suggested that all three surface models possess five oxygen vacancies at relevant SOFC operating conditions ($P_{O2} = 10^{-20}$, T = 1100 K); however, the distribution of vacancy sites is different in the three models. The plane-Mo surface (Figure 2.1a) has two oxygen vacancies in the topmost layer, whereas the diagonal-Mo (Figure 2.1b) surface has three oxygen vacancies, and the FeO_2^- terminated (Figure 2.1c) surface contains four oxygen vacancies in the topmost layer.

Each SFMO (001) slab has four SrO and four $Fe(Mo)O_2$ layers and is terminated by a $Fe(Mo)O_2$ layer. As reported previously,[24] the antiferromagnetic arrangement of Fe spins was found to be the most stable arrangement in all the three surface configurations. A vacuum gap of 15 Å was used to minimize the interaction between images along the z-axis. The bottom-most layer was fixed in all calculations to mimic a semi-infinite bulk crystal and the slabs were optimized using a $4 \times 4 \times 1$ MP[29] k-mesh. Dipole and quadrupole corrections to the energy are taken into account using a modified version of the Markov and Payne method;[31] i.e., the contribution of dipole interactions along the z-axis is subtracted from the total energy.

2.4 RESULTS AND DISCUSSION

Since sulfur compounds present in hydrocarbon fuels are converted to gaseous H_2S during reforming and the adsorption of a sulfur atom on the SFMO surface can be described as $H_2S_{(g)} + * \leftrightarrow H_{2(g)} + S^*$, where * represents an empty site on the SFMO surface and S* is the adsorbed sulfur atom. On the three surface models considered in the present study (Figure 2.1), the adsorption site for a sulfur atom could either be on top of a Mo or Fe atom as well as on the existing oxygen vacancy site ($M - V_O^{\bullet\bullet} - Fe,\ M = Mo$ or Fe in Kröger−Vink notation[32]). Our calculations suggested that the adsorption of S is favored on the oxygen vacancy site in all three surface models. The initial structures with S on top of a Mo or Fe atom converged to the structures with S in the vacancy site because each Mo and Fe atom in the three surface models has a neighboring oxygen vacancy. Thus, we describe the S adsorption reaction on the reduced SFMO (001) surface as

$$H_2S_{(g)} + M - V_O^{\bullet\bullet} - Fe \leftrightarrow H_{2(g)} + M - S - Fe,\ (M = Mo\ or\ Fe) \qquad (1)$$

and the corresponding adsorption reaction energy (ΔE^{ads}) is then given by

$$\Delta E^{ads} = E_{H2}^{DFT} + E_{M-S-Fe}^{DFT+U} - E_{H2S}^{DFT} - E_{M-V_O^{\bullet\bullet}-Fe}^{DFT+U} \qquad (2)$$

where $E_{M-V_O^{\bullet\bullet}-Fe}^{DFT+U}$ and E_{M-S-Fe}^{DFT+U} correspond to the computed energy of the surface model before and after S adsorption, respectively. In addition to the adsorption of S atom on the SFMO surface, we have also considered the possibility of S replacing an oxygen atom on

the surface. This reaction can be described as

$$H_2S_{(g)} + M - O - Fe \leftrightarrow H_2O_{(g)} + M - S - Fe, \ (M = Mo \ or \ Fe) \quad (3)$$

and the corresponding replacement reaction energy (ΔE^{repl}) is then given by

$$\Delta E^{repl} = E_{H2O}^{DFT} + E_{M-S-Fe}^{DFT+U} - E_{H2S}^{DFT} - E_{M-O-Fe}^{DFT+U} \quad (4)$$

where E_{M-O-Fe}^{DFT+U} and E_{M-S-Fe}^{DFT+U} correspond to the energy of the surface model before and after O replacement by S, respectively. We note here that for a particular surface model, e.g. plane-Mo surface, the product structures of $M - S - Fe$ described in eqns. (1) & (3) and the corresponding energies described in eqns. (2) & (4) are different due to the adsorption and replacement happening at different sites. However, the reactant structures of $M - V_O^{\bullet\bullet} - Fe$ and $M - O - Fe$ described in eqns. (1) & (3) and the corresponding energies described in eqns. (2) & (4) are the same because they only represent different active sites on the same surface model. The optimized structures of S adsorbed on the oxygen vacancy and S replacing an oxygen atom on the three surface models and their corresponding reaction energies are provided in Figure 2.2. The three SFMO surface models not only differ in number of Mo/Fe atoms and oxygen vacancy concentration on the surface layer, they also possess different oxygen vacancy types such as, $Mo - V_O^{\bullet\bullet} - Fe$ and $Fe - V_O^{\bullet\bullet} - Fe$. The plane-Mo surface has only $Mo - V_O^{\bullet\bullet} - Fe$ type oxygen vacancies and FeO_2- terminated surface has only $Fe - V_O^{\bullet\bullet} - Fe$ type oxygen vacancies. However, the diagonal-Mo surface has both types of oxygen vacancies on the surface layer.

Our calculations suggest that the adsorption of S on the $Fe - V_O^{\bullet\bullet} - Fe$ vacancy of FeO_2- terminated surface and diagonal-Mo surface is energetically more favorable than on the $Mo - V_O^{\bullet\bullet} - Fe$ vacancy of plane-Mo surface by -0.49 eV and -0.70 eV, respectively. The adsorption of S on the $Mo - V_O^{\bullet\bullet} - Fe$ vacancy of diagonal-Mo surface is even less favorable than the plane-Mo surface by 0.39 eV. We note here that when S is adsorbed on the $Mo - V_O^{\bullet\bullet} - Fe$ vacancy of plane-Mo surface it forms a stronger bond with Fe (d_{Fe-S} = 2.26 Å) and a weaker bond with Mo (d_{Mo-S} = 2.51 Å). On the diagonal-Mo surface the S atom is mostly bonded to Mo (d_{Mo-S} = 2.17 Å) without any interaction with Fe and thus becomes the least stable structure compared to all the other S adsorbed structures. These results suggest that the Fe atoms have strong tendency to adsorb S atoms while Mo seems to exhibit some resistance towards S adsorption. Although the dissociative adsorption at the most favorable $Fe - V_O^{\bullet\bullet} - Fe$ vacancy site seems to be stronger on the SFMO surfaces, the adsorption energies (-0.61 and -0.82 eV) are still lower than the S adsorption energies reported for Ni (100) and Ni (111) surfaces. Wang and Liu[33] calculated the dissociative adsorption of H_2S on Ni surfaces using PBE functional and reported that the adsorption energy ranges from -2.64 eV to -2.16 eV on Ni (100) surface and from -1.96 eV to -1.10 eV on Ni (111) surface when the surface coverage of S is between 0.063 to 0.5 ML. Thus the SFMO surface is expected to be less prone to sulfur poisoning than the conventional Ni based anodes.

Comparison of oxygen replacement reaction energies on the three surfaces also reveal the same trend as dissociative adsorption energies, i.e., replacing $Fe - O - Fe$ type oxygen by S on the FeO_2- terminated and diagonal-Mo surfaces are more favorable

than replacing $Mo - O - Fe$ type oxygen on the plane-Mo and diagonal-Mo surfaces. In order to examine the stability of the adsorbed S atom on the SFMO surface either via adsorption reaction or oxygen replacement reaction under fuel cell operating conditions, we calculated the Gibbs free energies of these reactions which includes the entropy contributions for gas molecules and allow us to make a direct comparison between these two reactions on each surface model. The environmental effects at fuel cell operating conditions can be taken into consideration by calculating the Gibbs free energy $G(T,P)$ of the reactants and products as a function of temperature (T) and pressure (P) from the DFT+U results using ab initio atomistic thermodynamic method. The change in Gibbs free energy (ΔG) of reactions (1) and (3) can be written as:

$$\Delta G^{ads} = G_{H2(g)} + G_{M-S-Fe} - G_{H2S(g)} - G_{M-V_O^{\bullet\bullet}-Fe} \quad (5)$$

$$\Delta G^{repl} = G_{H2O(g)} + G_{M-S-Fe} - G_{H2S(g)} - G_{M-O-Fe} \quad (6)$$

where the Gibbs free energies of the oxide surfaces (G_{M-O-Fe}, $G_{M-V_O^{\bullet\bullet}-Fe}$, and G_{M-S-Fe}) have relatively small variation with environmental effects and can be approximated by the energies computed by DFT+U. On the contrary, the Gibbs free energy of the gas phase molecules will be strongly affected by temperature (T) and pressure (P) and is calculated using

$$G_{(g)}(T,P) = E_{gas}^{DFT} + \Delta\mu_{gas}(T,P^0) + k_B T ln\left(\frac{P}{P^0}\right) \quad (7)$$

where $\Delta\mu_{gas}(T, P^0)$ can be calculated from the rotational, translational, and vibrational partition functions of the gas molecule as a function of temperature under atmospheric pressure (P^0 = 1 atm). The pressure dependent contribution is provided in the third term of eqn. (7). Since the surface structure is modified in the oxygen replacement reaction (3), vibrational effects on the surface free energy would be important and thus we calculated the vibrational free energy of the SFMO surfaces before and after S adsorption and replacement reactions by considering few vibrational modes around the active site. The active site (M-O-Fe or M-S-Fe) atoms and the neighboring oxygen atoms that are directly connected to the active site are included in the frequency calculations. Displacements of ±0.001 Å were used along the x, y and z directions for all Hessian constructions from analytic gradients. The vibrational free energy ($F^{vib}(T)$) within the harmonic approximation for *n* fundamental modes (with frequencies of ω_i) of the system can be expressed as:

$$F^{vib}(T) = \sum_{i=1}^{n}\left[\frac{1}{2}\hbar_{\omega i} + k_B T ln\left(1 - exp\left(\frac{-\hbar_{\omega i}}{k_B T}\right)\right)\right] \quad (8)$$

Thus the variation of Gibbs free energy for the adsorption and replacement reactions shown in eqns. (5) and (6) can be rewritten as,

$$\Delta G^{ads}(T, P) = \left(E_{H2}^{DFT} + \Delta\mu_{H2}(T, P^0)\right)$$

$$+\left(E_{M-S-Fe}^{DFT+U} + F_{M-S-Fe}^{vib}(T)\right)$$

$$-\left(E_{H2S}^{DFT} + \Delta\mu_{H2S}(T, P^0)\right)$$

$$- \left(E_{M-V_O^{\bullet\bullet}-Fe}^{DFT+U} + F_{M-V_O^{\bullet\bullet}-Fe}^{vib}(T)\right)$$

$$+ k_B T ln\left(\frac{P_{H_2}}{P_{H2S}}\right) \quad (9)$$

$$\Delta G^{repl}(T, P) = \left(E_{H2O}^{DFT} + \Delta\mu_{H2O}(T, P^0)\right)$$

$$+ \left(E_{M-S-Fe}^{DFT+U} + F_{M-S-Fe}^{vib}(T)\right)$$

$$-\left(E_{H2S}^{DFT} + \Delta\mu_{H2S}(T, P^0)\right)$$

$$- \left(E_{M-O-Fe}^{DFT+U} + F_{M-O-Fe}^{vib}(T)\right)$$

$$+ k_B T ln\left(\frac{P_{H2O}}{P_{H2S}}\right) \quad (10)$$

The calculated reaction free energies using eqns. (9) and (10) at a representative temperature of 1100 K and assuming the partial pressure of gas molecules as 1 atm are provided in Table 2.1. The pressure dependence of these reaction free energies are displayed in the phase diagrams (Figure 2.3, $\Delta G = 0$ – curve) which illustrate the stability of the S atom on the three SFMO surfaces as a function of temperature and pressure. The reaction free energies provided in Table 2.1 suggest that the dissociative adsorption of H_2S on the $Mo - V_O^{\bullet\bullet} - Fe$ site is endergonic at high temperatures whereas on the $Fe - V_O^{\bullet\bullet} - Fe$ site it is still favorable. Comparison of adsorption and oxygen

replacement reaction free energies on each surface suggests that the replacement reaction is more favorable than the adsorption reaction and the oxygen replacement is exergonic on all the surfaces at 1100 K.

The constructed phase diagram (Figure 2.3a) using eqn. (9) indicates that the dissociative adsorption of H_2S on the SFMO surface is favorable only when the H_2S concentration in the fuel stream is above 10^4 ppm at temperatures above 1000 K (P_{H2} = 1 atm). Considering that the H_2S concentration in most fuel sources is below 300 ppm,[11] we can eliminate the possibility of poisoning the SFMO surface by dissociative adsorption of H_2S. In the phase diagram of oxygen replacement reaction (Figure 2.3b) the $\Delta G = 0$ curves are plotted against the partial pressure ratio of H_2S and H_2O. In a typical H_2 oxidation process at SOFC anodes H_2O concentration in the fuel stream is only about 3%.[23,34] Assuming P_{H2O} = 0.03 atm, Figure 2.3b suggests that replacing Mo-O-Fe type oxygen by S is favorable only at high concentration of H_2S (>10^3 ppm) in the temperature range (900 – 1300 K) considered here. On the other hand, replacing Fe-O-Fe type oxygen by S on the diagonal-Mo surface becomes feasible when the H_2S concentration is > ~200 ppm at 1100 K and only need about 46 ppm of H_2S at 900 K. In correlation with the reaction free energies provided in Table 2.1, the FeO_2- terminated surface is more prone to S poisoning than the diagonal-Mo surface. On this surface, the replacement reaction becomes exergonic when the H_2S concentration increases above 17 ppm and 88 ppm at temperatures 900 K and 1100 K, respectively. However, this amount is still higher than the H_2S concentration required for poisoning the Ni anodes. Matsuzaki and Yasuda investigated the poisoning effect of sulfur-containing impurity on the electrochemical oxidation of H_2 at the interface of Ni-YSZ cermet electrode and reported that the

polarization resistance and the overvoltage of the electrode increased when the H_2S concentration exceeded 0.05, 0.5, and 2 ppm at 1023, 1173, and 1273 K, respectively.[7] Thus our computational results suggest that the SFMO electrodes in general are less susceptible to sulfur poisoning compared to the conventional Ni based electrodes and increasing the Mo concentration on the SFMO surface could further improve the resistance towards sulfur poisoning.

Next, we examined the effect of the presence of sulfur in the SFMO surface on its ability to electrochemically oxidize H_2. In our recent work, we investigated various pathways of the electrooxidation of H_2 at different active sites on the three SFMO surfaces.[24] Our analysis based on periodic DFT and microkinetic modeling techniques revealed that at relevant operating voltages and reaction conditions, H_2O desorption which produces surface oxygen vacancies is rate controlling for H_2 oxidation on SFMO surfaces. Thus, we were able to relate the activity of these surfaces to their ability to form surface oxygen vacancies under SOFC operating conditions. The calculated current densities on the three surfaces correlated well with the Gibbs free energies of the reaction, $M - O - Fe + H_{2(g)} \leftrightarrow M - V_O^{\bullet\bullet} - Fe + H_2O_{(g)}$, $(M = Mo\ or\ Fe)$. The correlation revealed that the surface with higher Mo concentration on the gas exposed layer (plane-Mo) has lower oxygen vacancy formation energy which in turn exhibited higher activity towards H_2 electrooxidation. On the other hand, the most stable FeO_2^- terminated surface has higher oxygen vacancy formation energy and lower activity towards H_2 electrooxidation. In our current analysis, we identified that the plane-Mo surface which exhibited higher activity is also less susceptible to sulfur poisoning and the least active FeO_2- terminated surface is more susceptible to sulfur poisoning. In order to

understand the effect of sulfur on the rate controlling surface vacancy formation process on the FeO_2- terminated surface, we calculated the Gibbs free energies of vacancy formation process in the presence of S by considering various active sites as shown in Table 2.2. The corresponding reactant structures and the exact oxygen/sulfur atom that is removed to form a vacancy are illustrated in Figure 2.4. The reaction (a) in Table 2.2 corresponds to the surface vacancy formation process at $Fe-O-Fe$ site on a clean FeO_2- terminated surface. In reaction (b), we assume that H_2 oxidation occurs at the active site ($Fe-S-Fe$) where the oxygen atom is already replaced by S and in reaction (c) we examine the effect of S on H_2 oxidation at a neighboring $Fe-O-Fe$ site. The calculated Gibbs free energies of both reactions (b) & (c) are higher than the vacancy formation free energy (1.07 eV)[24] in the absence of sulfur (a). The free energy of reaction (b) is 0.61 eV higher than the free energy of H_2 oxidation at $Fe-O-Fe$ site, suggesting that the rate of H_2 oxidation at $Fe-S-Fe$ site will be much smaller than that of $Fe-O-Fe$ site. When S is present on the surface, the free energy of H_2 oxidation at a neighboring $Fe-O-Fe$ site is also about 0.1 eV higher than the free energy in the absence of S. Thus in the presence of S, H_2 oxidation rate at a neighboring $Fe-O-Fe$ site will be at least an order of magnitude lower than the surface without any adsorbed S.

In our earlier work,[24] we have also shown that the oxygen vacancy formation free energy of FeO_2- terminated surface is greatly reduced in the presence of one and two Ni adatoms. In accordance with experimental reports,[19,23] these results suggested that Ni improves the catalytic activity of SFMO anode by promoting the rate controlling oxygen vacancy formation process. However, the experimental studies also observed a drop in

cell performance of Ni-SFMO anodes with time while operating in H_2 fuel with 100 ppm H_2S.[23] To further understand the detrimental effect of H_2S on the Ni-SFMO anode performance, we calculated the oxygen vacancy formation free energies of the FeO_2-terminated surface with a Ni_3 cluster on top, both in the presence and absence of adsorbed sulfur on Ni. The calculated free energies are provided in Table 2.3 (reactions d & e) and the optimized structures are shown in Figures 2.4d & 2.4e. In the presence of Ni_3 cluster, the oxygen vacancy formation free energy is calculated as 0.14 eV which is 0.93 eV smaller than the clean surface. Next, we examined the effect of S on the vacancy formation free energy of Ni_3/SFMO surface. It is well known that the dissociative adsorption of H_2S is highly favorable on Ni surfaces.[33,35,36] Our calculations also suggest that the reaction energy (ΔE^{ads}) for the dissociative adsorption of H_2S on the Ni_3 cluster is as high as -2.88 eV. This adsorption energy is higher than the reported dissociative adsorption energies of H_2S for Ni (100) ($\Delta E^{ads} = -2.64\ eV$) and Ni (111) ($\Delta E^{ads} = -1.96\ eV$) at low coverage of S.[33] This is not surprising considering that the Ni atoms in the adsorbed Ni_3 cluster are highly under-coordinated than the surface Ni atoms. The high adsorption energy calculated for the Ni_3 cluster suggests that the adsorbed S atom will be stable at SOFC operating conditions even in the presence of <2 ppm of H_2S. When S is adsorbed on the Ni_3 cluster, the vacancy formation free energy was calculated to be 0.74 eV which is 0.70 eV higher than the reaction free energy in the absence of adsorbed S (Table 2.2). Thus, in agreement with experimental results[23] these calculations confirm that although Ni promotes the catalytic activity of SFMO anode by facilitating the surface oxygen vacancy formation process, the activity will decrease with time due to the strong adsorption of sulfur on Ni. On the other hand, the plane-Mo surface with higher Mo

concentration on the gas exposed layer not only exhibits higher catalytic activity (without a need for additional Ni particles) but also shows high resistance to sulfur poisoning.

A better understanding of the detrimental effect of sulfur on the FeO_2- terminated surface both in the presence and absence Ni cluster can be obtained by analyzing the electron density of these surfaces by computing Bader charges.[37,38] These charges provided in Table 2.3 can yield a qualitative picture of the reorganization of the electron density upon adsorption of metal atoms or removal of neutral oxygen/sufur atom. In our earlier work,[24] we have identified that all the Fe atoms on the FeO_2- terminated surface ($Sr_{16}Fe_{12}Mo_4O_{43}$) layer are in Fe^{2+} state due to the presence of multiple oxygen vacancies under SOFC operating conditions. Further removal of oxygen atom from this surface during H_2 oxidation process reduces the neighboring Fe atoms to an unstable Fe^{1+} state, making this process highly endergonic. The calculated Bader charges on the active oxygen and neighboring metal atoms on FeO_2- terminated surface before and after oxygen vacancy formation are provided in the top portion of the first two columns of Table 2.3 for comparison. When an oxygen atom on the surface is replaced by sulfur (Table 2.3, column 3), the neighboring Fe atoms are slightly reduced. Since sulfur has a lower electronegativity than oxygen it donates some of its charge to the neighboring Fe atoms, however oxygen tends to keep the extra charge. Thus sulfur forms strong covalent bonds with Fe whereas the Fe-O bonds are more ionic: the closer the Bader charge is to the formal oxidation state the more ionic is the bond. This is also the reason why the oxygen replacement reaction by sulfur on this surface is highly favorable (Table 2.1). When H_2 oxidation was considered on the $Fe-S-Fe$ site (Table 2.2, reaction (b)), the removal of S atom requires breaking two Fe-S covalent bonds and thus becomes highly

unfavorable. In Table 2.2, we have also shown that the presence of S on the surface further affects the oxygen vacancy formation energy at a neighboring site. The charges given in the last column of Table 2.3 (top) suggests that only part of the charge left on the surface upon removal of oxygen atom is transferred to the neighboring Fe atoms. Further analysis revealed that the remaining charge is transferred to the Fe/Mo and oxygen atoms in the second layer making those bonds more ionic and the vacancy structure less stable.

The electronic effect of Ni on the oxygen vacancy formation in the presence and absence of adsorbed sulfur can be analyzed from the calculated Bader charges provided in the bottom portion of Table 2.3. When Ni_3 cluster is adsorbed on the surface ($Sr_{16}Fe_{12}Mo_4O_{43}$), a small amount of charge (0.54 e^-) is transferred from Ni to the surface Fe atoms as we have shown in our earlier work for Ni_2 adsorption.[24] The average charge on the Ni atom (q_{Ni}^{ave}) is only +0.18, suggesting that the Ni atoms are mostly in metallic state. When the oxygen atom is removed from the surface, most of the extra charge (~0.60 e^-) left by oxygen is transferred back to the Ni cluster and the Fe atoms are not significantly further reduced. Thus Ni facilitates the rate controlling vacancy formation process by accepting the extra electrons left by oxygen. When S is adsorbed on the Ni cluster, the Ni atoms are more positively charged ($q_{Ni}^{ave} = +0.44$) due to the presence of negatively charged sulfur atom. However, we observed a similar amount of charge transfer from Ni to the surface (0.53 e^-) and a slightly smaller back transfer of charge from the surface to Ni (0.54 e^-) before and after oxygen vacancy formation, respectively. Although the amount of charge transfer from the surface to Ni upon oxygen vacancy formation is quite similar in the presence and absence of sulfur, there seems to

be a repulsive interaction between negatively charged Ni and S atoms which destabilizes the oxygen vacancy structure. Hence the promotional effect Ni could be suppressed by the presence of strongly adsorbed S atoms.

2.5 CONCLUSIONS

Constrained *ab initio* thermodynamic simulations have been performed to investigate the sulfur poisoning mechanism of different terminations of SFMO (001) surfaces under SOFC operating conditions. Three surface models, namely plane-Mo, diagonal-Mo, and FeO_2- terminated surfaces with varying Mo and oxygen vacancy concentration on the gas exposed layer were considered for this study. The interaction of sulfur on these surfaces has been examined by considering two types of reactions: dissociative adsorption of H_2S and replacement of a surface oxygen by sulfur. Calculated Gibbs free energies suggested that the oxygen replacement reaction by sulfur is favored over dissociative adsorption of H_2S on all the three surfaces. The phase diagrams further revealed that the dissociative adsorption of H_2S on these surfaces is favorable only when the H_2S concentration in the fuel stream exceeds 10^4 ppm at SOFC operating temperatures. While replacing $Mo - O - Fe$ type oxygen by sulfur on the plane-Mo surface (with higher Mo content on the surface layer) is also favorable only at high concentration of H_2S (>10^3 ppm), the replacement of $Fe - O - Fe$ type oxygen on the diagonal-Mo and FeO_2- terminated surfaces becomes feasible when H_2S concentration is <100 ppm. Nevertheless, the H_2S concentration required for a favorable oxygen replacement reaction is still higher than the amount required for poisoning the conventional Ni anodes. Thus, the SFMO anodes are in general less susceptible to sulfur

poisoning than the Ni anodes and the SFMO surface with higher Mo content on the exposed layer exhibits even better sulfur tolerance.

Furthermore, for the most stable and least active FeO_2- terminated surface we also examined the effect of sulfur on the surface oxygen vacancy formation process which was identified in our earlier work as rate controlling process for H_2 electro-oxidation. When S is present on the surface, the free energy of vacancy formation becomes more endergonic while considering H_2 oxidation at $Fe - S - Fe$ site as well as at a neighboring oxygen site. Although, adding small Ni_3 cluster on the surface promotes surface oxygen vacancy formation process, the presence of strongly adsorbed S atom on the Ni_3 cluster destabilizes the oxygen vacancy structure and thus will decrease the activity of the anode with time. Overall, increasing the Mo content on the gas exposed layer of SFMO anode not only improves its catalytic activity but also maintains excellent sulfur tolerance.

2.6 ACKNOWLEDGEMENTS

This work was supported by the Heterogeneous Functional Materials Center (HeteroFoaM), an Energy Frontier Research Center (EFRC) funded by the US Department of Energy, Office of Basic Energy Science under Award No. DE-SC0001061. Computations were carried out at the US Department of Energy facilities located at the National Energy Research Scientific Computing Center (NERSC) and at EMSL, located at Pacific Northwest National Laboratory (Grant Proposal 47447). Furthermore, a portion of this research was performed with XSEDE resources provided

by the National Institute for Computational Sciences (NICS) and Texas advanced Computing Center (TACC) under grant number TG-CTS090100. Finally, computing resources from USC's High Performance Computing Group are gratefully acknowledged.

2.7 REFERENCES

(1) EG&G Technical Services for NETL of U.S. Department of Energy, *Fuel Cell Handbook*, 2004.
(2) Atkinson, A.; Barnett, S.; Gorte, R. J.; Irvine, J. T. S.; McEvoy, A. J.; Mogensen, M.; Singhal, S. C.; Vohs, J. *Nat Mater* **2004**, *3*, 17-27.
(3) Minh, N. Q. *J. Am. Ceram. Soc.* **1993**, *76*, 563-588.
(4) Minh, N. Q. *Solid State Ionics* **2004**, *174*, 271-277.
(5) Singh, P.; Minh, N. Q. *International Journal of Applied Ceramic Technology* **2004**, *1*, 5-15.
(6) Sasaki, K.; Susuki, K.; Iyoshi, A.; Uchimura, M.; Imamura, N.; Kusaba, H.; Teraoka, Y.; Fuchino, H.; Tsujimoto, K.; Uchida, Y.; Jingo, N. *J. Electrochem. Soc.* **2006**, *153*, A2023-A2029.
(7) Matsuzaki, Y.; Yasuda, I. *Solid State Ionics* **2000**, *132*, 261-269.
(8) Abild-Pedersen, F.; Lytken, O.; Engbaek, J.; Nielsen, G.; Chorkendorff, I.; Norskov, J. K. *Surf. Sci.* **2005**, *590*, 127-137.
(9) Singhal, S. C.; Ruka, R. J.; Bauerle, J. E.; Spengler, C. J. *Anode Development for Solid Oxide Fuel Cells, Final Technical Report, Doe/Mc/22046-2371*, 1986.
(10) Stolten, D.; Spah, R.; Schamm, R.; Stimming, U., Singhal, S. C., Tagawa, H., Lennert, W., Eds.; The Electrochemical Society Proceeding Series: Pennington, NJ, 1997; Vol. PV 97-40, p 88.
(11) Gong, M. Y.; Liu, X. B.; Trembly, J.; Johnson, C. *J. Power Sources* **2007**, *168*, 289-298.
(12) Yang, L.; Cheng, Z.; Liu, M. L.; Wilson, L. *Energ Environ Sci* **2010**, *3*, 1804-1809.
(13) Cheng, Z.; Zha, S. W.; Liu, M. L. *J. Power Sources* **2007**, *172*, 688-693.
(14) Zha, S. W.; Cheng, Z.; Liu, M. L. *J. Electrochem. Soc.* **2007**, *154*, B201-B206.
(15) Prasad, B. V. R. S. N.; Janardhanan, V. M. *J. Electrochem. Soc.* **2014**, *161*, F208-F213.
(16) Weber, A.; Dierickx, S.; Kromp, A.; Ivers-Tiffee, E. *Fuel Cells* **2013**, *13*, 487-493.
(17) Marina, O. A.; Coyle, C. A.; Engelhard, M. H.; Pederson, L. R. *J. Electrochem. Soc.* **2011**, *158*, B424-B429.
(18) Liu, Q.; Dong, X.; Xiao, G.; Zhao, F.; Chen, F. *Adv. Mater.* **2010**, *22*, 5478-5482.
(19) Xiao, G.; Chen, F. *Electrochem. Commun.* **2011**, *13*, 57-59.
(20) Munoz-Garcia, A. B.; Bugaris, D. E.; Pavone, M.; Hodges, J. P.; Huq, A.; Chen, F.; zur Loye, H.-C.; Carter, E. A. *J. Am. Chem. Soc.* **2012**, *134*, 6826-6833.

(21) Munoz-Garcia, A. B.; Pavone, M.; Ritzmann, A. M.; Carter, E. A. *PCCP* **2013**, *15*, 6250-6259.
(22) Xiao, G.; Liu, Q.; Nuansaeng, S.; Chen, F. *ECS Transactions* **2012**, *45*, 355-362.
(23) Xiao, G. L.; Jin, C.; Liu, Q.; Heyden, A.; Chen, F. L. *J. Power Sources* **2012**, *201*, 43-48.
(24) Suthirakun, S.; Ammal, S. C.; Muñoz-García, A. B.; Xiao, G.; Chen, F.; Loye, H.-C. z.; Carter, E. A.; Heyden, A. *J. Am. Chem. Soc.* **2014**, (accepted for publication).
(25) Kresse, G.; Furthmuller, J. *Phys Rev B* **1996**, *54*, 11169-11186.
(26) Kresse, G.; Joubert, D. *Phys Rev B* **1999**, *59*, 1758-1775.
(27) Perdew, J. P.; Burke, K.; Ernzerhof, M. *Phys. Rev. Lett.* **1996**, *77*, 3865-3868.
(28) Blochl, P. E. *Phys Rev B* **1994**, *50*, 17953-17979.
(29) Monkhorst, H. J.; Pack, J. D. *Phys Rev B* **1976**, *13*, 5188-5192.
(30) Munoz-Garcia, A. B.; Pavone, M.; Carter, E. A. *Chem. Mater.* **2011**, *23*, 4525-4536.
(31) Makov, G.; Payne, M. C. *Phys Rev B* **1995**, *51*, 4014-4022.
(32) Kroger, F. A.; Vink, H. J. *Solid State Phys* **1956**, *3*, 307-435.
(33) Wang, J. H.; Liu, M. L. *Electrochem. Commun.* **2007**, *9*, 2212-2217.
(34) Hansen, K. V.; Norrman, K.; Mogensen, M. *J. Electrochem. Soc.* **2004**, *151*, A1436-A1444.
(35) Lohsoontorn, P.; Brett, D. J. L.; Brandon, N. P. *J. Power Sources* **2008**, *175*, 60-67.
(36) Monder, D. S.; Karan, K. *J Phys Chem C* **2010**, *114*, 22597-22602.
(37) Bader, R. F. W. *Atoms in Molecules - a Quantum Theory*; Oxford University Press: New York, 1990.
(38) Tang, W.; Sanville, E.; Henkelman, G. *J Phys-Condens Mat* **2009**, *21*, 084204.

2.8 TABLES AND FIGURES

Table 2.1 Gibbs free energies for the dissociative adsorption of H_2S (ΔG^{ads}, eqn. 9) and oxygen replacement by H_2S (ΔG^{repl}, eqn. 10) on the SFMO (001) surface calculated at T = 1100 K and P_{gas} = 1 atm.

Surface Model	**Adsorption site**	ΔG^{ads} **(eV)**	**Active site**	ΔG^{repl} **(eV)**
Plane-Mo	$Mo - V_O^{\bullet\bullet} - Fe$	0.30	$Mo - O - Fe$	-0.17
Diagonal-Mo	$Mo - V_O^{\bullet\bullet} - Fe$	0.72	$Mo - O - Fe$	-0.17
	$Fe - V_O^{\bullet\bullet} - Fe$	-0.33	$Fe - O - Fe$	-0.47
FeO_2-terminated	$Fe - V_O^{\bullet\bullet} - Fe$	-0.01	$Fe - O - Fe$	-0.55

Table 2.2 Gibbs free energies (ΔG) for the formation of an oxygen vacancy on the FeO_2-terminated SFMO surface in the presence and absence of sulfur and nickel under reducing conditions (T = 1100 K, P_{gas} = 1 atm). $Fe-S-Fe$ represents the active site on the FeO_2- terminated surface after an oxygen atom of $Fe-O-Fe$ active site is replaced by a sulfur atom and $V_O^{\bullet\bullet}$ is the oxygen vacancy.

Reaction	**ΔG (eV)**
$(a)\ Fe-O-Fe\ + H_{2(g)} \leftrightarrow\ Fe-V_O^{\bullet\bullet}-Fe + H_2O_{(g)}$	1.07
$(b)\ Fe-S-Fe\ + H_{2(g)} \leftrightarrow\ Fe-V_O^{\bullet\bullet}-Fe + H_2S_{(g)}$	1.68
$(c)\ Fe-S-Fe-O-Fe\ + H_{2(g)} \leftrightarrow\ Fe-S-Fe-V_O^{\bullet\bullet}-Fe + H_2O_{(g)}$	1.16
$(d)\ Ni_3/Fe-O-Fe\ + H_{2(g)} \leftrightarrow\ Ni_3/Fe-V_O^{\bullet\bullet}-Fe + H_2O_{(g)}$	0.14
$(e)\ S-Ni_3/Fe-O-Fe\ + H_{2(g)} \leftrightarrow\ S-Ni_3/Fe-V_O^{\bullet\bullet}-Fe + H_2O_{(g)}$	0.74

Table 2.3 Calculated Bader charges (in *e*) on the neighboring metals and active oxygen/sulfur atom on the FeO_2- terminated surface in the presence and absence of sulfur and nickel cluster.

	SFMO			
	$Sr_{16}Fe_{12}Mo_4O_{43}$ (Fe_1-O_1-Fe_2-O_2-Fe_3)	$Sr_{16}Fe_{12}Mo_4O_{42}$ (Fe_1-$V_O^{\bullet\bullet}$-Fe_2-O_2-Fe_3)	$Sr_{16}Fe_{12}Mo_4O_{42}$ S (Fe_1-S_1-Fe_2-O_2-Fe_3)	$Sr_{16}Fe_{12}Mo_4O_{41}$ S (Fe_1-S_1-Fe_2-$V_O^{\bullet\bullet}$-Fe_3)
Fe_1	+1.21	+0.64	+1.11	+1.10
Fe_2	+1.22	+0.68	+1.12	+0.71
Fe_3	+1.22	+1.21	+1.23	+0.87
O_1/S_1	-1.28	--	-1.10	-1.07
O_2	-1.30	-1.30	-1.30	--
Ni:SFMO				
	Ni_3/$Sr_{16}Fe_{12}Mo_4O_{43}$ (Fe_1-O-Fe_2)	Ni_3/$Sr_{16}Fe_{12}Mo_4O_{42}$ (Fe_1-$V_O^{\bullet\bullet}$-Fe_2)	S-Ni_3/$Sr_{16}Fe_{12}Mo_4O_{43}$ (Fe_1-O-Fe_2)	S-Ni_3/$Sr_{16}Fe_{12}Mo_4O_{42}$ (Fe_1-$V_O^{\bullet\bullet}$-Fe_2)
Fe_1	+1.13	+0.85	+1.12	+0.84
Fe_2	+1.17	+0.89	+1.18	+0.86
3×Ni	+0.54	-0.06	+1.32	+0.76
S	--	--	-0.79	-0.77

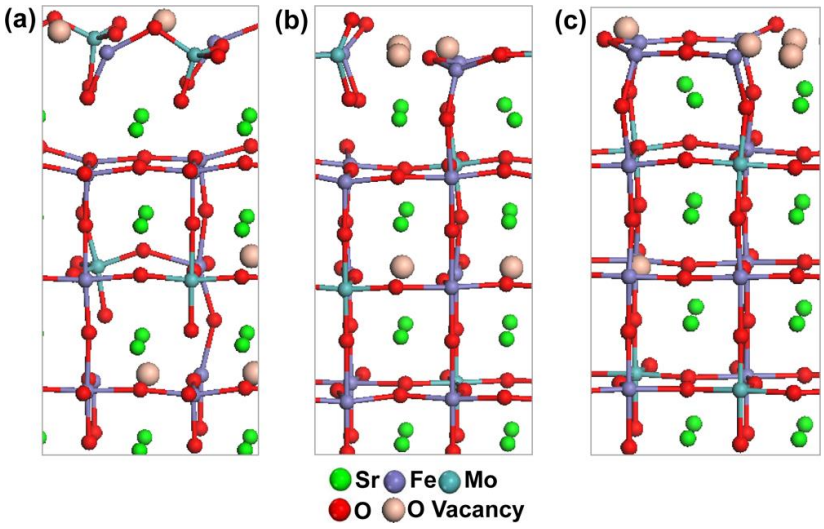

Figure 2.1 $Sr_2Fe_{1.5}Mo_{0.5}O_{6-\delta}$ ($\delta = 0.625$) (001) surface models used to study the sulfur poisoning mechanism: (a) plane-Mo surface (Mo:Fe = 1) (b) diagonal-Mo surface (Mo:Fe = 0.33), and (c) FeO_2- terminated surface (Mo:Fe = 0).

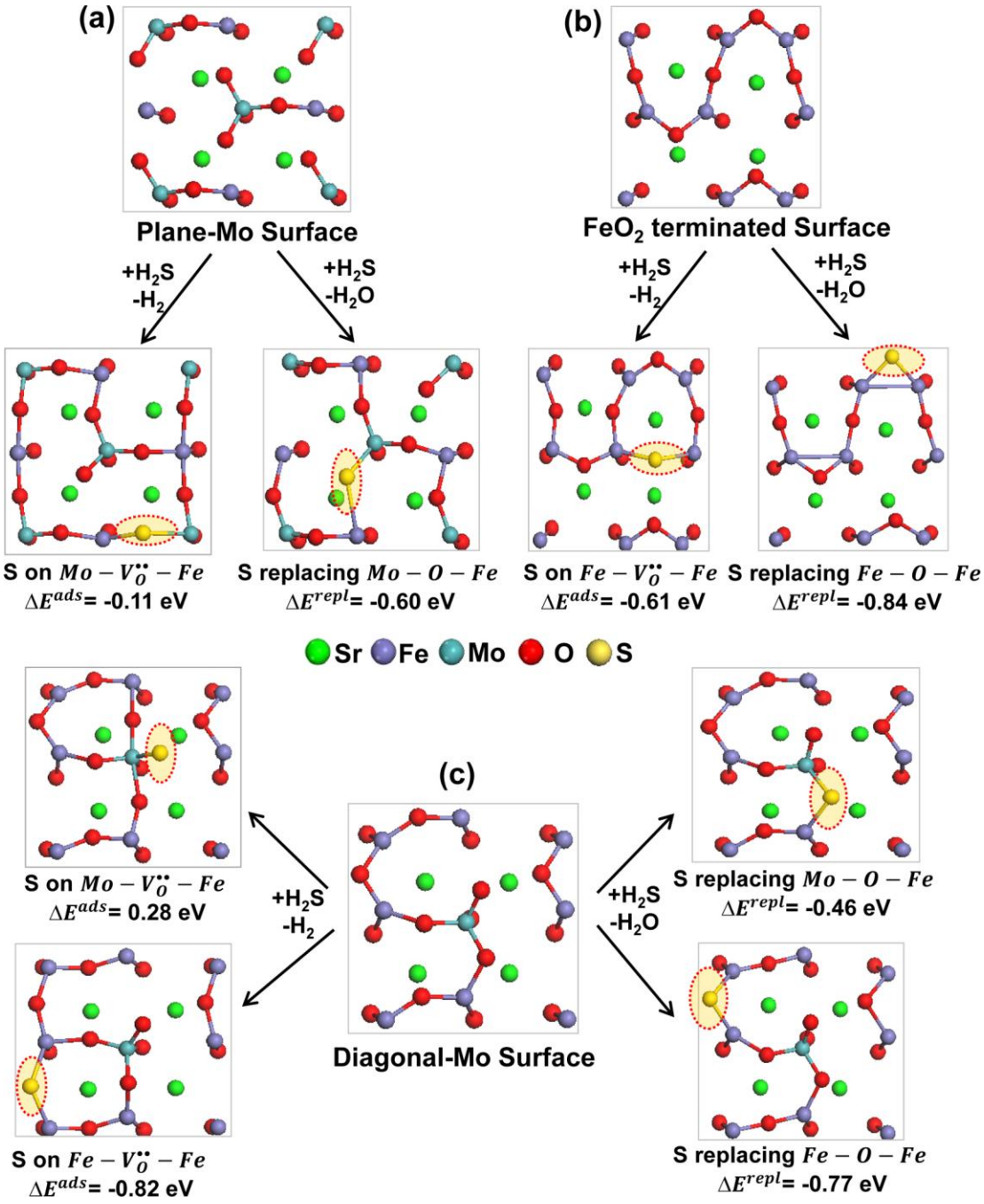

Figure 2.2 Top view of the optimized structures of S adsorbed on an oxygen vacancy ($M - V_O^{\bullet\bullet} - Fe, M = Mo\ or\ Fe$) and S replacing an oxygen atom ($M - O - Fe, M = Mo\ or\ Fe$) on the reduced SFMO (001) surface models (a) plane-Mo surface (b) FeO_2-terminated surface, and (c) diagonal-Mo surface. ΔE^{ads} and ΔE^{repl} provided under each structure correspond to the reaction energy of dissociative adsorption of H_2S ($H_2S + M - V_O^{\bullet\bullet} - Fe \leftrightarrow H_2 + M - S - Fe$) and oxygen replacement by S ($H_2S + M - O - Fe \leftrightarrow H_2O + M - S - Fe$), respectively.

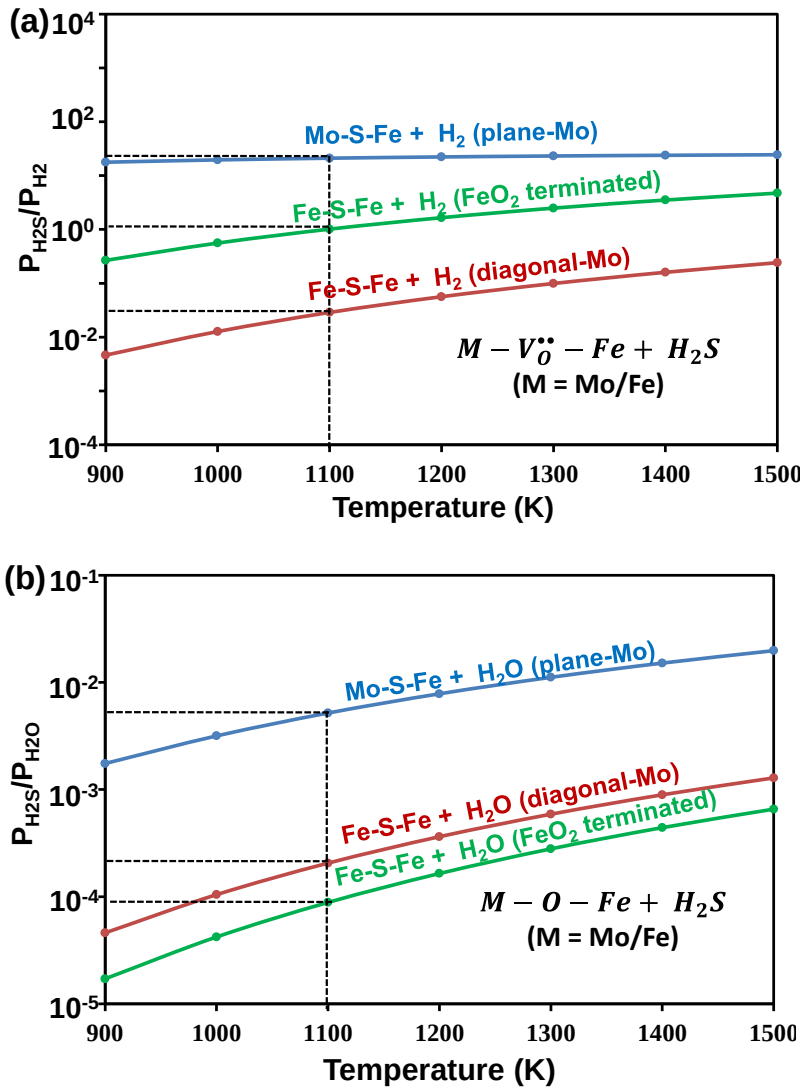

Figure 2.3 Calculated phase diagrams for the interaction of S on SFMO (001) surfaces (a) dissociative adsorption of H_2S on an oxygen vacancy ($H_2S + M - V_O^{\bullet\bullet} - Fe \leftrightarrow H_2 + M - S - Fe, M = Mo\ or\ Fe$) (b) oxygen replacement reaction by S ($H_2S + M - O - Fe \leftrightarrow H_2O + M - S - Fe, M = Mo\ or\ Fe$).

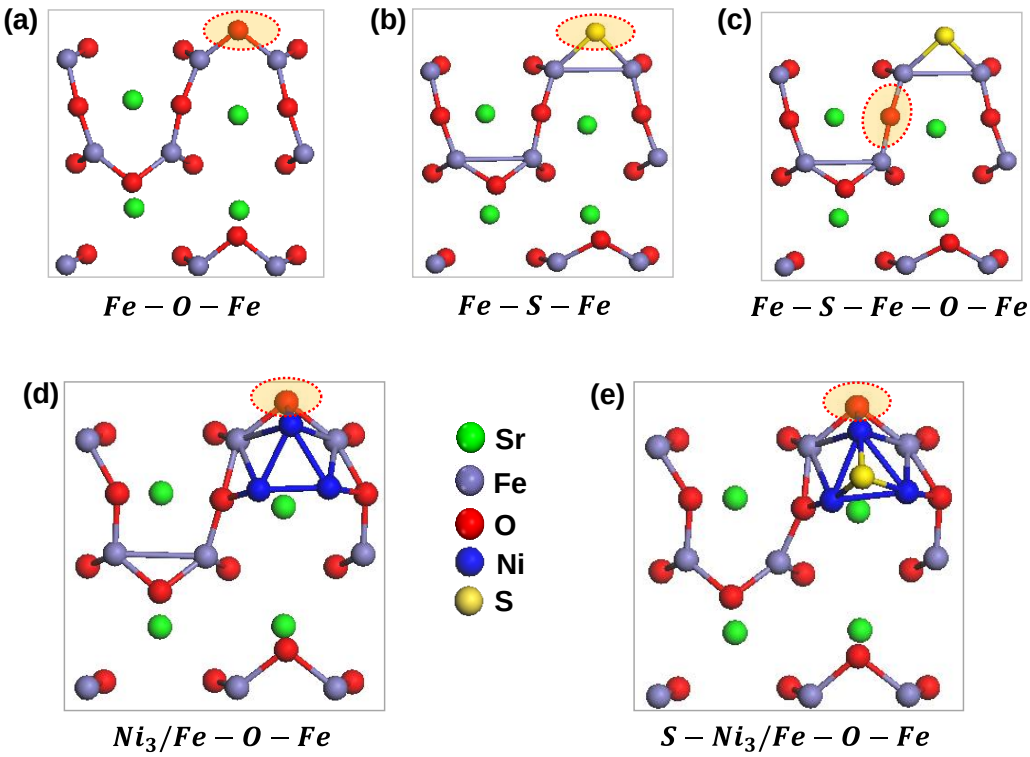

Figure 2.4 Top view of reactant structures corresponding to the reactions provided in Table 2.2. Highlighted atom represents the atom removed during surface vacancy formation.

CHAPTER 3

UNCERTAINTY QUANTIFICATION FRAMEWORK APPLIED TO THE WATER-GAS SHIFT REACTION OVER PT-BASED CATALYSTS[1]

[1]Walker, E.; Ammal, S. C.; Terejanu, G. A.; Heyden, A. *J. Phys. Chem. C*, **2016**, 120, 10328–10339.

Reprinted here with permission of publisher.

3.1 ABSTRACT

This paper presents a systematic approach to quantify uncertainties of various quantities of interest (QoIs) in catalysis determined by microkinetic models developed from first principles. One of the main sources of uncertainty in any microkinetic simulation is attributed to the exchange-correlation approximations in density functional theory (DFT) used to calculate the rate constants for all elementary reaction steps within transition state theory. These DFT approximations are at the core of significant discrepancies between computational simulations and experimental measurements. Therefore, any model calculation should be accompanied by a measure of uncertainty. This work uses probability to represent uncertainties and latent variable models to develop probabilistic models that account for errors and correlations in DFT energies. These probabilistic models are further constrained to known reaction thermodynamics, and then propagated to QoIs such as turnover frequency (TOF), apparent activation barrier, and reaction orders. The proposed uncertainty quantification (UQ) framework is applied on the water−gas shift reaction (WGS: $CO + H_2O \rightleftharpoons CO_2 + H_2$). Specifically, this WGS study models a Pt/TiO_2 catalyst as a Pt_8 cluster supported on a rutile TiO_2 (110) surface, where DFT energies are obtained using four separate functionals PBE, RPBE, HSE, and M06L that each have their own justification for being appropriate for this study. In this way, information from three different classes of functionals, GGA (generalized-gradient approximation), meta-GGA, and hybrid functionals, are used to generate a free energy probabilistic model. Although the uncertainty in model results spans orders of magnitude, a new approach is introduced to identify the dominant catalytic cycle under uncertainty. Overall, we find that our model captures various

experimental kinetic data; however, the probability densities for TOF, apparent activation barrier, and reaction orders are relatively wide due to different flavors of DFT predicting a wide variation of transition state and oxygen vacancy formation energies. Nevertheless, we can conclude with high certainty that a CO-promoted redox cycle is the dominant mechanism over the temperature range 473−600 K and that formate and carboxyl pathways are not playing any role for the investigated active site model.

3.2 INTRODUCTION

Microkinetic models play an important role in understanding reaction kinetics and production rates on macroscopic scales. The insight provided by microkinetic model simulations can be used to speed up the rational design of novel catalytic materials.[1−3] Density functional theory (DFT) provides a good starting point to estimate (together with harmonic transition state theory) the values of rate constants for each elementary step in the microkinetic model. However, DFT calculations have inadequacies due to exchange-correlation approximations, which induce significant errors in the prediction of macroscopic quantities of interest (QoI) such as turnover frequency (TOF), apparent activation barrier, and reaction orders. For example, a variation of only 0.2 eV in a DFT predicted activation barrier leads to an uncertainty of 2 orders of magnitude in an elementary reaction rate constant in a catalytic cycle at 500 K, which again can lead to significant uncertainty in microkinetic modeling results. Therefore, new computational tools are required to quantify uncertainties in DFT calculations, propagate them to QoIs, and guide the process of drawing conclusions under uncertainty. We note that we limit ourselves in the following to uncertainties in the DFT functional and neglect any

uncertainties related to estimating entropies and using harmonic transition state theory. In fact, we assume that these uncertainties are small relative to the uncertainties in DFT energies such that they can approximately be mapped into the uncertainties of the DFT energies (an approximation that might not be valid for some surface states). We note that considering these uncertainties does not constitute any additional complication and our proposed framework can in principle be extended to include these uncertainties. Also, we are not concerned with inadequacies of our active site model structure and number of elementary reaction steps but aim at predicting the QoIs for a given active site model and reaction mechanism.

Previously, a number of research groups such as Mortensen et al.,[4] Cramer,[5] and Hanke[6] have investigated the errors in DFT energies of functionals commonly used in heterogeneous catalysis. Also, Vlachos and co-workers[7,8] have proposed corrections for energies of formation and binding energies obtained by DFT calculations to explain differences in DFT energies and experimental observations. Errors in DFT energies have often been assumed to behave systematically; e.g., a constant correction term was assigned to any species containing an OCO backbone.[9] This systematic error was determined by comparing DFT energies of gas molecules to National Institute of Standards and Technology (NIST) data.[10] While such a systematic approach is appealing, there is little scientific justification regarding why errors in DFT energies can be divided into atom groups that are transferable to systems containing transition metal surfaces. Recently, Petzold et al.[11] have proposed the use of databases of electronic density functionals fit by Bayes formula. This research led to the Bayesian error estimation−van der Waals (BEEF-vdW) functional,[4,12−14] a seminal work in quantifying uncertainties in

DFT energies. BEEF-vdW is based on using empirical data of microscopic properties such as binding energies to infer errors and correlations in DFT energies due to the exchange-correlation functional approximation. Medford et al.[12] recently found by studying the ammonia synthesis reaction that these correlations in energies play an important role in reducing the uncertainty in QoIs such as TOFs. One way to obtain correlations is to use the ensemble or a subset of the ensemble of functionals from BEEF-vdW.[4,12−14] However, these correlations are based strictly only on generalized-gradient approximation (GGA) functionals, and GGAs can face issues when electrons become localized such as in oxide systems.[15,16] For example, in the system of consideration, oxygen vacancies are formed on a TiO_2 surface, and a strategy based exclusively on GGA functionals for estimating errors and their correlation risks underestimating the inherent uncertainties since all GGA functionals will overdelocalize electrons which leads to lower vacancy formation energies.

In this work, we propose to describe the uncertainty in DFT energies by explicitly accounting for information provided by various classes of functionals such as GGA, meta-GGA, as well as hybrid functionals. Specifically, we only choose DFT functionals (PBE,[17] RPBE,[18,19] HSE,[20] and M06L[21]) that have some justification to be used in a DFT study of the active site model structure and that are all known to have different limitations relevant for the reaction mechanism. Next, DFT energies calculated with these functionals are used in a factor analysis[22] to develop a probabilistic latent variable model that accounts for errors and correlations in DFT energies. This probabilistic model is further extended to ensure that samples of DFT energies are constrained to known reaction thermodynamics. This is accomplished by designing a separate probabilistic

model for energy correction of gas molecules based on the Dirichlet distribution.[23] The uncertainty captured by this composite probabilistic model for DFT energies is propagated through the microkinetic model to QoIs using Monte Carlo simulations. Specifically, the composite probabilistic model is used to generate correlated and thermodynamically constrained DFT energy samples, which are then used to calculate rate constants in the microkinetic model. Finally, the uncertainty in the QoIs such as TOF, reaction orders, and apparent activation energy is captured by samples corresponding to the QoI predictive distribution. As the model calculations are no longer deterministic but rather probabilistic, new tools are required to draw conclusions under uncertainty. This work introduces the information theoretic quantity, Kullback− Leibler divergence, to determine the dominant pathway by finding the smallest divergence between the probability density function (PDF) of the overall TOF and the PDF of individual pathway TOF.

To summarize, uncertainty quantification (UQ) is the process of assessing and representing uncertainties in model simulations such that their impacts on the QoIs can be determined. This paper presents a systematic approach to quantify uncertainties in QoIs calculated using microkinetic models. The proposed UQ framework for computational catalysis consists of three distinct processes: (1) quantifying uncertainties in DFT energies, (2) propagating uncertainties to QoIs, and (3) drawing conclusions using uncertain QoIs. To showcase the proposed UQ framework, we apply it to our recent water−gas shift reaction model (WGS: $CO + H_2O \rightleftharpoons CO_2 + H_2$) over Pt/TiO_2 catalysts.[24]

The WGS is an essential step in industrial chemical processes utilizing hydrogen.[24–33] Besides producing hydrogen, the WGS consumes carbon monoxide (CO) which is beneficial because CO is a poison for noble metal catalysts and catalysts used in fuel cell applications.[26,32,33] With these important applications comes a desire to understand the WGS over relevant catalyst systems. The case study in this work builds upon a theoretical investigation[24] of the WGS over an active site at a three-phase boundary (TPB) of a metal nanoparticle, a reducible metal oxide support, and a gas phase. It has been hypothesized that TPB sites are the origin of unique activity and selectivity of various reducible oxide supported metal cluster catalysts. For example, gold (Au) catalysts on reducible oxide supports possess a unique activity attributed to TPB sites.[34–36] The specific catalyst of this case study is platinum supported by titanium oxide (Pt/TiO_2).[37–39] Pt/TiO_2 reports more activity than systems of Pt on other mixed oxides[34] and has been investigated for low and medium temperature WGS reactions.[40–47] A current question of high interest is if individual metal atoms or metal clusters/nanoparticles supported on reducible oxide supports are the active site for catalysis.[48–50] DFT calculations and microkinetic modeling can be used to shed more light on the activity of various active site models and has been used here for a Pt_8/TiO_2 (110) catalyst model characteristic of a metal cluster on rutile TiO_2. At the same time, describing the electronic structure of reaction intermediates and transition states at the interface of a Pt cluster and a TiO_2 support during the WGS is quite challenging with DFT considering that regions of the active site model are clearly metallic while the oxide support is a semiconductor. Considering furthermore that the oxygen vacancy formation energy of TiO2 is significantly underpredicted by GGA-DFT,[51] there is increased

uncertainty in our previous computational predictions that have been based on GGA-DFT,[24,52] making this catalytic system an ideal test case for our novel UQ approach.

3.3 UNCERTAINTY QUANTIFICATION

This section introduces the proposed UQ framework for a general system where N functionals have been used to obtain energies for intermediate and transition states. In this work, N = 4. This data set is used to generate a probabilistic latent variable model to capture both the variation of DFT energies for individual states and the correlation between energies at various states. This probabilistic model is further constrained to known reaction thermodynamics, and then it is propagated to QoIs such as turnover frequency (TOF), apparent activation barrier, and reaction orders. Finally, an information theoretic approach is introduced to determine the dominant catalytic cycle under uncertainty.

3.3.1 DFT Latent Variable Model

In this work the probabilistic latent variable model used to summarize the uncertainty in DFT calculations is developed using factor analysis. Factor analysis expresses observed variables (functional results) as a linear combination of a small number of factors.[22] This allows the model to represent the uncertainty in the functionals as a multivariate Gaussian with a restricted number of free parameters and still capture the dominant correlations in the data set. Using fewer factors than functionals is possible because the functionals are correlated.[4,9] An exchange-correlation functional in DFT

tends to overestimate one intermediate state energy if it overestimates a similar intermediate energy. Positive correlation signifies corrections moving together, and negative correlation corresponds to corrections occurring opposite to each other.

Factor analysis models the observable in the following manner.

$$\boldsymbol{y} = \boldsymbol{W}\boldsymbol{z} + \boldsymbol{\mu} + \boldsymbol{e} \tag{1}$$

Here, the vector $\boldsymbol{y}$ denotes the observed DFT Gibbs' free energies for all intermediate and transition states relative to a clean catalyst with reactant molecules in the gas phase, $\boldsymbol{z}$ is a vector of independent factors/latent variables that are normally distributed, $N(0,1)$, the matrix $\boldsymbol{W}$ contains the factor loadings that capture the correlations between observables, and $\boldsymbol{e}$ is a zero-mean Gaussian distributed noise with a diagonal covariance matrix $\boldsymbol{\Psi}$ that contains *specific variances*.[22]

The parameters, $\boldsymbol{W}, \boldsymbol{\mu}$, and $\boldsymbol{\Psi}$ are determined using maximum likelihood[22] via Expectation Maximization, i.e., $\boldsymbol{\mu}$ becomes a vector of the average of the DFT predicted Gibbs' free energies.[53] Given the set of N DFT calculations, $\boldsymbol{Y} = \{\boldsymbol{y_1}, \ldots, \boldsymbol{y_N}\}$, the corresponding log-likelihood function, $\ln \boldsymbol{p}$, to be maximized is given by,

$$\ln \boldsymbol{p}(\boldsymbol{Y}|\, \boldsymbol{W}, \boldsymbol{\mu}, \boldsymbol{\Psi}) = \sum_{\boldsymbol{i=1}}^{\boldsymbol{N}} \ln \boldsymbol{p}(\boldsymbol{y_i}|\, \boldsymbol{W}, \boldsymbol{\mu}, \boldsymbol{\Psi}) \tag{2}$$

The number of optimal factors is determined using cross-validation. After parameter learning, the marginal distribution for the observable $\boldsymbol{y}$ is given by a Gaussian

distribution with mean $\boldsymbol{\mu}$ and covariance matrix given by $\boldsymbol{\Sigma} = \boldsymbol{W}\boldsymbol{W}^T + \boldsymbol{\Psi}$. With this method the correlation structure is from N functional results rather than setting a correlation structure by choosing a chemical similarity measure among states and transition states. This latent variable model is used to draw samples of energies corresponding to intermediate and transition states. However, these energy samples may not match the reaction thermodynamics.

3.3.2. Thermodynamics correction

The factor analysis described above has been conducted on the free energies of surface intermediate and transition states. After the factor analysis is completed, a separate probabilistic model is proposed to correct the free energies of the gas molecules such that they match the overall reaction thermodynamics (Gibbs' free energy of reaction). Given M gas molecules with $\{\zeta_1, \zeta_2, \ldots \zeta_M\}$ corrections, then the following constraint is imposed on the gas molecule corrections.

$$\sum_{i=1}^{M} \zeta_i = \delta \tag{3}$$

Note that δ is constant (the average error of our DFT functionals in predicting the Gibbs' free energy of reaction). The individual corrections may be bounded due to the uncertainty associated with the magnitude of the correction. Namely, each correction has its own associated uncertainty.

$$\underline{\zeta_i} \leq \zeta_i \leq \overline{\zeta_i} \tag{4}$$

A modified uniform Dirichlet distribution (Diun) is used in this work[23] to guarantee that the sample corrections sum up to the right-hand side of equation (3) and that individual corrections are within the set bounds. We start with a set of M random variables $\{\zeta_i^*\}$ with joint distribution defined by Diun.[23] Here, the Diun samples obey the following relation.

$$\sum_{i=1}^{M} \zeta_i^* = 1 \tag{5}$$

To generate the samples for gas molecule corrections using Diun samples, first we have to define a transformation that will preserve the sum of corrections to be equal with the overall thermodynamics. The proposed relationship between Diun random variables and the gas molecule free energy correction is given by the following linear transformation.

$$\zeta_i = a + (b - a)\, \zeta_i^* \tag{6}$$

Here, $a = \min\left(\left\{\underline{\zeta_i}\right\}_{i=1..M}\right)$ and $b = \delta - a(M-1)$. Note, that the individual upper bounds $\overline{\zeta_i}$ should be smaller than b. This transformation only ensures that the gas molecule corrections sum up to the right-hand side of equation (3), i.e., that the overall Gibbs' free energy of reaction agrees exactly with NIST data. However, the sampling algorithm needs to take into account that the correction samples generated using this transformation might be larger than the imposed upper bound. As a result, all sample values higher than the upper bound are rejected and sampling is continued until the

desired number of feasible samples is obtained. Gas molecule energy corrections affect all state and transition state energies that contain gas molecules. Given a DFT energy sample $\boldsymbol{y}$ from the latent variable model previously introduced, a set of corrections $\{\zeta_i\}$ is drawn such that the corrected energy sample $\boldsymbol{y}_{\boldsymbol{corrected}}$ matches the overall thermodynamics.

3.3.3. Propagation of uncertainty to quantities of interest

Consider the turnover frequency (TOF) given by a mapping involving a microkinetic simulation that depends on the corrected DFT energies:

$$TOF = f(\boldsymbol{y}_{\boldsymbol{corrected}}) \tag{7}$$

The following relation gives the probability distribution of TOF induced by the DFT errors and magnitudes of gas molecule corrections.

$$p(TOF) = \int p(TOF|\,\boldsymbol{y}_{\boldsymbol{corrected}})p(\boldsymbol{y}_{\boldsymbol{corrected}})d\boldsymbol{y}_{\boldsymbol{corrected}} \tag{8}$$

Here, a Monte Carlo simulation is proposed to obtain samples from the probability distribution of TOF. A TOF sample is generated as follows. First an energy sample is generated for every intermediate state and transition state according to the latent variable model. Second, a set of gas molecule corrections is generated using the modified Diun. The corrected energy sample is then used to calculate the rate constants and solve the

microkinetic model. The TOF result of the microkinetic model is stored and a new set of energies is selected and this process is repeated a significant number of times.

Similarly, one can quantify the uncertainty of other QoIs for comparison with experiments such as activation barrier (eV) and reaction orders. The apparent activation barrier is calculated as

$$E_{app} = k_B T^2 \left(\frac{dln(TOF)}{dT}\right)_{P,T} \tag{9}$$

where P is pressure, T is temperature and k_B is Boltzmann's constant. A range of temperature points and a linear fit are used to calculate $E_{app}\ (eV)$. Reaction orders, α_i for each species are calculated as

$$\alpha_i = \left(\frac{dln(TOF)}{dln(P_i)}\right)_{T,P_{j\neq i}} \tag{10}$$

where P_i (atm) represents the partial pressure of gas species, i.

3.3.4. Determining the dominant catalytic cycle

The microkinetic model generates a variety of results comparable with experiments. The overall TOF (s^{-1}) as well as individual catalytic cycle TOF's are solved for. Calculating individual catalytic cycle TOF uncertainties allows evaluating the dominant cycle in a reliable manner. The dominant catalytic cycle may be identified

using Kullback-Leibler (KL) divergence[54,55], which is used in information theory to measure the difference between two probability distributions. KL divergence is defined by

$$D_{KL}(P||Q) = \int_{\mathrm{x}} p(x) \ln\left(\frac{p(x)}{q(x)}\right) \tag{11}$$

where x is an uncertain variable. p and q are two probabilities for a given value of x. The KL divergence is taken for each catalytic cycle TOF q from the overall TOF p in the case study. A large KL divergence means PDF q is far from PDF p. The KL divergence is non-negative and it is zero when the two PDF's p and q are identical. A trapezoidal integration in MATLAB, *trapz*, is utilized to evaluate the integral in which the individual catalytic cycle TOF is q and the overall TOF is p. Specifically, a kernel density estimator, MATLAB's *ksdensity*, is used to obtain a set of probabilities and their corresponding TOF values for the trapezoidal integration. The dominant cycle is given by the catalytic cycle TOF that has the smallest KL divergence with respect to the overall TOF. Figure 3.1 illustrates the workflow of the general framework provided in this section.

3.4 WGS APPLICATION

Computational and model details of our case study model of the WGS over Pt_8/TiO_2 are available in Ammal et al.[24] DFT calculations used the PBE[17] functional to approximate exchange and correlation effects. For a factor analysis[22] three more functionals are used along with PBE to obtain the correlations for a covariance matrix. The additional functionals are the revised Perdew-Burke-Ernzerhof (RPBE)[18,19], Heyd-

Scuseria-Ernzerhof (HSE)[20], and M06L[21] which is a Minnesota functional. PBE uses a GGA which utilizes fundamental parameters apart from local spin density parameters to approximate the exchange-correlation energy in Kohn-Sham DFT and is considered a universally good functional.[56] RPBE belongs to the class of GGA functionals that has been optimized for chemisorption energetics on transition metal surfaces to overcome the observed limitation of PBE to often overestimate the adsorption energy of various small molecules.[18] Interestingly for this study, it has been proposed that PBE overestimates the binding of CO and H, while RPBE misrepresents the energy of species with OCO backbone.[9] All of these species are of significant importance for the WGS. Next, HSE is a computationally efficient hybrid exchange density functional based on the PBE0 (or sometimes called PBEh) functional that contains 25% exact exchange.[20,57] For non-metallic systems, transition state energies, and (of particular importance for this study) oxygen vacancy formation energies, it has been argued that the inclusion of exact exchange is important to describe the electronic structure correctly[16,58]. Finally, we also performed calculations with the M06L meta-GGA DFT functional that is computationally faster than hybrid exchange functionals (though significantly slower than pure GGA functionals) and that has been optimized to predict good energetics (including energy barriers and medium range dispersion interactions) for transition metal, inorganic and organometallic systems.

Climbing image nudge elastic band and dimer methods were used to obtain transition states[24,59-60] at the PBE level of theory as reported previously. For all other DFT functionals we only performed single point energy calculations on the PBE optimized geometries. A full optimization with each DFT functional would be preferred; however,

the computational expense would be significantly larger (particularly for the HSE and M06L calculations) such that we refrained from using such an approach here. Transition state theory within the harmonic approximation and for adsorption processes collision theory were used to calculate reaction rate constants. For the vibrational partition function and zero-point energy (ZPE) correction we used the numbers from the PBE functional where we shifted all vibrational frequencies smaller than 100 cm^{-1} to 100 cm^{-1} to avoid having large entropy contributions from very small frequencies. The vibrational frequencies are computed by numerical differentiation. A 0.01 Å displacement was used for all vibrational frequency calculations. There are four catalytic cycles considered in this case study. The first catalytic cycle is the classical redox catalytic cycle.[24,61,62] The second catalytic cycle is the CO-promoted redox catalytic cycle.[24] And, the final two pathways are the formate and carboxyl pathways with redox regeneration that we predicted previously to be of no importance.[24] All elementary reaction steps in these four pathways have been included in a microkinetic model as described previously.[24] The *gsl* (GNU Scientific Library) linear algebra library in C++ is used to solve the set of steady state reactor equations.

Next, we placed Gaussian PDF's representing the DFT energy uncertainty and their correlation on all intermediate and transition states. Transition states from collision theory are given a PDF with correction with a mean of +0.075 eV and a standard deviation of 0.075 eV. This mean correction suggests collision theory tends to underestimate transition state energies for adsorption. The selection of a standard deviation covers a sticking coefficient from zero to one where at 500 K a correction of 0.075 eV corresponds to a sticking coefficient of 0.175.

The standard deviations of all other intermediate and transition states are obtained by the results of our factor analysis[22] of the four functionals. Only one factor is used to explain the correlation structure between DFT energies. The DFT calculations with four functional results are listed in Table 3.1. The standard deviations are listed in Table 3.2. All standard deviations are from the element-wise square root of the diagonal of the covariance matrix obtained through factor analysis. Free energies of reaction and activation barriers which vary more widely are reflected by relatively larger standard deviations in Table 3.2.

The DFT-derived free energy pathways for this system including all intermediate and transition states need to end 0.40 eV higher to match the overall reaction thermodynamics (NIST value: $\Delta G_{rxn}^{WGS,}(523\ K) = -0.24\ eV$, average DFT: $\Delta G_{rxn}^{WGS,}(523\ K) = -0.64\ eV$, PBE: $\Delta G_{rxn}^{WGS,}(523\ K) = -0.67\ eV$, RPBE: $\Delta G_{rxn}^{WGS,}(523\ K) = -0.62\ eV$, HSE: $\Delta G_{rxn}^{WGS,}(523\ K) = -0.47\ eV$, M06L: $\Delta G_{rxn}^{WGS,}(523\ K) = -0.80\ eV$). A four-dimensional modified Diun is used to obtain four corrections $\zeta_{CO_2}, \zeta_{H_2}, \zeta_{H_2O}, \zeta_{CO}$ to gas molecule energies for CO_2, H_2, H_2O and CO, respectively. The following constraints are imposed on the four corrections.

$$\zeta_{CO_2} + \zeta_{H_2} + \zeta_{H_2O} + \zeta_{CO} = \delta \tag{12}$$

$$-0.4 \le \zeta_{CO_2}, \zeta_{CO} \le 0.4 \qquad -0.2 \le \zeta_{H_2}, \zeta_{H_2O} \le 0.2$$

We choose relatively large bounds on uncertainty of ±0.4 eV for CO and CO_2 due to the known challenges of DFT to predict both CO and CO_2 equally well;[4] while we choose a relatively small uncertainty bounds for H_2 and H_2O of ±0.2 eV. It can be argued

that our uncertainty of ±0.4 eV and ±0.2 eV, respectively, is too large, however, we advise to not underestimate uncertainties and note that the overall error of the average of our four functionals is 0.40 eV for the WGS at T = 523 K. The following linear transformation is used to alter the Diun distribution:

$$\zeta_{CO_2} = a + (b - a)\zeta^*_{CO_2}$$

$$\zeta_{H_2} = a + (b - a)\zeta^*_{H_2}$$

$$\zeta_{H_2O} = a + (b - a)\zeta^*_{H_2O}$$

$$\zeta_{CO} = a + (b - a)\zeta^*_{CO}$$

$$a = -0.4$$

$$b = 0.40 - 3a \tag{13}$$

This defines a four-dimensional Dirichlet distribution, called a simplex, where each correction is bounded below by a and above by b. This simplex is cut in order to provide the ranges of equation (12). Figure 3.2 illustrates samples from equation (13) following the ranges of equation (12) as a boxplot. Three samples are plotted on top of the boxplot to illustrate that each sample of gas DFT energy corrections sums to 0.40 eV.

Another coding strategy is included to ensure that energies in the UQ simulation are physical. Transition states used in transition state theory are set so that no activation barriers may be negative. This is accomplished by constraining transition state free energies to be at least equal to product or reactant state free energies whichever is greater.

3.5 RESULTS AND DISCUSSION

Figures 3.3a and 3.3b are free-energy diagrams which visualize the four functional results of the classical redox pathway and the CO-promoted redox pathway on our edge interface site model pictured in Figure 3.3c.[24] We observe that PBE and RPBE free energies are relative to the HSE and M06L results quite similar. Also, HSE and M06L free energies can deviate from the PBE and RPBE results by as much as 1 eV, particularly for transition states involving the formation of an oxygen vacancy in the TiO_2 support. Figure 4a shows the 95% confidence interval based upon average DFT energies. The 95% confidence interval is the mean of the four functionals plus or minus two standard deviations, indicated by dashed lines. The mean of the four functionals is the expected value, the solid line. Figure 3.4b shows uncertainties from the factor analysis with thermodynamics (Gibbs' free energy) correction for the gas molecules. The final and initial Gibbs' free energies are entirely certain in Figure 3.4b (the initial state is the reference energy and the final state is given by the reaction thermodynamics). In other words, the mean of the four functionals undergoes gas-phase corrections which correct the Gibbs' free energy of reaction to the NIST value which is assumed to have no uncertainty (the NIST uncertainty is significantly smaller than the DFT uncertainty).

Figure 3.5 displays overall TOF results and TOF results of individual catalytic cycles including constraints on (gas molecule) thermodynamics and correlations. The vertical dashed line is the experimental observation from Kalamaras et al.[44] The dominant catalytic cycle is predicted to be the CO-promoted redox pathway at these reaction conditions (P_{CO} = 0.03 atm, P_{H2O} = 0.1 atm, P_{CO2} = 0.06 atm, P_{H2} = 0.2 atm, T = 523 K).

This observation is in agreement with our previous conclusions about the dominant reaction mechanism on Pt_8/TiO_2 interface sites.[24] Figure 3.5 displays evidence of this trend by visual inspection that the probability density of the TOF of the CO-promoted redox pathway essentially lines up with the overall TOF probability density. This lining up signifies that there is hardly any difference between overall TOF and CO-promoted TOF. Although the classical redox pathway is not lined up with the overall TOF, the classical redox pathway is able to reach the experimentally observed TOF. It is evident that even when considering uncertainty, the formate and carboxyl pathway cannot lead to a significant WGS rate at edge sites of a Pt cluster on TiO_2 (110) and we can exclude the possibility that the WGS proceeds through these pathways at interface edge sites.

To statistically formalize the importance of one pathway over another, the KL divergence is taken of the CO-promoted redox catalytic cycle TOF and the classical redox catalytic cycle TOF using the overall TOF as a reference over the temperature range of 473 to 673 K as shown in Figure 3.6. The raw numerical data from the model must be transformed and entered into the equation for KL divergence, Equation (11). A smaller KL divergence reveals that the individual catalytic cycle TOF is closer to the overall TOF. As a note, any plotting software/language which has kernel density estimation capability could create the plots which MATLAB creates. As a clarification, MATLAB is only used for plotting the data in this work. QUESO, gsl and other C++ libraries are used to build and run the model for the generation of data. Python is used to obtain confidence intervals and correlation structure by factor analysis.[63] At a reaction temperature of 523 K, the KL divergence of the CO-promoted redox catalytic cycle is 0.0237 which is significantly less than the 0.2211 KL divergence of the classical redox

cycle. Therefore we have high confidence that the CO-promoted catalytic cycle is indeed dominant. The CO-promoted redox catalytic cycle dominates within the temperature range of 473 K to at least 600 K, at which temperature we observe slowly a change in reaction mechanism (the KL for both pathways becomes equivalent at 608 K). This change in dominant catalytic cycle is likely due to the effect of temperature on the CO binding energy and therefore the surface coverage fraction of the extra adsorbed CO molecule needed in the CO-promoted cycle. We also analyzed the reaction pathways at a temperature of 623 K and Figure 3.7 illustrates the PDF's of the two cycles and overall TOF at T=623 K. Here, the classical redox TOF is very close to overall TOF and it becomes very challenging to identify the dominant reaction mechanism by visual inspection. However, it is still apparent that the formate and carboxyl mechanism lead to small TOFs and these pathways are not relevant for our Pt/TiO_2 catalyst model.

Next, we analyzed our predicted apparent activation barrier and reaction orders. The apparent activation barrier of our active site model captures the experiment as evidenced by Figure 3.8 although it has wide uncertainty of over 2.5 eV (the apparent activation barrier has been obtained in the temperature interval from 473 to 673 K). This wide uncertainty is a result of the significant uncertainty of the DFT predicted Gibbs' free energies (Figure 3.3 and 3.4), particularly for processes involving the formation of an oxygen vacancy on the TiO_2 surface. In other words, agreement between experimental and computational apparent activation barriers is not a sufficient measure to validate the computational model. We note however that there is a correlation between the TOF and apparent activation barrier such that when considering only the parameter space with results that are close to the experimental TOF, the uncertainty in apparent activation

barrier is significantly reduced and relatively close to the experimentally observed barrier. Finally, Figure 3.9 shows reaction order PDF's with experiments reported in the literature at reaction conditions of P_{CO} = 0.03 atm, P_{H2O} = 0.1 atm, P_{CO2} = 0.06 atm, P_{H2} = 0.2 atm, T = 523 K.[15] The experimental H_2 reaction order is reasonably captured well by its PDF. H_2 and in fact all reaction orders display some degree of bimodality due to the large uncertainty in the DFT energies which leads to various states being rate controlling in different samples - for example the reaction order for H_2O can be zero or one (or anywhere in between) when the uncertainty in DFT is accounted. Also, the CO reaction order PDF is able to capture the experiment and the H_2O reaction order PDF captures the experimental observation with most probability lying between 0 and 1. Finally, the CO_2 reaction order PDF captures the experimental value at its mode at 0. Overall, we observe wide ranges of predicted reaction orders with bimodality that capture the experimental data. In other words, our model based on DFT and transition state theory captures all experimental data (indeed there exist free energy corrections that lead to kinetic parameters that all agree concurrently with experimental data); however, the PDFs for TOF, apparent activation barrier and reaction orders are relatively wide such that DFT is still challenged with predicting the absolute activity of active sites at the interface of a transition metal particle and a reducible oxide support. Encouragingly though the prediction of the dominant reaction pathway/mechanism can be made with high confidence for even complex active site models. Clearly, the formate and carboxyl mechanisms play no role at the investigated active site model and the CO-promoted redox pathway is the dominant reaction mechanism at low temperatures.

3.6 CONCLUSIONS

A general framework has been proposed for uncertainty quantification of computational catalysis studies. The usefulness of correlating DFT uncertainties using a factor analysis has been shown. A Dirichlet distribution has been used to perform a thermodynamics correction. Case study results have been presented and they suggest DFT is accurate for producing relative results such as the dominant catalytic cycle. Kullback-Leibler divergence has been presented for identification of the dominant catalytic cycle. For the case study of the water-gas shift reaction at the edge interface site of our Pt_8/TiO_2 catalyst model, a combination of generalized gradient approximation functionals, a hybrid functional, and a Minnesota functional have been entered into the factor analysis for DFT uncertainty and correlation structure among states and transition states. The experimental data of TOF, apparent activation barrier, and reaction orders of CO, H_2O, CO_2 and H_2 all fall within the uncertainty due to DFT illustrating that our active site model might capture all relevant characteristics of the active sites in the experimental catalyst. Two catalytic cycles, formate and carboxylate, have been ruled out from playing a dominant role in TOF. Furthermore, the Kullback-Leibler divergence formalizes that the CO-promoted cycle is dominant over the classical redox cycle. Although, above 600 K the two cycles become equivalent in dominance as measured by Kullback-Leibler divergence. A four-dimensional Dirichlet distribution has been applied to the gas molecules CO, H_2O, CO_2 and H_2 which corrects the overall Gibbs' free energy of reaction to NIST data, i.e., the reaction is less thermodynamically downhill with the Dirichlet distribution correction. Uncertainty quantification *forward problems* such as the general framework and case study communicated here are recommended for other

computational catalysis models in order to account for the inexact nature of DFT and can of course be extended to include other uncertainties in the model if they are believed to be of high importance such as lateral interactions and limitations of harmonic transition state theory. In future work, a significant reduction in uncertainty may be accomplished by using Bayesian statistical tools to perform an *inverse problem* to learn about DFT energies and their correlation from experiments.

3.7 ACKNOWLEDGEMENTS

The authors would like to acknowledge the National Science Foundation (NSF) CAREER award grant # NSF CBET-1254352 and the 2014 Eastman fellowship. The US Department of Energy facilities located at the National Energy Research Scientific Computing Center (NERSC) and at EMSL, located at Pacific Northwest National Laboratory are gratefully acknowledged for their computing resources used in this work. Furthermore, a portion of this research was performed with XSEDE resources provided by the National Institute for Computational Sciences (NICS), San Diego Supercomputer Center (SDSC), and Texas Advanced Computing Center (TACC) under grant number TG-CTS090100.

3.8 REFERENCES

[1] Hansgen, D. A.; Vlachos, D. G.; Chen, J. G. Using First Principles to Predict Bimetallic Catalysts for the Ammonia Decomposition Reaction. *Nat. Chem.* **2010**, *2*, 484-489.

[2] Studt, F.; Pedersen, F. A.; Bligaard, T.; Sørensen, R. Z.; Christensen, C. H.; Nørskov, J. K. Identification of Non-Precious Metal Alloy Catalysts for Selective Hydrogenation of Acetylene. *Science* **2008**, *320*, 1320-1322.

[3] Honkala, K.; Hellman, A.; Remediakis, I. N.; Logadottir, A.; Carlsson, A.; Dahl, S.; Christensen, C. H.; Nørskov, J. K. Ammonia Synthesis from First-Principles Calculations. *Science* **2005**, *307*, 555-558.

[4] Mortensen, J. J.; Kaasbjerg, K.; Frederiksen, S. L.; Norskov, J. K.; Sethna, J. P.; Jacobsen, K. W. Bayesian Error Estimation in Density-Functional Theory. *Phys. Rev. Lett.* **2005**, *95*, 216401.

[5] Cramer, C. J. *Essentials of Computational Chemistry: Second Edition*; John Wiley and Sons, Inc.: Hoboken, New Jersey, 2007.

[6] Hanke, F. Sensitivity Analysis and Uncertainty Calculation for Dispersion Corrected Density Functional Theory. *J. Comput. Chem.* **2011**, *32*, 1424-1430.

[7] Sutton, J. E.; Vlachos, D. G. Error Estimates in Semi-Empirical Estimation Methods of Surface Reactions. *J. Catal.* **2013**, *297*, 202-216.

[8] Sutton, J. E.; Panagiotopoulou, P.; Verykios, X. E.; Vlachos, D. G. Combined DFT, Microkinetic, and Experimental Study of Ethanol Steam Reforming on Pt. *J. Phys. Chem. C.* **2013**, *117*, 4691-4706.

[9] Peterson, A. A.; Pedersen, F. A.; Studt, F.; Rossmeisl, J.; Nørskov, J. K. How Copper Catalyzes the Electroreduction of Carbon Dioxide into Hydrocarbon Fuels. *Energy Environ. Sci.* **2010**, *3*, 1311-1315. Supporting information.

[10] Afeefy, H.; Liebman, J.; Stein, S. NIST Chemistry WebBook, NIST Standard Reference Database Number 69. (National Institute of Standards and Technology, Gaithersburg MD, USA 2010).

[11] Petzold, V.; Bligaard, T. K.; Jacobsen, W. Construction of New Electronic Density Functionals with Error Estimation Through Fitting. *Top. Catal*. **2012**, *55*, 402-417.

[12] Medford, A. J.; Wellendorff, J.; Vojvodic, A.; Studt, F.; Pedersen, F. A.; Jacobsen, K. W.; Bligaard, T.; Norskov, J. K. Assessing the Reliability of Calculated Catalytic Ammonia Synthesis Rates. *Science* **2014**, *345*, 197-200.

[13] Wellendorff, J.; Lundgaard, K. T.; Jacobsen, K. W.; Bligaard, T.; mBEEF: An Accurate Semi-Local Bayesian Error Estimation Density Functional. *J. Chem. Phys.* **2014**, *140*, 144107.

[14] Wellendorff, J.; Lundgaard, K. T.; Mogelhoj, A.; Petzold, V.; Landis, D. D.; Norskov, T. Bligaard, K. W. Jacobsen, Density Functionals for Surface Science: Exchange-Correlation Model Development with Bayesian Error Estimation. Phys. Rev. B., **2012**, *85*, 235149.

[15] Kulik, H. J.; Cococcioni, M.; Scherlis, D. A.; Marzari, N. Density Functional Theory in Transition-Metal Chemistry: A Self-Consistent Hubbard U Approach. *Phys. Rev. Lett.*, **2006**, *97*,103001.

[16] Kulik, H. J. Perspective: Treating Electron Over-Delocalization with the DFT+U Method. *J. Chem. Phys.* **2015**, *142*, 240901.

[17] Perdew, J. P.; Burke, K.; Ernzerhof, M. Generalized Gradient Approximation Made Simple. *Phys. Rev. Lett.* **1996**, *77*, 3865-3868.
[18] Hammer, B.; Hansen, L. B.; Norskov, J. K. Improved Adsorption Energetics within Density- Functional Theory using revised Perdew-Burke-Ernzerhof Functionals. *Phys. Rev. B*. **1999**, *59*, 7413-7421.
[19] Zhang, Y.; Yang, W. Comment on "Generalized Gradient Approximation Made Simple". *Phys. Rev. Lett.* 1998, **80**, 890.
[20] Heyd, J.; Scuseria, G. E.; Ernzerhof, M. Hybrid Functionals Based on a Screened Coulomb Potential. *J. Chem. Phys.* **2003**, *118*, 8207.
[21] Zhao, Y.; Truhlar, D. G. A New Local Density Functional for Main-Group Thermochemistry, Transition Metal Bonding, Thermochemical Kinetics, and Noncovalent Interactions. *J. Chem. Phys.* **2006**, *125*, 194101.
[22] Rencher, A. C. *Methods of Multivariate Analysis*; John Wiley and Sons, Inc.: Hoboken, New Jersey, 2007.
[23] Plessis, S.; Carrasco, N.; Pernot, P. Knowledge-Based Probabilistic Representations Of Branching Ratios in Chemical Networks: The Case of Dissociative Recombinations. *J.Chem. Phys.* **2010**, *133*, 134110.
[24] Ammal, S. C.; A. Heyden, Origin of the Unique Activity of Pt/TiO2 Catalysts for the Water Gas Shift Reaction. *J. Catal*. **2013**, *306*, 78-90.
[25] Oettel, C.; Rihko-Struckmann, L.; Sundmacher, K.; Characterisation of the Electrochemical Water Gas Shift Reactor (EWGSR) Operated with Hydrogen and Carbon Monoxide Rich Feed Gas. *Int. J. Hydrogen Energy* **2012**, *37*, 11759-11771.
[26] Haryanto, A.; Fernando, S.; Murali, N.; Adhikari, S. Current Status of Hydrogen Production Techniques by Steam Reforming of Ethanol: A Review. *Energy Fuels* **2005**, *19*, 2098- 2106.
[27] Holladay, J. D.; Hu, J.; King, D. L.; Wang, Y. An Overview of Hydrogen Production Technologies. *Catal. Today* **2009**, *139*, 244-260.
[28] Cortright, R. D.; Davda, R. R.; Dumesic, J. A. Hydrogen from Catalytic Reforming of Biomass-Derived Hydrocarbons in Liquid Water. *Nature* **2002**, *418*, 964-967.
[29] Song, C. S. Fuel Processing for Low-Temperature and High-Temperature Fuel Cells: Challenges, and Opportunities for Sustainable Development in the 21st Century. *Catal. Today* **2002**, *77*, 17-49.
[30] D. L. Trimm, Minimisation of Carbon Monoxide in a Hydrogen Stream for Fuel Cell Application. *Appl.Catal. A*. **2005**, *296*, 1-11.
[31] Bartholomew, C. H.; Farrauto, R. J. *Fundamentals of Industrial Catalytic Processes*; Wiley: Hoboken, N.J. 2006.
[32] Liu, Y.; Fu, Q.; Flytzani-Stephanopoulos, M. Preferential Oxidation of CO in H2 over CuO-CeO_2 Catalysts. *Catal. Today* **2004**, *93-95***,** 241-246.
[33] Suh, D. J.; Kwak, C.; Kim, J. H.; Kwon, S. M.; Park, T. J.; Removal of Carbon Monoxide from Hydrogen-Rich Fuels by Selective Low-Temperature Oxidation over Base Metal Added Platinum Catalysts. *J. Power Sources* **2005**, *142*, 70-74.
[34] Haruta, M.; Yamada, N.; Kobayashi, T.; Iijima, S. Gold Catalysts Prepared by Coprecipitation for Low-Temperature Oxidation of Hydrogen and of Carbon Monoxide. *J. Catal*. **1989**, *115*, 301-309.
[35] Bond, G. C.; Thompson, D. T. Catalysis by Gold. *Catal. Rev. Sci. Eng*. **1999**, *41*, 319-388.

[36] Haruta, M. Gold as a Novel Catalyst in the 21st Century: Preparation, Working Mechanism and Applications. *Gold Bull.* **2004**, *37*, 27-36.
[37] Thinon, O.; Rachedi, K.; Diehl, F.; Avenier, P.; Schuurman, Y. Kinetics and Mechanism of the Water–Gas Shift Reaction Over Platinum Supported Catalysts. *Top. Catal.* **2009**, *52*, 1940–1945.
[38] Azzam, K. G.; Babich, I. V.; Seshan, K.; Lefferts, L.; A Bifunctional Catalyst for the Single-Stage Water–Gas Shift Reaction in Fuel Cell Applications. Part 2. Roles of the Support and Promoter on Catalyst Activity and Stability *J. Catal.* **2007**, *251*, 163-171.
[39] Kalamaras, C. M.; Gonzalez, I. D.; Navarro, R. M.; Fierro, J. L. G.; Efstathiou, A. M. Effects of Reaction Temperature and Support Composition on the Mechanism of Water– Gas Shift Reaction over Supported-Pt Catalysts. *J. Phys. Chem. C.* **2011**, *115*, 11595-11610.
[40] Williams, W. D.; Shekhar, M.; Lee, W. S.; Kispersky, V.; Delgass, W. N.; Ribeiro, F. H.; Kim, S. M.; Stach, E. A.; Miller, J. T.; Allard, L. F. Metallic Corner Atoms in Gold Clusters Supported on Rutile Are the Dominant Active Site during Water−Gas Shift Catalysis. *J. Am. Chem. Soc.* **2010**, *132*, 14018-14020.
[41] Rodriguez, J. A.; Evans, J.; Graciani, J.; Park, J. B.; Liu, P.; Hrbek, J.; Sanz, J. F. High Water−Gas Shift Activity in TiO_2(110) Supported Cu and Au Nanoparticles: Role of the Oxide and Metal Particle Size. *J. Phys.Chem. C.* **2009**, *113*, 7364-7370.
[42] Vignatti, C.; Avila, M. S.; Apesteguia, C. R.; Garetto, T. F.; Catalytic and DRIFTS Study of the WGS Reaction on Pt-Based Catalysts. *Int. J. Hydrogen Energy* **2010**, *35*, 7302-7312.
[43] Azzam, K. G.; Babich, I. V.; Seshan, K.; Lefferts, L. Bifunctional Catalysts for Single-Stage Water–Gas Shift Reaction in Fuel Cell Applications.: Part 1. Effect of the Support on the Reaction Sequence. *J. Catal.* **2007**, *251*, 153-162.
[44] Kalamaras, C. M.; Panagiotopoulou, P.; Kondarides, D. I.; Efstathiou, A. M.; Kinetic and Mechanistic Studies of the Water–Gas Shift Reaction on Pt/TiO_2 Catalyst. *J. Catal*. **2009**, *264*, 117-129.
[45] Green, I. X.; Tang, W. J.; Neurock, M.; Yates, J. T.; Spectroscopic Observation of Dual Catalytic Sites During Oxidation of CO on a Au/TiO_2 Catalyst. *Science* **2011**, *333***,** 736-739.
[46] Rashkeev, S. N.; Lupini, A. R.; Overbury, S. H.; Pennycook, S. J.; Pantelides, S. T. Role of the Nanoscale in Catalytic CO Oxidation by Supported Au and Pt Nanostructures. *Phys. Rev. B*, **2007**, *76*, 035438.
[47] Pazmino, J. H.; Shekhar, M.; Williams, W. D.; Akatay, M. C.; Miller, J. T.; Delgass, W. N.; Ribeiro, F. H. Metallic Pt as Active Sites for the Water–Gas Shift Reaction on Alkali Promoted Supported Catalysts. *J. Catal.* **2012**, *286*, 279-2861.
[48] Ding, K.; Gulec, A.; Johnson, A. M.; Schweitzer, N. M.; Stucky, G. D.; Marks, L. D.; Stair, P. C. Identification of Active Sites in CO Oxidation and Water-Gas Shift over Supported Pt Catalysts. *Science* **2015**, *350*, 189-192.
[49] Fu, Q.; Saltsburg, H.; Stephanopoulos, M. F. Active Nonmetallic Au and Pt Species On Ceria-Based Water-Gas Shift Catalysts. *Science* **2003**, *301*, 935-938.
[50] Yang, M.; Liu, J.; Lee, S.; Zugic, B.; Huang, J.; Allard, L. F.; Flytzani-Stephanopoulos, M. A Common Single-Site Pt(II)–O(OH)x– Species Stabilized by Sodium on "Active" and "Inert" Supports Catalyzes the Water-Gas Shift Reaction.

J. Am. Chem. Soc. **2015**, *137*, 3470-3473.
[51] Ammal, S. C.; Heyden, A.; Modeling the Noble Metal/TiO_2 metal/TiO_2(110) Interface with Hybrid DFT Functionals: A Periodic Electrostatic Embedded Cluster Model Study. *J. Chem. Phys.* **2010**, *133*, 164703.
[52] Ammal, S. C.; Heyden, A. Water–Gas Shift Catalysis at Corner Atoms of Pt Clusters in Contact with a TiO_2 (110) Support Surface. *ACS Catal.* **2014**, *4*, 3654-3662.
[53] Rubin, D. B.; Thayer, D. T. EM Algorithms for ML Factor Analysis. *Psychometrika*, **1982**, *47*, 69-76.
[54] Terejanu, G.; Upadhyay, R. R.; Miki, K. Bayesian Experimental Design for the Active Nitridation of Graphite by Atomic Nitrogen. *Exp. Therm. Fluid Sci.* **2012**, *36*, 178-193.
[55] Kullback, S.; Leibler, R. A. On Information and Sufficiency. *Ann. Math. Statist.* **1951**, *22*, 79-86.
[56] Kohn, W.; Sham, L. J. Self-Consistent Equations Including Exchange and Correlation Effects. *Phys. Rev.* **1965**, *140*, A1133.
[57] Adamo, C.; Scuseria, G. E.; Barone, V. Accurate Excitation Energies from Time-Dependent Density Functional Theory: Assessing the PBE0 Model. *J. Chem. Phys.* **1999**, *111*, 2889.
[58] Xu, Z.; Joshi, Y. V.; Raman, S.; Kitchin, J. R. Accurate Electronic and Chemical Properties of 3d Transition Metal Oxides Using a Calculated Linear Response U and a DFT + U(V) Method. *J. Chem. Phys.* **2015**, *142*, 144701.
[59] Henkelman, G.; Uberuaga, B. P.; Jonsson, H.; A Climbing Image Nudged Elastic Band Method for Finding Saddle Points and Minimum Energy Paths. *J. Chem. Phys*. **2000**, *113*, 9901.
[60] Heyden, A.; Bell, A. T.; Keil, F. J. Efficient Methods for Finding Transition States in Chemical Reactions: Comparison of Improved Dimer Method and Partitioned Rational Function Optimization Method. *J. Chem. Phys*. **2005**, *123*, 224101.
[61] Iida, H.; Igarashi, A. Characterization of a Pt/TiO_2 (Rutile) Catalyst for Water Gas Shift Reaction at Low-Temperature. *Appl. Catal. A*. **2006**, *298*, 152-160.
[62] Panagiotopoulou, P.; Christodoulakis, A.; Kondarides, D. I.; Boghosian, S. Particle Size Effects on the Reducibility of Titanium Dioxide and its Relation to the Water Gas Shift Activity of Pt/TiO_2 Catalysts. *J. Catal.* **2006**, *240*, 114-125.
[63] We plan to make our code publically available during summer 2016.

3.9 TABLES AND FIGURES

Table 3.1 Four functional results for the Gibbs' free energy of various states of our model originally reported by Ammal et al.[24] A temperature of 523 K has been used for the free energy calculations at a reference pressure of 1 atm for each gas molecule. All energies are with reference to state: $*_{Pt}$-O_{int} + 2CO(g) + H_2O(g). Transition states are symbolized by the reaction equation they belong to.

Intermediate or Transition State	**G (eV)**			
	PBE	**RPBE**	**HSE**	**M06L**
$*_{Pt}$-O_{int} + 2CO(g) + H_2O(g)	0.000	0.000	0.000	0.000
$*_{Pt}$-O_{int} + 2CO(g) + H_2O(g)→ CO_{Pt}-O_{int} + CO(g) + H_2O(g)	0.000	0.000	0.000	0.000
CO_{Pt}-O_{int} + CO(g) + H_2O(g)	0.182	0.273	0.365	0.768
CO_{Pt}-O_{int} + CO(g) + H_2O(g) → $CO_{2(Pt\text{-}int)}$ + CO(g) + H_2O(g)	0.733	0.951	0.940	1.399
$CO_{2(Pt\text{-}int)}$ + CO(g) + H_2O(g)	0.605	0.892	0.748	0.957
$CO_{2(Pt\text{-}int)}$ + CO(g) + H_2O(g) → $*_{Pt}$-V_{int} + CO_2(g) + CO(g) + H_2O(g)	1.829	1.976	2.803	2.095
$*_{Pt}$-V_{int} + CO(g) + H_2O(g) + CO_2(g)	0.489	0.408	0.868	1.074
$*_{Pt}$-V_{int} + CO(g) + H_2O(g) + CO_2(g)→ $*_{Pt}$-$2OH_{int}$ + CO(g) + CO_2(g)	1.020	1.263	2.044	1.395
$*_{Pt}$-$2OH_{int}$ + CO(g) + CO_2(g)	0.121	0.462	0.667	-0.353
$*_{Pt}$-$2OH_{int}$ + CO(g) + CO_2(g) → H_{Pt}-OH_{int} + O_{int} + CO(g) + CO_2(g)	0.697	0.905	1.147	1.349
H_{Pt}-OH_{int} + $*_{Pt}$ + CO(g) + CO_2(g)	0.374	0.507	0.736	0.842
H_{Pt}-OH_{int} + $*_{Pt}$ + CO(g) + CO_2(g) → $2H_{Pt}$-O_{int} + CO(g) + CO_2(g)	1.036	1.424	1.853	1.339
$2H_{Pt}$-O_{int} + CO(g) + CO_2(g)	-0.097	0.245	0.309	0.175
$2H_{Pt}$-O_{int} + CO(g) + CO_2(g) → $*_{Pt}$-O_{int} +$*_{Pt}$ +H_2(g) + CO(g) + CO_2(g)	-0.097	0.245	0.309	0.175
$*_{Pt}$-O_{int} +$*_{Pt}$ +H_2(g) + CO(g) + CO_2(g)	-0.667	-0.622	-0.468	-0.803
$CO_{2(Pt\text{-}int)}$ + CO(g) + H_2O(g) → CO_{Pt}-$CO_{2(int)}$ + H_2O(g)	0.605	0.892	0.748	0.957
CO_{Pt}-$CO_{2(int)}$ + H_2O(g)	0.540	0.780	0.879	1.318
CO_{Pt}-$CO_{2(int)}$ + H_2O(g) → CO_{Pt}-V_{int} + CO_2(g) + H_2O(g)	1.272	1.323	1.851	2.306
CO_{Pt}-V_{int} +O_{int} + H_2O(g) + CO_2(g)	-0.305	-0.263	0.607	0.497
CO_{Pt}-V_{int} +O_{int} H_2O(g) + CO_2(g) → CO_{Pt}-$2OH_{int}$ + CO_2(g)	0.924	1.050	1.496	1.958

CO_{Pt}-$2OH_{int}$ + O_s + CO_2(g)	0.313	0.673	0.957	0.570
CO_{Pt}-$2OH_{int}$ + O_s + CO_2(g) → CO_{Pt}-OH_{int}-O_{int}-OH_s + CO_2(g)	0.771	1.111	1.206	1.651
CO_{Pt}-OH_{int}-O_{int}-OH_s + O_{int} + CO_2 (g)	0.379	0.571	0.658	1.094
CO_{Pt}-OH_{int}-O_{int}-OH_s + O_{int} + CO_2 (g) → CO_{Pt}-OH_{int}-O_{int}-OH_{int} + O_s + CO_2 (g)	0.869	0.949	1.258	1.920
CO_{Pt}-OH_{int}-O_{int}-OH_{int} + $*_{Pt}$ + CO_2 (g)	0.236	0.517	0.777	0.514
CO_{Pt}-OH_{int}-O_{int}-OH_{int} + $*_{Pt}$ + CO_2 (g)→ CO_{Pt}-OH_{int}-O_{int}-H_{Pt} + O_{int} + CO_2 (g)	0.262	0.397	0.648	1.344
CO_{Pt}-OH_{int}-O_{int}-H_{Pt} + $*_{Pt}$ + CO_2 (g)	-0.364	-0.097	-0.174	0.219
CO_{Pt}-OH_{int}-O_{int}-H_{Pt} + $*_{Pt}$ + CO_2 (g)→ CO_{Pt}-O_{int}-$2H_{Pt}$ + O_{int} + CO_2 (g)	-0.034	0.148	0.296	1.106
CO_{Pt}-O_{int}-$2H_{Pt}$ + CO_2 (g)	-0.761	-0.483	-0.612	0.102
CO_{Pt}-O_{int}-$2H_{Pt}$ + CO_2 (g)→ CO_{Pt}-O_{int} + $2*_{Pt}$ + CO_2 (g)+ H_2 (g)	-0.761	-0.483	-0.612	0.102
CO_{Pt}-O_{int} + $2*_{Pt}$ + CO_2 (g)+ H_2 (g)	-0.485	-0.349	-0.103	-0.034

Table 3.2 Standard deviations of Gaussian uncertainties of Gibbs' free energies obtained by factor analysis and setting adsorption/desorption uncertainties. Standard deviations correspond to how varied the four functional results (free energies) listed in Table 1 are. All energies are with reference to state: $*_{Pt}\text{-}O_{int} + 2CO(g) + H_2O(g)$. Transition states are symbolized by the reaction equation they belong to.

Intermediate or Transition State	**Standard Deviation (eV)**
$*_{Pt}\text{-}O_{int} + 2CO(g) + H_2O(g)$	0.000
$*_{Pt}\text{-}O_{int} + 2CO(g) + H_2O(g) \rightarrow CO_{Pt}\text{-}O_{int} + CO(g) + H_2O(g)$	0.075
$CO_{Pt}\text{-}O_{int} + CO(g) + H_2O(g)$	0.224
$CO_{Pt}\text{-}O_{int} + CO(g) + H_2O(g) \rightarrow CO_{2(Pt\text{-}int)} + CO(g) + H_2O(g)$	0.243
$CO_{2(Pt\text{-}int)} + CO(g) + H_2O(g)$	0.136
$CO_{2(Pt\text{-}int)} + CO(g) + H_2O(g) \rightarrow *_{Pt}\text{-}V_{int} + CO_2(g) + CO(g) + H_2O(g)$	0.374
$*_{Pt}\text{-}V_{int} + CO(g) + H_2O(g) + CO_2(g)$	0.273
$*_{Pt}\text{-}V_{int} + CO(g) + H_2O(g) + CO_2(g) \rightarrow *_{Pt}\text{-}2OH_{int} + CO(g) + CO_2(g)$	0.379
$*_{Pt}\text{-}2OH_{int} + CO(g) + CO_2(g)$	0.386
$*_{Pt}\text{-}2OH_{int} + CO(g) + CO_2(g) \rightarrow H_{Pt}\text{-}OH_{int} + O_{int} + CO(g) + CO_2(g)$	0.246
$H_{Pt}\text{-}OH_{int} + *_{Pt} + CO(g) + CO_2(g)$	0.184
$H_{Pt}\text{-}OH_{int} + *_{Pt} + CO(g) + CO_2(g) \rightarrow 2H_{Pt}\text{-}O_{int} + CO(g) + CO_2(g)$	0.292
$2H_{Pt}\text{-}O_{int} + CO(g) + CO_2(g)$	0.155
$2H_{Pt}\text{-}O_{int} + CO(g) + CO_2(g) \rightarrow *_{Pt}\text{-}O_{int} + *_{Pt} + H_2(g) + CO(g) + CO_2(g)$	0.075
$*_{Pt}\text{-}O_{int} + *_{Pt} + H_2(g) + CO(g) + CO_2(g)$	0.119
$CO_{2(Pt\text{-}int)} + CO(g) + H_2O(g) \rightarrow CO_{Pt}\text{-}CO_{2(int)} + H_2O(g)$	0.136
$CO_{Pt}\text{-}CO_{2(int)} + H_2O(g)$	0.282
$CO_{Pt}\text{-}CO_{2(int)} + H_2O(g) \rightarrow CO_{Pt}\text{-}V_{int} + CO_2(g) + H_2O(g)$	0.423
$CO_{Pt}\text{-}V_{int} + O_{int} + H_2O(g) + CO_2(g)$	0.420
$CO_{Pt}\text{-}V_{int} + O_{int}\ H_2O(g) + CO_2(g) \rightarrow CO_{Pt}\text{-}2OH_{int} + CO_2(g)$	0.407
$CO_{Pt}\text{-}2OH_{int} + O_s + CO_2(g)$	0.231

CO_{Pt}-$2OH_{int}$ + O_s + CO_2(g) → CO_{Pt}-OH_{int}-O_{int}-OH_s + CO_2(g)	0.314
CO_{Pt}-OH_{int}-O_{int}-OH_s + O_{int} + CO_2 (g)	0.262
CO_{Pt}-OH_{int}-O_{int}-OH_s + O_{int} + CO_2 (g) → CO_{Pt}-OH_{int}-O_{int}-OH_{int} + O_s + CO_2 (g)	0.414
CO_{Pt}-OH_{int}-O_{int}-OH_{int} + $*_{Pt}$ + CO_2 (g)	0.191
CO_{Pt}-OH_{int}-O_{int}-OH_{int} + $*_{Pt}$ + CO_2 (g) → CO_{Pt}-OH_{int}-O_{int}-H_{Pt} + O_{int} + CO_2 (g)	0.417
CO_{Pt}-OH_{int}-O_{int}-H_{Pt} + $*_{Pt}$ + CO_2 (g)	0.210
CO_{Pt}-OH_{int}-O_{int}-H_{Pt} + $*_{Pt}$ + CO_2 (g) → CO_{Pt}-O_{int}-$2H_{Pt}$ + O_{int} + CO_2 (g)	0.436
CO_{Pt}-O_{int}-$2H_{Pt}$ + CO_2 (g)	0.327
CO_{Pt}-O_{int}-$2H_{Pt}$ + CO_2 (g) → CO_{Pt}-O_{int} + $2*_{Pt}$ + CO_2 (g)+ H_2 (g)	0.075
CO_{Pt}-O_{int} + $2*_{Pt}$ + CO_2 (g)+ H_2 (g)	0.398

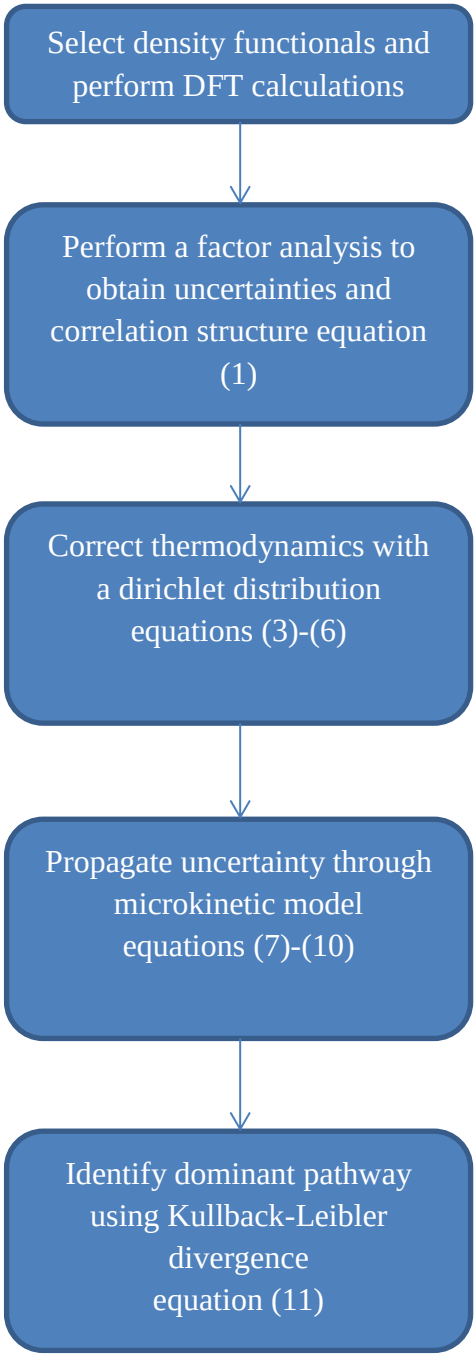

Figure 3.1 Flowchart of general framework for uncertainty quantification of computational catalysis results presented in section 3.2.

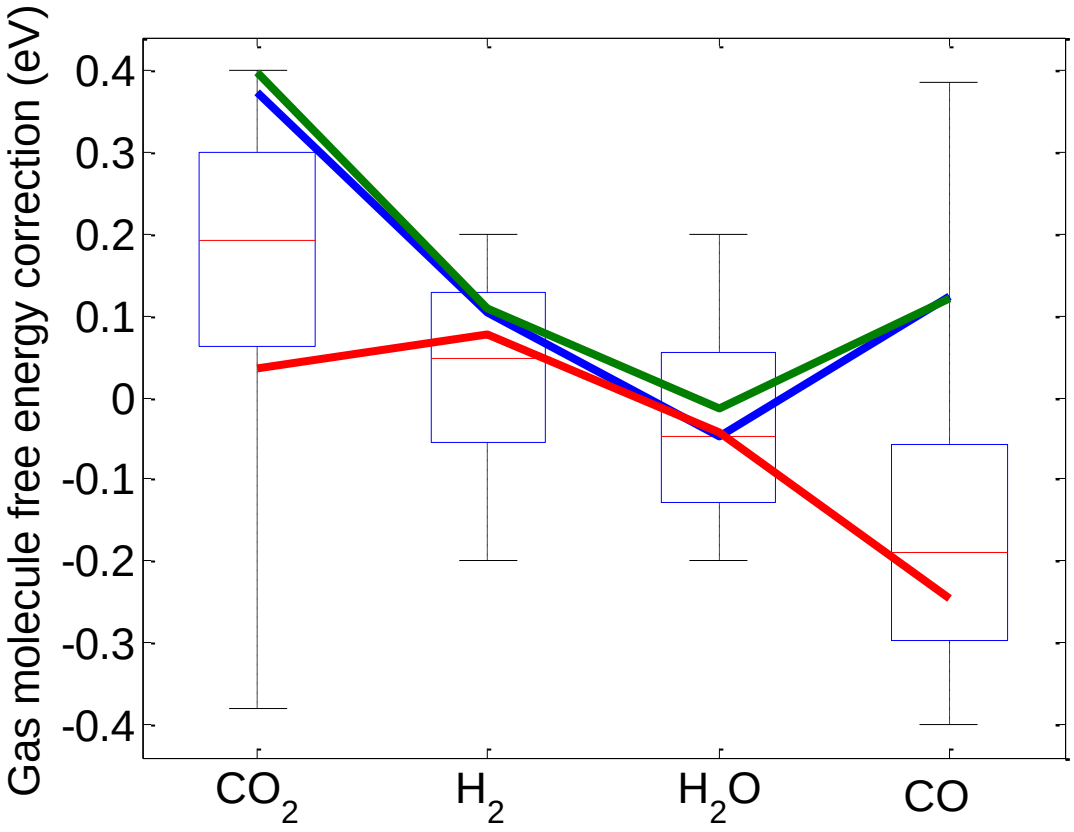

Figure 3.2 Boxplot of gas molecule free energy corrections with three samples shown on top. The overall reaction thermodynamics may be expressed as $\sum_i \nu_i G_i$ where ν_i is the stoichiometric coefficient of gas molecule i. Overall reaction Gibbs' free energies are $\Delta G^{error} = G_{CO2}^{error} + G_{H2}^{error} - G_{H2O}^{error} - G_{CO}^{error}$. The three samples illustrate that ΔG^{error} is +0.40 eV. For example, a possible sample from the four-dimensional Dirichlet PDF is 0.15, 0.07, -0.01, -0.17 (eV) for CO_2, H_2, H_2O and CO because it falls within the constraints and sums (using stoichiometric coefficients) to +0.40 eV. If a three-dimensional slice were taken of this four-dimensional space the samples would appear uniformly spread.

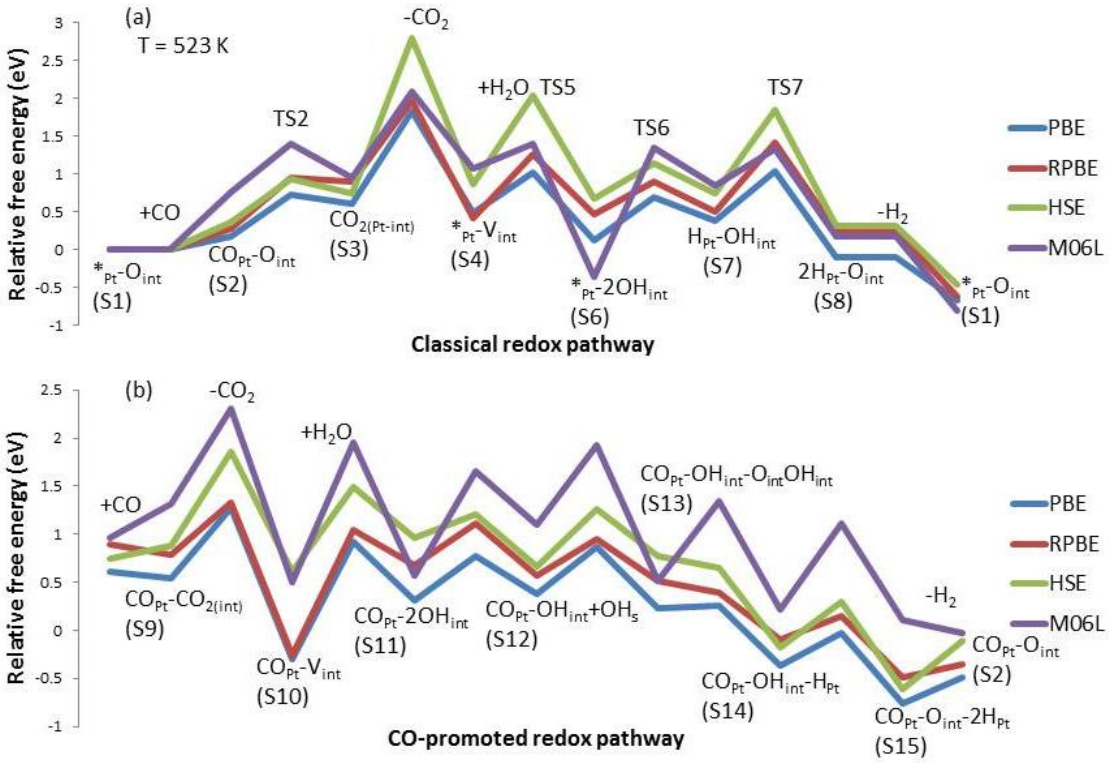

(c)

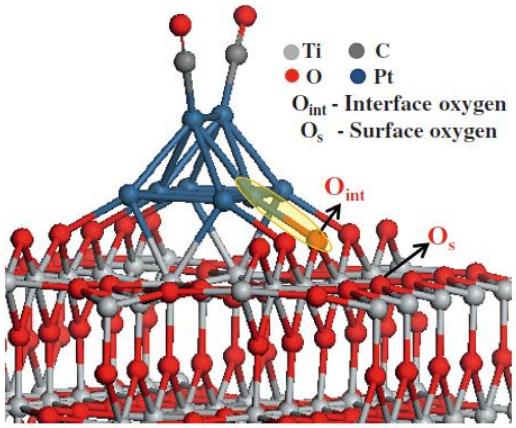

Figure 3.3a-c. Free energy diagrams of the classical redox pathway (a) and CO-promoted redox pathway (b) computed by four DFT functionals at a reaction temperature of 523 K. Figure c is a picture of the active edge interface site model adapted from our earlier work[24].

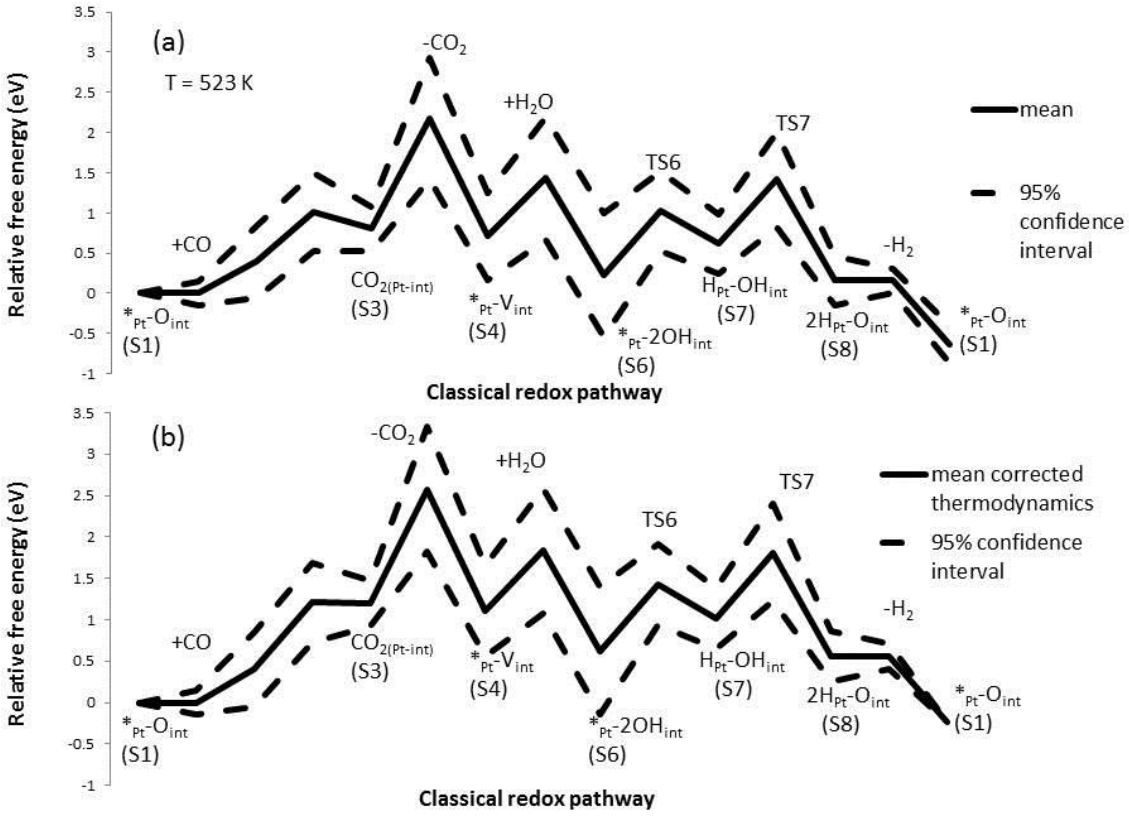

Figure 3.4a-b. Relative Gibbs' free energy diagram of the classical redox cycle with 95% confidence intervals from factor analysis. Figure b shows the dirichlet pdf results correcting the thermodynamics (Gibbs' free energy of reaction) to the NIST value at the end of the catalytic cycle.

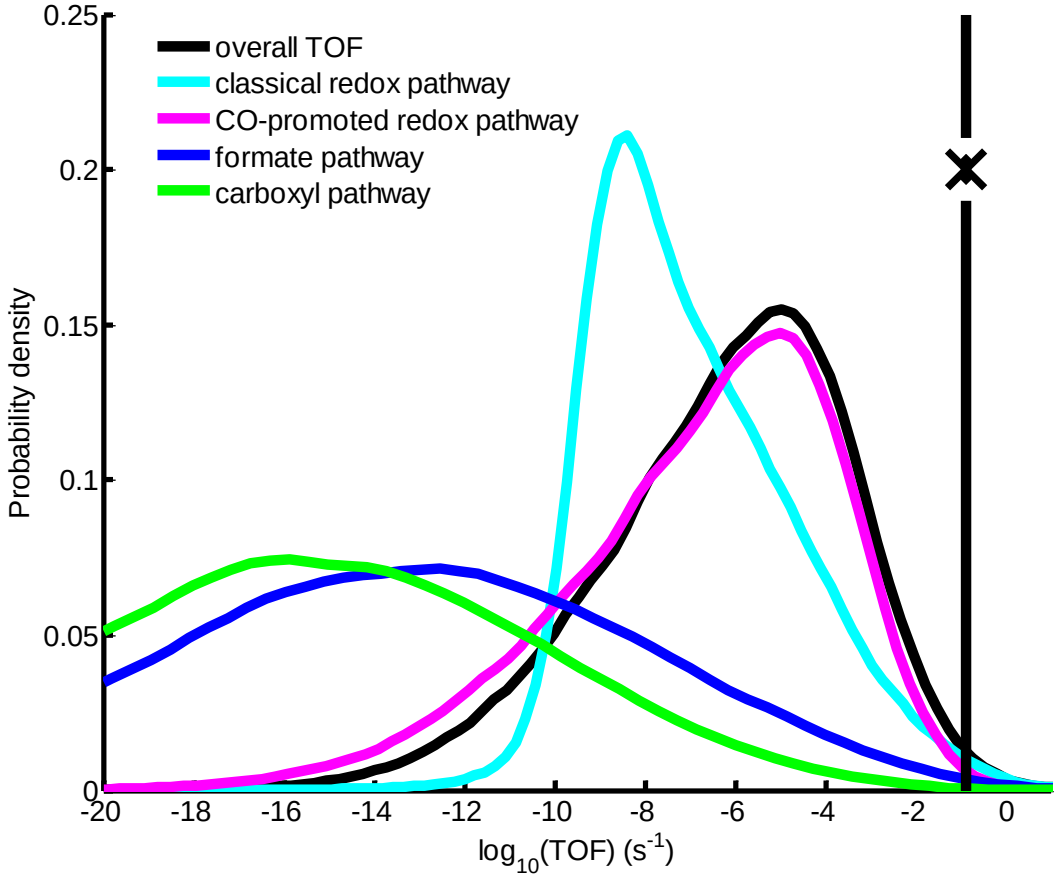

Figure 3.5 Probability density of TOFs calculated for different pathways of the WGS at Pt/TiO_2 interface sites. At least 70,000 samples are used. 470,000 samples are used to test for convergence of the 70,000 sample results. No change is observed and 70,000 sample results are plotted. P_{CO} = 0.03 atm, P_{H2O} = 0.1 atm, P_{CO2} = 0.06 atm, P_{H2} = 0.2 atm, T = 523 K. The straight line with X corresponds to the experimental results from Kalamaras, et al.[44]

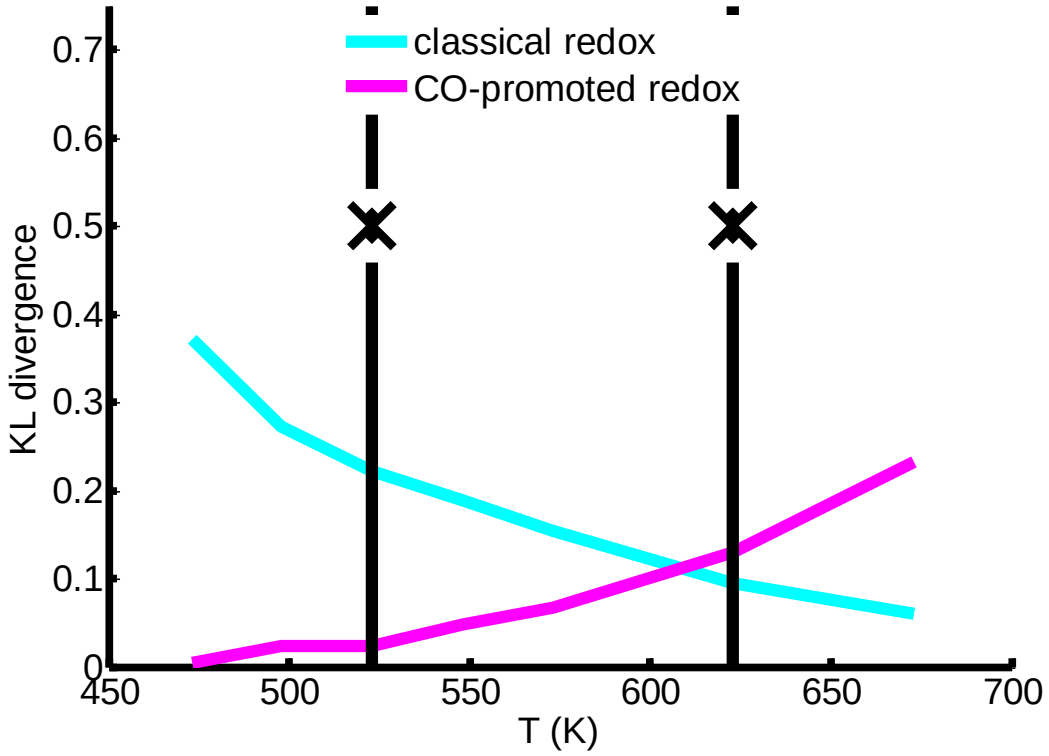

Figure 3.6 KL divergence of two catalytic cycles over a range of temperatures. A smaller KL divergence suggests dominance. $D_{KL}(P||Q) = \int_{\mathrm{x}} p(x) \log_2 \left(\frac{p(x)}{q(x)}\right)$. Two temperatures at 523 K and 623 K indicated by straight line with X are selected for discussion.

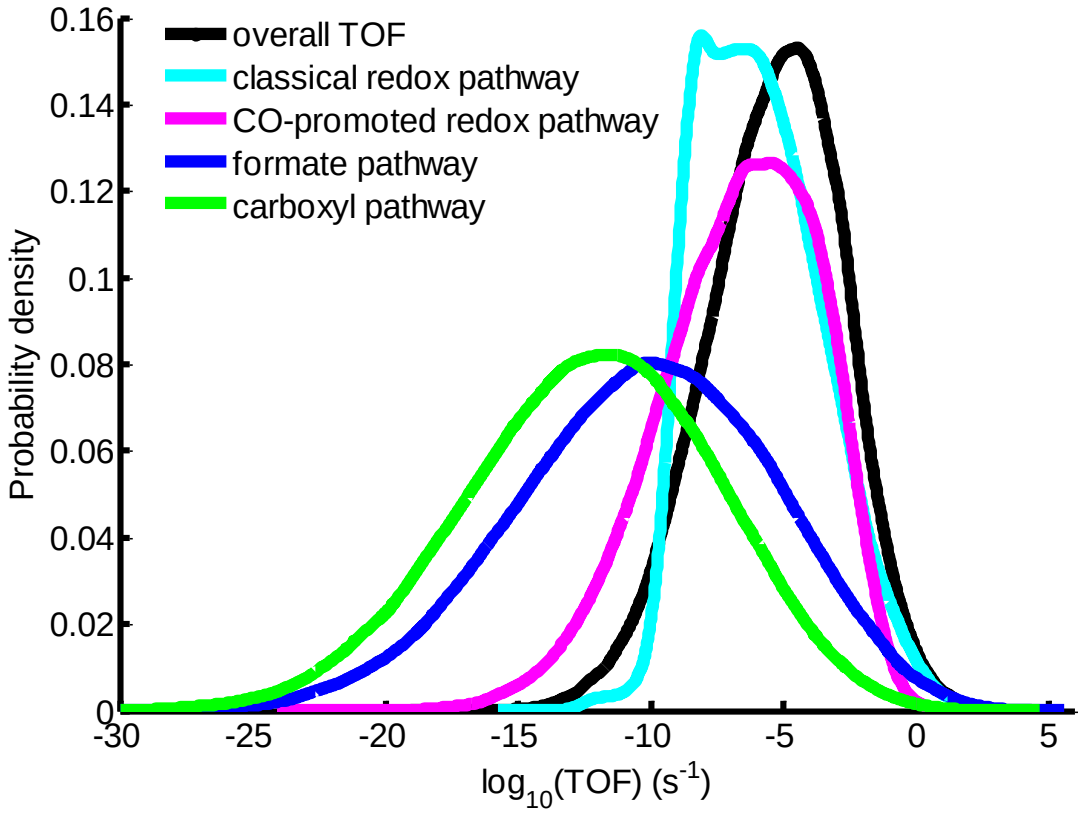

Figure 3.7 Probability density of overall TOF and individual catalytic cycle TOF of various pathways at P_{CO} = 0.03 atm, P_{H2O} = 0.1 atm, P_{CO2} = 0.06 atm, P_{H2} = 0.2 atm, and T = 623 K. The catalytic cycles have moved closer together with an increase in temperature of 100 K relative to Figure 4 as indicated by the KL divergence in Figure 5.

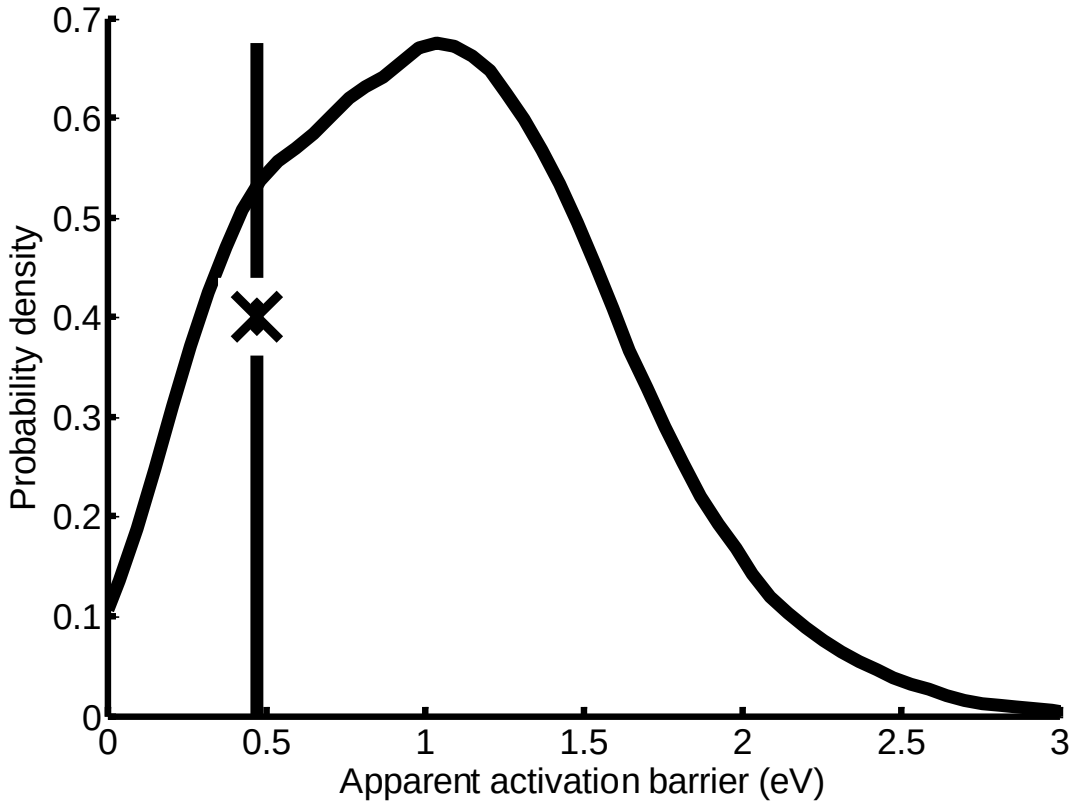

Figure 3.8 Probability density of the apparent activation barrier obtained at P_{CO} = 0.03 atm, P_{H2O} = 0.1 atm, P_{CO2} = 0.06 atm, P_{H2} = 0.2 atm, and T = 473 - 623 K. Experimental data point from Kalamaras et al.[44] is symbolized by a straight line with X.

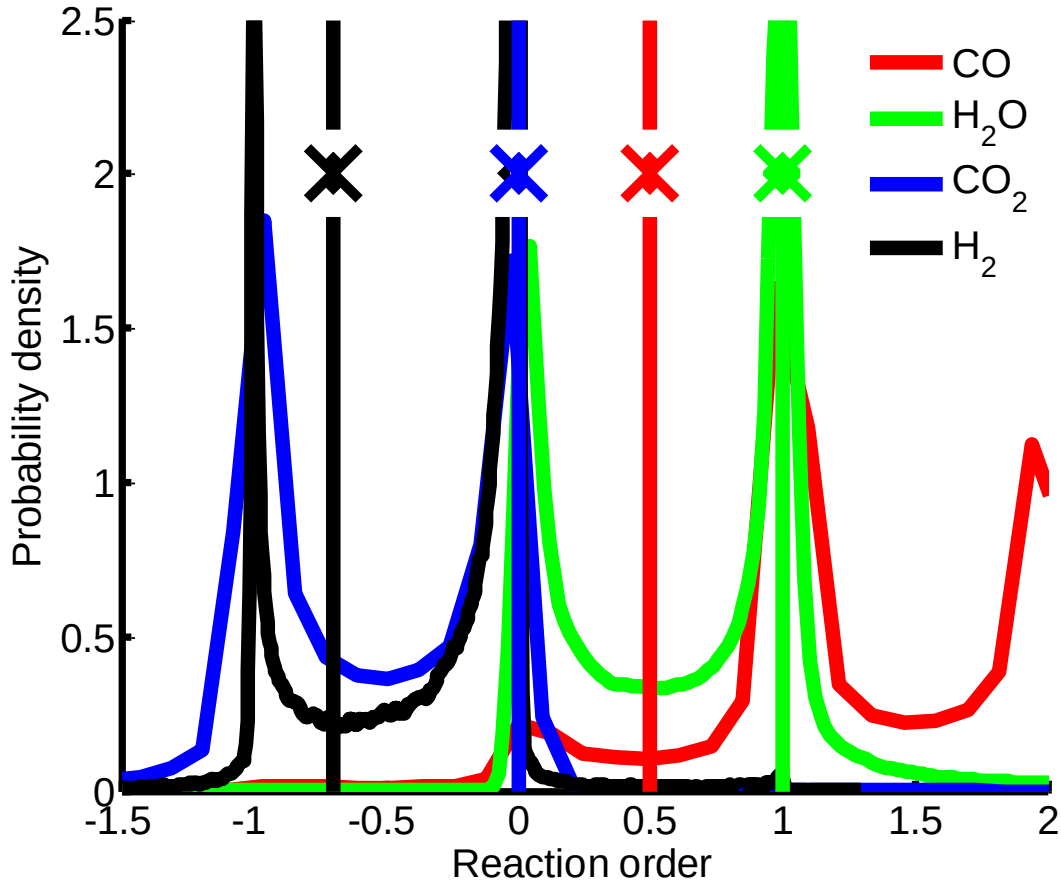

Figure 3.9 Probability density of various reaction orders. All experimental data from Kalamaras et al.[44] (symbolized by straight lines with X) are captured by their PDF's. Reaction orders have been determined at the following reaction conditions: P_{CO} = 0.03 (0.02-0.08) atm, P_{H2O} = 0.1 (0.05-0.1) atm, P_{CO2} = 0.06 (0.02-0.1) atm, P_{H2} = 0.2 (0.05-0.4) atm, and T = 523 K.

CHAPTER 4

IDENTIFYING ACTIVE SITES IN THE WATER-GAS SHIFT REACTION OVER TITANIUM OXIDE SUPPORTED PLATINUM CATALYSTS

Eric A. Walker, Salai Cheettu Ammal, Donald Mitchell, Gabriel A. Terejanu, Andreas Heyden

To be submitted.

4.1 ABSTRACT

The most active site among three is determined for the water-gas shift reaction on Pt/TiO_2 catalysts. Each active site model consists of DFT calculations and a microkinetic model. Of the three active sites, two involve the oxide support in the mechanism of reaction. Using Bayesian statistical tools and experimental data the edge active site is selected followed by the corner in close second. The edge and the corner site both explain the experimental data far better than the terrace Pt(111) active site. Therefore, it is concluded that the oxide support plays a mechanistic role in the WGS reaction. The selected active site, the edge, is verified with separate experiments at separate pressure and temperature conditions. For the selected edge active site, the uncertainty in degrees of rate control are reported and discussed. The rate-controlling step with the most uncertainty is adsorption of CO-promoter prior to the oxygen vacancy formation step.

4.2 INTRODUCTION

The WGS reaction ($CO + H_2O \rightleftharpoons CO_2 + H_2$) is the most widely applied reaction in industry for the generation of hydrogen.[1-10] Currently hydrogen is produced from natural gas sources through a process involving first high pressure steam-reforming. This produces syngas ($CO + H_2 + CO_2$) which with the addition of water (H_2O) allows for WGS.[11] At present, there is disagreement in the literature for the active site of WGS for Pt nanoparticles on a reducible support such as TiO_2. Some have suggested that the Pt is the sole active site, corresponding to terrace active sites in this work. This opinion rules out the mechanistic involvement of the support. Grabow, et al[12] and Stamatakis, et al[13,14] have proposed Pt(111)/Pt(211) as the active site, with little effect due to crystal surface

structure. Schneider, et al[15] found unphysically high surface CO coverage to be responsible to low turnover frequencies (TOF s^{-1}) during simulations. For Pt(111) and Pd(111) the reaction orders and apparent activation barrier (eV) did not match experiments where Pt and Pd nanoparticles were supported by γ-Al_2O_3. γ-Al_2O_3 support has the least supporting effect.[15] On the other hand, Grabow, et al[12] arrived at good agreement with experiments although free energies from DFT were adjusted to the data. However, Haruta, et al[16] and Stephanopoulos, et al [17] have suggested that the support plays a role in the reaction due to nearly metal-free catalysts showing activity and the activity scales with the edge length of the nanoparticles. Recently, there has been an open debate in the literature over the activity of single Pt atoms.[18,19] Stephanopoulos, et al[18] have suggested that single Pt atoms are active but Stair, et al[19] have suggested there is only indirect evidence for this. Previously, we have published on the mechanism of reaction on corner and edge sites for Pt_8 nanoparticles.[20] Selecting one of these models would not be conclusive for singe atom sites, but they would lend to the argument that single Pt atom sites are active due to the involvement of the oxide surface and the lesser importance of metal surfaces.

Four types of DFT are used for investigation in this work as previously suggested for this system in our previous work.[20] The reason to use four types of functionals is to include in the uncertainty possible approaches for treating the system. First, generalized gradient approximation functionals are used including the Perdew-Burke-Ernzerhof (PBE)[21] and Revised Perdew-Burke-Ernzerhof (RPBE)[22,23] functionals are used. Next, a hybrid functional including exact exchange-correlation was included in uncertainty quantification (UQ), the Heyd-Scuseria-Ernzerhof (HSE)[24] functional. Another type of

functional is included, the M06L functional.[25] Thermodynamics were corrected to NIST gas-phase reaction thermodynamics in an unbiased manner using a Dirichlet[26] probability density function of free energy corrections. The concept is DFT inaccurately describes the thermodynamics of WGS occurring in a cycle on the catalyst surface. However, by energy balance, the thermodynamics of the reaction on the catalyst surface must match the known NIST gas-phase thermodynamics.[27] Corrections were/are made along the intermediates and transition states based upon the molecules in the gas phase resulting in the correct overall thermodynamics for a catalytic cycle. The correction to arrive at correct thermodynamics was spread among the four molecules with the least amount of knowledge/bias to which of the gas molecules is correct or incorrect. This unbiased spread of uncertainty is/was among the four gas molecules because it is unknown including the four functionals which molecules are more or less accurate.

Bayesian statistics is widely applied in industry in academia for a gamut of conceivable applications from atmospheric and oceanographic modeling[28], computational fluid dynamics[29] including turbulent flow[30] and even chemical kinetics[31]. Caruthers, et al[32,33] have proposed the use of Bayesian statistics in chemical kinetics modeling. Bayesian statistics grew in popularity in the twentieth century due to increasing computation power necessary to solve Bayes' formula. Indeed, for complex non-linear models no analytical solution for uncertainty quantification exists or if it exists is not at all practical without a computer algorithm to calculate a numerical approximation to the exact solution of Bayes' formula. In Bayes' century there was no such computing power. The Bayesian inverse will allow for not only selecting a model but also identifying dominant cycles after learning from experimental data. In the following sections, first

Pt(111) is calculated. The four functional data for Pt(111) and the corner active sites are in tables in the supporting information. Next is a discussion of the Bayesian inverse problem methodology. The results of the model selection are presented and discussed. A discussion and listing of the rate controlling steps is included in the supporting information. The Campbell's degree of rate control[34-38] is used and the findings are probabilistic in nature like other Bayesian posterior probabilities. Previously, degrees of rate control have been reported as single numbers. Although, a slight change in free energetics of the rate controlling step such as can be caused by a temperature shift changes the rate-controlling step.[39] Now, with the inclusion of uncertainty, more information is provided in the sense that a range of possible degrees of rate control are revealed and non-rate-controlling steps may be confidently ruled out because they have no probability to be rate controlling. Also, insight is provided about the summation to one principle of degrees of rate control and the conditions for negative degree of rate control.[40] The findings are summarized in the conclusion. In future work, the Pt/CeO_2 Bayesian inverse problem is suggested.

4.3 RESULTS AND DISCUSSION

We can see from Figure 4.1a that the mean of the four functionals is slightly higher than the PBE value for the classical redox pathway. From Figure 4.1b we see that the mean begins at a higher relative free energy but otherwise does not change the relative free energy to be remarkably higher. We see from Figure 4.1a that the reaction thermodynamics are exact- they come to a point at the end of the classical redox pathway. The CO-promoted redox pathway does not begin at S1 and so has uncertainty to begin with. Also, the first uncertainty shown is for a transition state. The highest free energy

transition state for both the mean of the four functionals and PBE is vacancy formation and CO_2 desorption in the classical redox pathway. The second highest transition state for the classical redox pathway is TS7 which involves O-H bond breaking. The highest free energy transition state within the CO-promoted redox pathway is oxygen vacancy formation. However, the free energy of this transition state is less than for the oxygen vacancy transition state of the classical redox pathway.

In Figure 4.2a the TOF (s^{-1}) of the edge posterior captures the experiment.[41] In Figure 4.2b the apparent activation barrier (eV) has reduced in uncertainty from the prior while capturing the experiment. The same holds true for Figure 4.3a-b of the reaction orders. The Figures 4.4a-b-4.5a-b are a verification of the edge posterior at separate[42] experimental conditions providing further support as the edge to be the active site of WGS on Pt/TiO_2. Figure A.6 is the degree of rate control for the classical pathway and CO-promoted pathway.

Table 4.1 shows that the evidence against the corner site being active is barely worth a mention according to Table A.7, Jeffreys scale.[43] This result suggests the corner is contributing to reaction and is active. However, the terrace sites are not active at all as indicated by the substantial evidence against it being selected. A key conclusion may be drawn here too because the terrace site is the only site which does not include the support in the mechanism. That is, the corner and edge active sites involve forming oxygen vacancies and borrowing that oxygen that the support doesn't possess solely electronic contributions to reaction but that is mechanistically involved in a way that other non-oxygen donating supports would be able to provide.

Figure A.3 seems to suggest that the lateral interactions increase the free energy path and certainly the free energy of the highest free energy transition state. However, a key point is the depth of the state of CO adsorption- it is less deep with lateral interactions which causes surface coverage fraction effects. With no lateral interaction effects the surface is highly covered with CO which inhibits the TOF. The lateral interactions also change the highest free energy transition state, although they both involve O-H bond breaking. With no lateral interaction this highest free energy transition state is $COOH \leftrightarrow CO_2 + H$. With lateral interactions the highest free energy transition state is $H_2O \leftrightarrow OH + H$. This transition state corresponds to the only rate controlling step with 1.00 degree of rate control. We are not suggesting this correspondence is by necessity but happens to agree in this case. Another confirmation of the lateral interactions comes from Figure A.3. The overall reaction thermodynamics is the same with and without lateral interactions. Were the lateral interactions to be implemented in a different way that did not include a correction for every intermediate and transition state such as is done the overall reaction thermodynamics would change. Figure A.3 is created from taking the steady-state reaction energies and activation barriers from the microkinetic model and constructing a free energy path. During the microkinetic model, the reaction energies are affecting the surface coverage fractions of all states which in turn (the CO and H coverages), affect the reaction energies and activation barriers. Therefore matching the reaction thermodynamics is evidence that the lateral interactions are not affecting the reaction thermodynamics and are operating correctly. Figure A.7 shows the carboxyl intermediate as key. Other potential pathways are shown but not all possibilities which are numerous are illustrated. The hydroxyl (HCOO) intermediate is

not dominant as indicated by Figure A.7. These results are suggested without uncertainty too. (Figures A.7-A.10 are the terrace active site with posterior uncertainty).

From Figure A.11 for the corner we observe a large reduction in uncertainty in the uncertain through Bayesian calibration. The redox pathway is dominant on the corner. We see from Figure A.11 that the redox pathway TOF is much higher than the associated carboxyl even much more than the carboxyl is higher than the redox pathway. Figures A.11-A.14 are the posterior uncertainties plotted on the experimental data used for calibration. The vertical bars represent the experiments. The uncertainty in the figures correspond to the red posterior uncertainty in the free energy path of Figure 4.2. The highest energy transition state is between intermediate (IM) 12 and IM13 which corresponds to the vacancy formation reaction $(CO, CO_2)_{Pt-O_i}\ (IM12) \rightarrow CO_{Pt} - V_i(IM13) + CO_2(g)$.[29] Furthermore, the redox pathway is able to capture the experimental TOF. Figures A.12-A.13 display the reaction orders with DFT uncertainty. The DFT with uncertainty after calibration in Figure A.12 is not able to capture all reaction orders. Certain reaction orders which are CO and CO_2 increase the likelihood in Bayes' formula but the other reaction orders cannot be captured and indeed result in smaller evidence. When model error is considered which lumps together transition state theory, numerical accuracy of the microkinetic model, and any experimental error (because information is not available on the experimental uncertainty) the reaction orders are captured as shown in Figure A.13. The CO and CO_2 have a small model error but H_2O in particular contains a large model error. These model errors would suggest the edge active site is more active contributing to the experimental reaction orders. The apparent activation barrier in Figure A.14.

For the terrace site uncertainty displayed in Figure A.5 the uncertainty is widened but the log-likelihood is still above the limit of 100 instead of dropping to numbers comparable to the edge and corner <10. The mean of the four functionals changes the highest free energy transition state from water dissociation to carboxyl formation $CO^* + OH^* \leftrightarrow COOH^* + ^*$. Figures A.7-A.10 show considerable uncertainty in the apparent activation barrier (eV) and an inability to capture reaction orders which are further visual evidence for the oxide-supported active sites being active for WGS. The overall large uncertainties are due to the search for a higher-evidence region of the parameter space which is not obtained but instead the limit of log-likelihood of 100 is constant.

Figure 4.2a-b is the posterior uncertainty in overall TOF and individual cycles plotted on the TOF experimental point used for calibration as well as the same for the apparent activation barrier. The experiment is more within the pdf than the prior uncertainty.[20] A model error is added for the overall TOF which is not available for individual cycles. As in the prior uncertainty, the posterior uncertainty shows the CO-promoted redox to be dominant to classical redox. This would agree with the free energy pathway being lower for the CO-promoted pathway. In Figure 4.3a-b the model error for reaction orders is visibly less than the model error for the reaction orders of the terrace and corner sites. Also, each reaction order is captured by the DFT uncertainty. This supports the edge site being most active for WGS.

Figure A.6 shows 5-6 potentially rate controlling steps with posterior uncertainty. Since the probability of any one step possessing a degree of rate control of one is very small, most likely there are multiple rate-controlling steps. The classical redox pathway

has steps with less degree of rate control which is to be expected due to that pathway not being dominant. TS3 is for the vacancy formation step of the classical redox cycle $CO_{2(Pt\text{-}int)} + CO(g) + H_2O(g) \rightarrow *_{Pt}\text{-}V_{int} + CO_2(g) + CO(g) + H_2O(g)$. This step, which has the highest probability of any step in the classical redox pathway, has also the highest free energy transition state for the classical redox pathway. TS4 is for the reaction $*_{Pt}\text{-}V_{int} + CO(g) + H_2O(g) + CO_2(g) \rightarrow *_{Pt}\text{-}2OH_{int} + CO(g) + CO_2(g)$. TS6 is for the reaction $H_{Pt}\text{-}OH_{int} + *_{Pt} + CO(g) + CO_2(g) \rightarrow 2H_{Pt}\text{-}O_{int} + CO(g) + CO_2(g)$.[4,21]

TS8 begins the branching off of the CO-promoted redox cycle and shows a non-zero probability of being rate-controlling. TS10 corresponds to reaction $CO_{Pt}\text{-}V_{int} + O_{int} H_2O(g) + CO_2(g) \rightarrow CO_{Pt}\text{-}2OH_{int} + CO_2(g)$. Interestingly although the transition state has the highest free energy for the CO-promoted redox pathway the rate control is not the largest by probability. TS11 corresponds to reaction $CO_{Pt}\text{-}2OH_{int} + O_s + CO_2(g) \rightarrow CO_{Pt}\text{-}OH_{int}\text{-}O_{int}\text{-}OH_s + CO_2(g)$. This reaction possesses a high probability of being the most rate-controlling step. It possesses a particularly large forward activation barrier due to stable reactants. TS12 which also is most likely rate-controlling is the reaction $CO_{Pt}\text{-}OH_{int}\text{-}O_{int}\text{-}OH_s + O_{int} + CO_2 (g) \rightarrow CO_{Pt}\text{-}OH_{int}\text{-}O_{int}\text{-}OH_{int} + O_s + CO_2 (g)$. The sum of the degrees of rate control are shown. Since the simulation of uncertainty is completed numerically each samples gives one sum of degrees of rate control which is always one. However, how the rate control is distributed can vary for each sample which is why uncertainty is available in the plots. A sum to one is a check that the degree of rate control analysis has been correctly implemented.

4.4 CONCLUSIONS

Three active sites are investigated and the most active site selected. An edge, corner and terrace site are considered. Four functionals are used to evaluate the prior uncertainty for each site. The terrace site includes lateral interactions for the most abundant surface intermediates CO and H and their effect on all states and transition states. Then, using a microkinetic model and experimental kinetic data of TOF, reaction orders and apparent activation barrier, a Bayesian calibration is conducted for each active site model. The posterior uncertainty is less for the edge and corner site and the posterior uncertainty is more for the terrace site. For the edge site, the CO-promoted redox is dominant to classical redox. For the corner site, the redox pathway is dominant to the associated carboxyl pathway. For the terrace site the pathway involving the COOH carboxyl intermediate is dominant to the pathway involving the HCOO formate intermediate. An evidence number is obtained for each active site during Bayesian calibration. This number is a quantification of which active site model best explains experiments. The edge site model is slightly more active than the corner site. The terrace site does not explain experiments and is therefore not active. The edge and corner sites are both at the three phase boundary of the Pt nanoparticle and the TiO_2 support in which the support plays a mechanistic role by donating an oxygen. The degrees of rate control for the active site has been revealed with a quantification of uncertainty and many steps contribute to rate control. Finally, the edge posterior uncertainty has been verified with data performed at different experimental conditions than the data used for Bayesian calibrations. We believe that beyond solving what is the active site for water-gas shift by

Pt/TiO_2 catalyst, the methods presented in this work are transferrable to other catalysis challenges where determination of the active site is important.

4.5 ACKNOWLEDGEMENTS

The authors would like to acknowledge the National Science Foundation (NSF) CAREER award grant #'s NSF CBET-1254352 and CBET-0932991, NSF grant Designing Materials to Revolutionize and Engineer our Future, the NSF Research Experience for Undergraduates (REU) program # NSF EEC-1358931 supporting REU student Donald Mitchell, and the 2014 Eastman fellowship. The US Department of Energy facilities located at the National Energy Research Scientific Computing Center (NERSC) and at EMSL, located at Pacific Northwest National Laboratory are gratefully acknowledged for their computing resources used in this work.

4.6 REFERENCES

[1] Ammal, S. C.; A. Heyden, Origin of the Unique Activity of Pt/TiO2 Catalysts for the Water Gas Shift Reaction. *J. Catal*. **2013**, *306*, 78-90.

[2] Oettel, C.; Rihko-Struckmann, L.; Sundmacher, K.; Characterisation of the Electrochemical Water Gas Shift Reactor (EWGSR) Operated with Hydrogen and Carbon Monoxide Rich Feed Gas. *Int. J. Hydrogen Energy* **2012**, *37*, 11759-11771.

[3] Haryanto, A.; Fernando, S.; Murali, N.; Adhikari, S. Current Status of Hydrogen Production Techniques by Steam Reforming of Ethanol: A Review. *Energy Fuels* **2005**, *19*, 2098-2106.

[4] Holladay, J. D.; Hu, J.; King, D. L.; Wang, Y. An Overview of Hydrogen Production Technologies. *Catal. Today* **2009**, *139*, 244-260.

[5] Cortright, R. D.; Davda, R. R.; Dumesic, J. A. Hydrogen from Catalytic Reforming of Biomass-Derived Hydrocarbons in Liquid Water. *Nature* **2002**, *418*, 964-967.

[6] Song, C. S. Fuel Processing for Low-Temperature and High-Temperature Fuel Cells: Challenges, and Opportunities for Sustainable Development in the 21st Century. *Catal. Today* **2002**, *77*, 17-49.

[7] Trimm, D. L. Minimisation of Carbon Monoxide in a Hydrogen Stream for Fuel Cell Application. *Appl.Catal. A*. **2005**, *296*, 1-11.

[8] Bartholomew, C. H.; Farrauto, R. J. *Fundamentals of Industrial Catalytic Processes*; Wiley: Hoboken, N.J. 2006.

[9] Liu, Y.; Fu, Q.; Flytzani-Stephanopoulos, M. Preferential Oxidation of CO in H2 over CuO-CeO_2 Catalysts. *Catal. Today* **2004**, *93-95***,** 241-246.

[10] Suh, D. J.; Kwak, C.; Kim, J. H.; Kwon, S. M.; Park, T. J.; Removal of Carbon Monoxide from Hydrogen-Rich Fuels by Selective Low-Temperature Oxidation Over Base Metal Added Platinum Catalysts. *J. Power Sources* **2005**, *142*, 70-74.

[11] Chorkendorff, I.; Niemantsverdriet, J. W. Concepts of Modern Catalysis and Kinetics. John Wiley and Sons: Verlag, **2007**.

[12] Grabow, L. C.; Gokhale, A. A.; Evans, S. T.; Dumesic, J. A.; Mavrikakis, M. *J. Phys. Chem. C.* Mechanism of the Water Gas Shift Reaction on Pt: First Principles, Experiments, And Microkinetic Modeling. **2008**, *112*, 4608-4617.

[13] Stamatakis, M.; Chen, Y.; Vlachos, D. G. First-Principles-Based Kinetic Monte Carlo Simulation of the Structure Sensitivity of the Water-Gas Shift Reaction on Platinum Surfaces. *J. Phys. Chem. C* **2011**, 115, 24750-24762.

[14] Stamatakis, M.; Vlachos, D. G. A Graph-Theoretical Kinetic Monte Carlo Framework for on-Lattice Chemical Kinetics. *J Chem. Phys.* **2011**, 115, 214115.

[15] Clay, J. P.; Greely, J. P.; Ribeiro, F. H.; Delgass, W. N.; Schneider, W. F. DFT Comparison of Intrinsic WGS Kinetics over Pd and Pt. *J. Catal.* **2014**, 320, 106-117.

[16] Ishida, T.; Kinoshita, N.; Okatsu, H.; Akita, T.; Takei, T.; Haruta, M. Influence of the Support and the Size of Gold Clusters on Catalytic Activity for Glucose Oxidation. *Angew. Chem. Int. Ed.* **2008**, *47*, 9265-9268.

[17] Fu, Q.; Saltsburg, H.; Flytzani-Stephanopoulos, M. Active Nonmetallic Au and Pt Species On Ceria-Based Water-Gas Shift Catalysts. *Science* **2003**, *301*, 935-938.

[18] Yang, M.; Liu, J.; Lee, S.; Zugic, B.; Huang, J.; Allard, L. F.; Flytzani-Stephanopoulos, M. A Common Single-Site Pt(II)-O(OH)$_x$- Species Stabilized by Sodium on "Active" and "Inert" Supports Catalyzes the Water-Gas Shift Reaction. *J. Am. Chem. Soc.* **2015**, *137*, 3470-3473.

[19] Ding, K.; Gulec, A.; Johnson, A. M.; Schweitzer, N. M.; Stucky, G. D.; Marks, L. D.; Stair, P. C. Identification of Active Sites in CO Oxidation and Water-Gas Shift over Supported Pt Catalysts. *Science* **2015**, *350*, 6257.

[20] Walker, E.; Ammal, S. C.; Terejanu, G. A.; Heyden, A. Uncertainty Quantification Framework Applied to the Water-Gas Shift Reaction over Pt-based Catalysts. *J. Phys.Chem. C*, **2016**, *120*, 10328–10339.

[21] Perdew, J. P.; Burke, K.; Ernzerhof, M. Generalized Gradient Approximation Made Simple. *Phys. Rev. Lett.* **1996**, *77*, 3865-3868.

[22] Hammer, B.; Hansen, L. B.; Norskov, J. K. Improved Adsorption Energetics within Density-Functional Theory Using Revised Perdew-Burke-Ernzerhof Functionals. *Phys. Rev. B.* **1999**, *59*, 7413-7421.

[23] Zhang, Y.; Yang, W. Comment on "Generalized Gradient Approximation Made Simple". *Phys. Rev. Lett.* **1998**, *80*, 890.

[24] Heyd, J.; Scuseria, G. E.; Ernzerhof, M. Hybrid Functionals Based on a Screened Coulomb Potential. *J. Chem. Phys.* **2003**, *118*, 8207.

[25] Zhao, Y.; Truhlar, D. G. A New Local Density Functional for Main-Group Thermochemistry, Transition Metal Bonding, Thermochemical Kinetics, and Noncovalent Interactions. *J. Chem. Phys.* **2006**, *125*, 194101.

[26] Plessis, S.; Carrasco, N.; Pernot, P. Knowledge-Based Probabilistic Representations

of Branching Ratios in Chemical Networks: The Case of Dissociative Recombinations. *J.Chem. Phys.* **2010**, 133, 134110.

[27] Afeefy, H.; Liebman, J.; Stein, S. NIST Chemistry WebBook, NIST Standard Reference Database Number 69. (National Institute of Standards and Technology, Gaithersburg MD, USA 2010).

[28] Wikle, C. K.; Berliner, L. M.; Cressie, N. Hierarchical Bayesian Space-Time Models. *Environ. Ecol. Stat.* **1998**, 5, 117-154.

[29] Najm, H. N.; Debusschere, B. J.; Marzouk, Y. M.; Widmer, S.; LeMaitre, O. Uncertainty Quantification in Chemical Systems. *Int. J. Num. Meth. Eng*. **2009**, 80, 789-814.

[30] S. H. Cheung, T. A. Oliver, E. E. Prudencio, S. Prudhomme, R. D. Moser. Bayesian Uncertainty Analysis with Applications to Turbulence Modeling. *Rel. Eng. Syst. Saf.* **2011**, 96, 1137-1149.

[31] N. Galagali, Y. M. Marzouk. Bayesian Inference of Chemical Kinetic Models from Proposed Reactions. *Chemical Engineering Science*. **2015**, 123, 170-190.

[32] S. H. Hsu, S. D. Stamatis, J. M. Caruthers, W. N. Delgass, V. Venkatasubramanian, G. E. Blau, M. Lasinski, S. Orcun. Bayesian Framework for Building Kinetic Models of Catalytic Systems. *Ind. Chem. Eng. Res.* **2009**, 48, 4768-4790.

[33] G. Blau, M. Lasinski, S. Orcun, S. H. Hsu, J. Caruthers, N. Delgass, V. Venkatasubramanian. High Fidelity Mathematical Model Building with Experimental Data: A Bayesian Approach. *Comput. Chem. Eng.* **2008**, 32, 971-989.

[34] Kozuch, S.; Shaik, S. A Combined Kinetic-Quantum Mechanical Model for Assessment of Catalytic Cycles: Application to Cross Coupling and Heck Reactions. *J. Am. Chem. Soc.* **2006**, *128*, 3355-3365.

[35] Kozuch, S.; Shaik, S. Kinetic-Quantum Chemical Model for Catalytic Cycles: The Haber Bosch Process and the Effect of Reagent Concentration. *J. Phys. Chem. A* **2008**, *112*, 6032-6041.

[36] Campbell, C. T. Micro- and Macro-Kinetics: Their Relationship in Heterogeneous Catalysis. *Top. Catal.* **1994**, *1*, 353−366.

[37] Campbell, C. T. Finding the Rate-Determining Step in a Mechanism - Comparing Dedonder Relations with the "Degree of Rate Control". *J. Catal.* **2001**, *204*, 520-524.

[38] Stegelmann, C.; Andreasen, A.; Campbell, C. T. Degree of Rate Control: How Much the Energies of Intermediates and Transition States Control Rates. *J. Am.*

Chem. Soc. **2009**, *131*, 8077−8082.

[39] Van den Bossche, M.; Grönbeck, H.; Methane Oxidation over PdO(101) Revealed by First-Principles Kinetic Modeling. *J. Am. Chem. Soc.* **2015**, *137*, 12035-12044.

[40] Stegelmann, C.; Schiodt, N. C.; Campbell, C. T.; Stoltze, P. Microkinetic Modeling of Ethylene Oxidation over Silver. *J. Catal.* **2004**, *221*, 630-649.

[41] Kalamaras, C. M.; Panagiotopoulou, P.; Kondarides, D. I.; Efstathiou, A. M.; Kinetic and Mechanistic Studies of the Water–Gas Shift Reaction on Pt/TiO_2 catalyst. *J. Catal*. **2009**, *264*, 117-129.

[42] Thinon, O.; Rachedi, K.; Diehl, F.; Avenier, P.; Schuurman, Y. Kinetics and Mechanism of the Water-Gas Shift Reaction Over Platinum Supported Catalysts. *Top. Catal.* **2009**, *52*, 1940-1945.

[43] Jeffreys, H. The Theory of Probability. Oxford University Press: **1961**.

4.7 TABLES AND FIGURES

Table 4.1 Bayes factor matrix.

B_{12} where 1 is rows and 2 is columns	Edge	Corner	Terrace
Edge	1.00	2.20	5.05e+38
Corner	0.45	1.00	1.1105e+38
Terrace	1.9801e-39	9.0046e-39	1.00

(a)

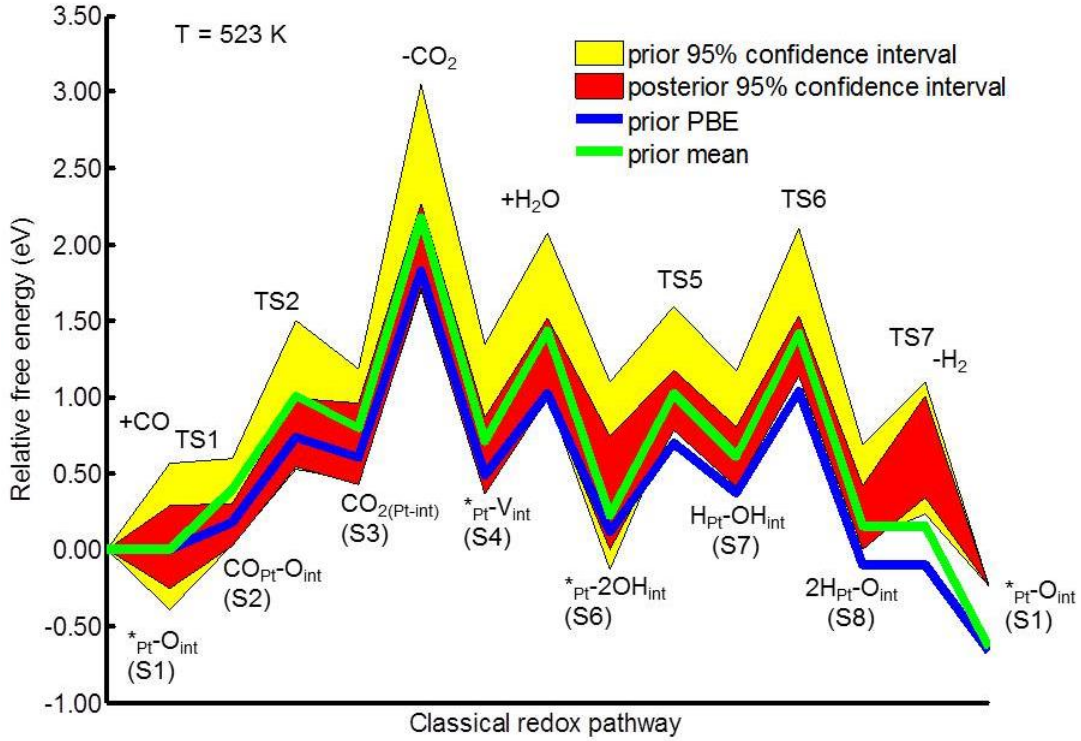
T = 523 K
prior 95% confidence interval
posterior 95% confidence interval
prior PBE
prior mean
Relative free energy (eV)
3.50
3.00
2.50
2.00
1.50
1.00
0.50
0.00
-0.50
-1.00
+CO
TS1
TS2
-CO2
+H2O
TS5
TS6
TS7
-H2
*Pt-Oint (S1)
COPt-Oint (S2)
CO2(Pt-int) (S3)
*Pt-Vint (S4)
*Pt-2OHint (S6)
HPt-OHint (S7)
2HPt-Oint (S8)
*Pt-Oint (S1)
Classical redox pathway

(b)

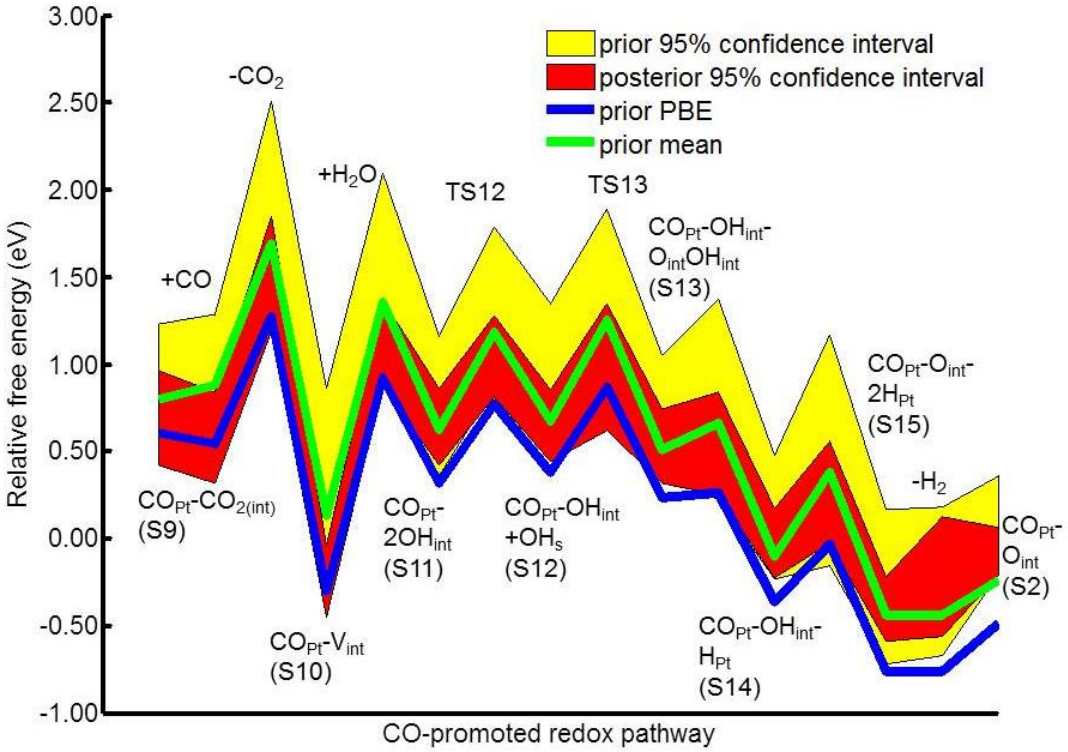

Figure 4.1 Prior and posterior uncertainty in the two dominant free energy paths for the edge active site.

(a)

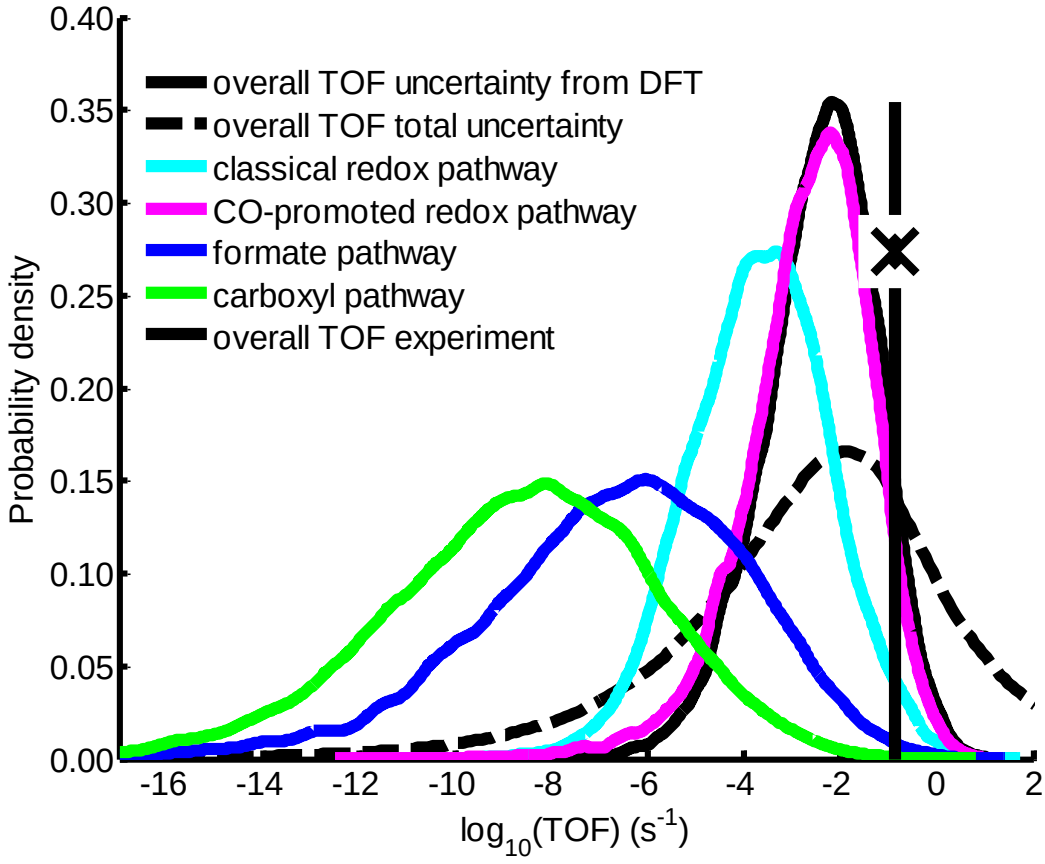
0.40
0.35
0.30
0.25
0.20
0.15
0.10
0.05
0.00
Probability density
overall TOF uncertainty from DFT
overall TOF total uncertainty
classical redox pathway
CO-promoted redox pathway
formate pathway
carboxyl pathway
overall TOF experiment
-16
-14
-12
-10
-8
-6
-4
-2
0
2
log10(TOF) (s-1)

(b)

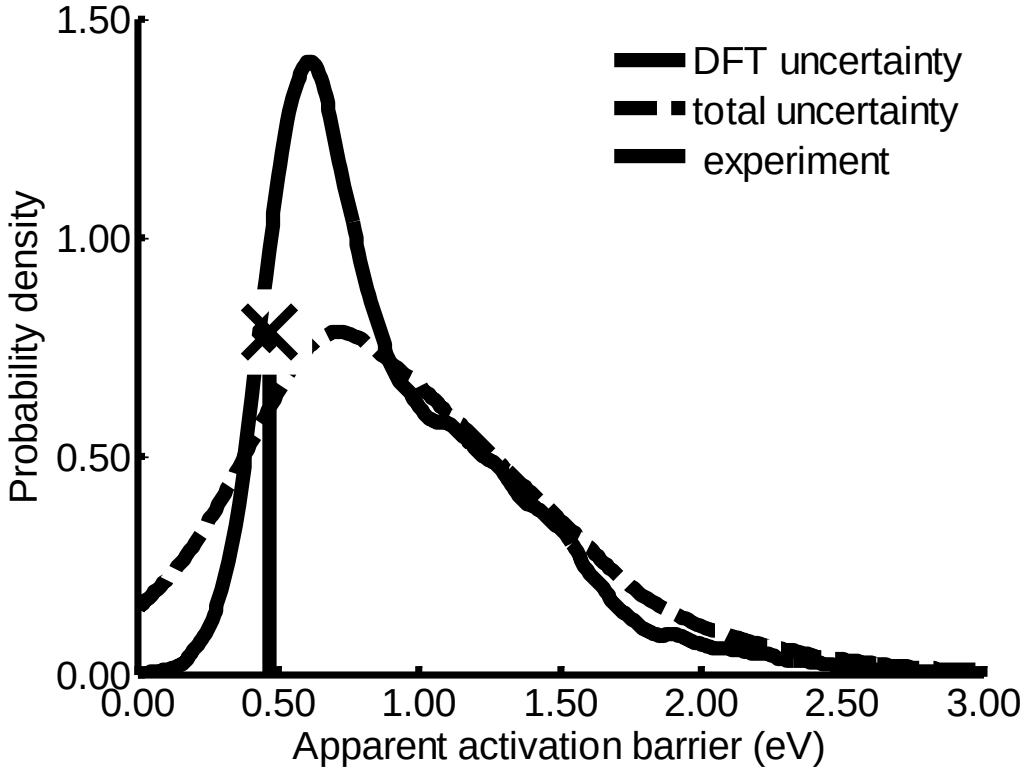

Figure 4.2 (a) TOF (s^{-1}) of the edge posterior captures the experiment.[41] (b) Apparent activation energy (eV) results of the Bayesian inverse.

(a)

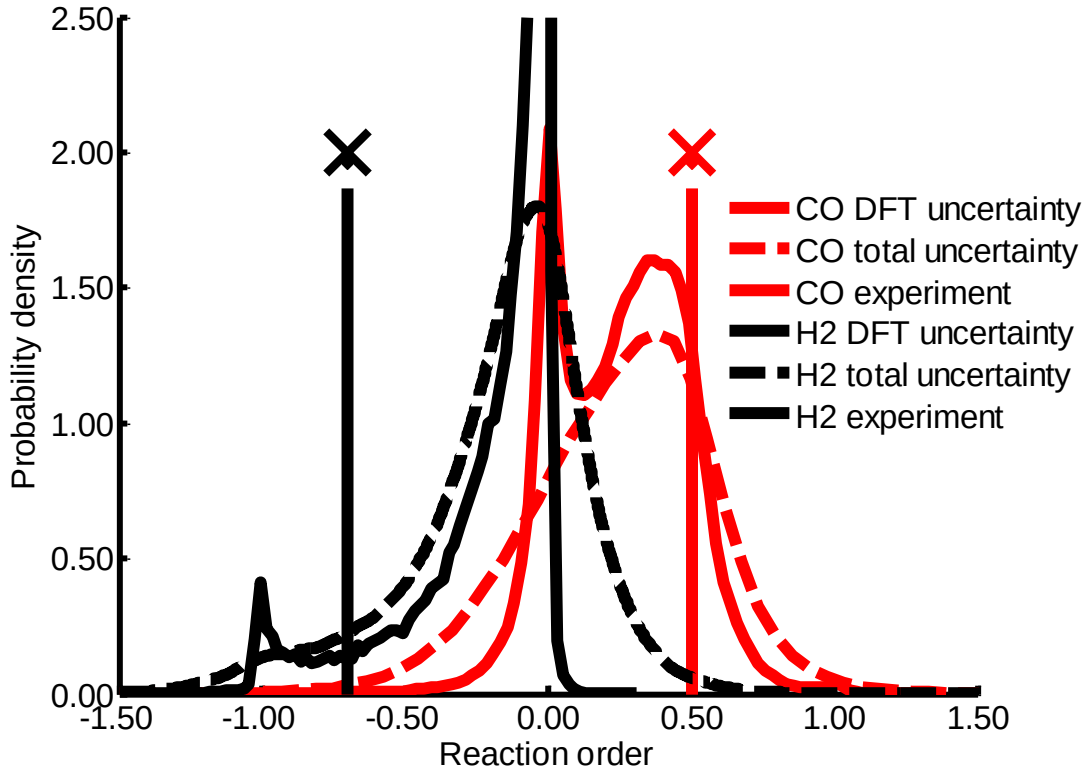
2.50
2.00
1.50
1.00
0.50
0.00
Probability density
-1.50
-1.00
-0.50
0.00
0.50
1.00
1.50
Reaction order
CO DFT uncertainty
CO total uncertainty
CO experiment
H2 DFT uncertainty
H2 total uncertainty
H2 experiment

(b)

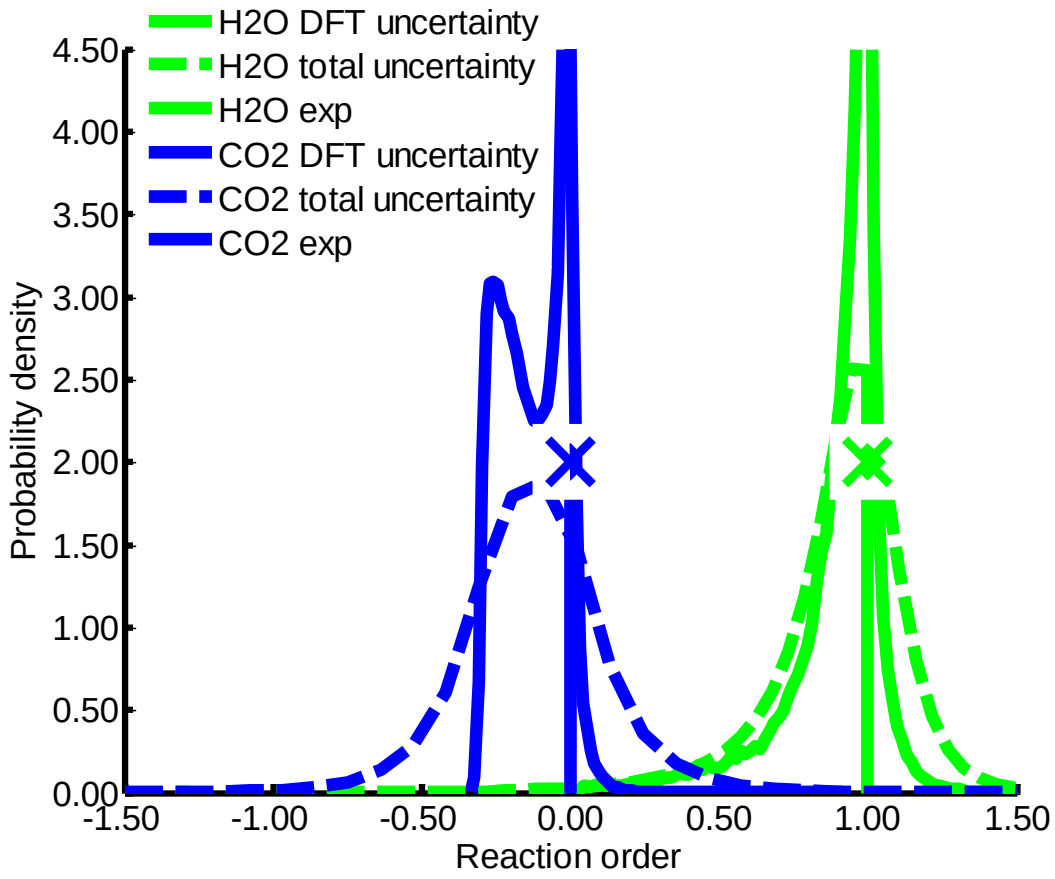

Figure 4.3 Reaction orders after the Bayesian inverse. The uncertainty due to DFT is able to capture experiments.

(a)

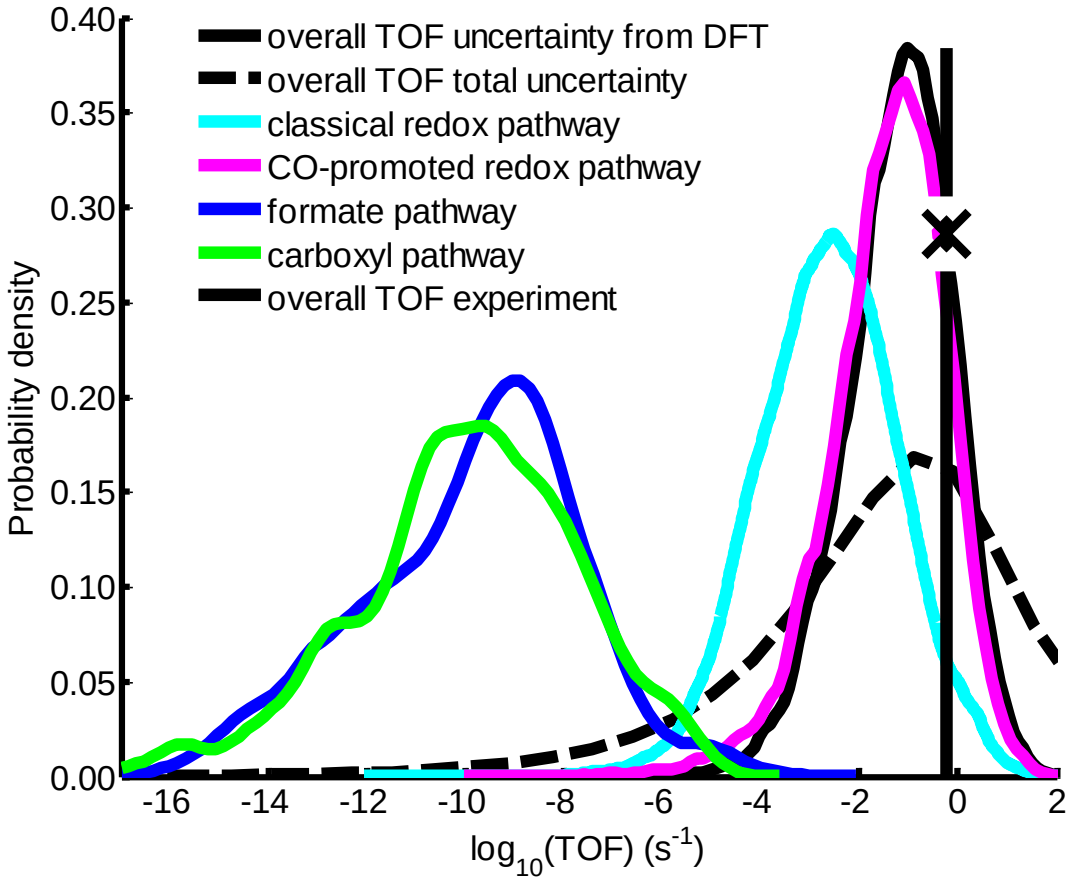
overall TOF uncertainty from DFT
overall TOF total uncertainty
classical redox pathway
CO-promoted redox pathway
formate pathway
carboxyl pathway
overall TOF experiment
Probability density
0.40
0.35
0.30
0.25
0.20
0.15
0.10
0.05
0.00
-16
-14
-12
-10
-8
-6
-4
-2
0
2
log10(TOF) (s-1)

(b)

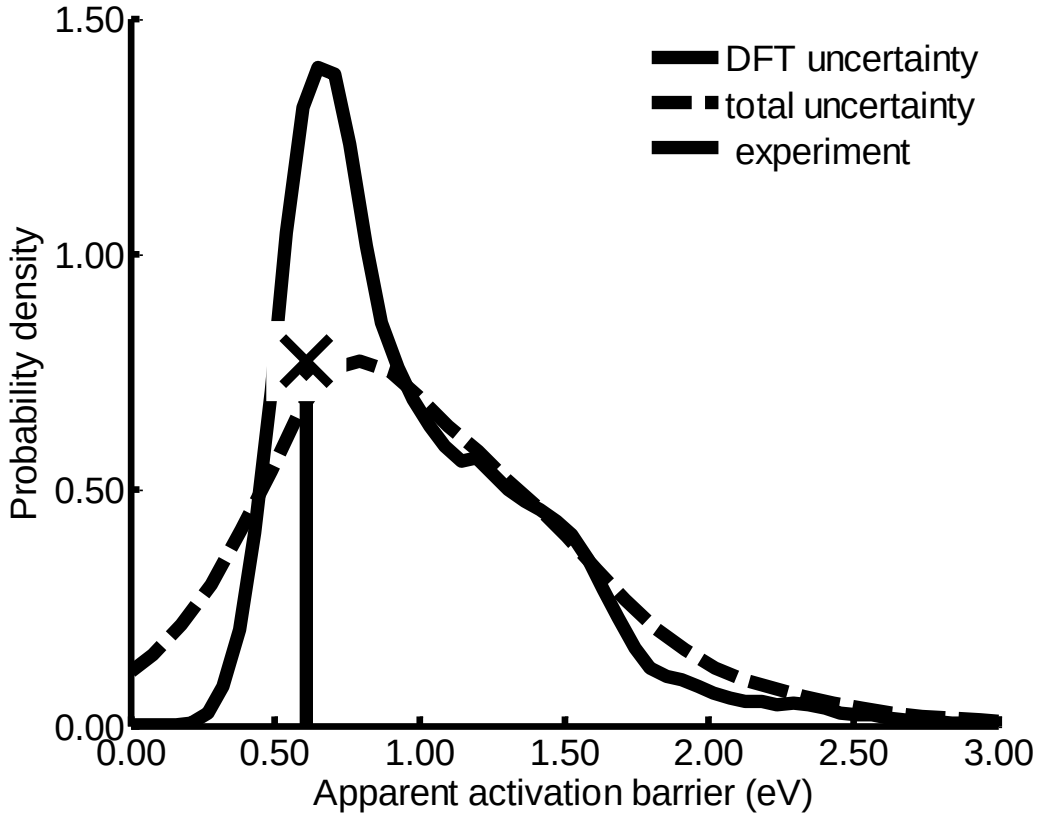

Figure 4.4 (a) Edge verification at separate experimental conditions and sources TOF (s^{-1}). T = 573 (K), P_{CO} = 0.1 (atm), P_{H2O} = 0.2, P_{CO2} = 0.1, P_{H2} = 0.4.[42] (b) Edge verification at separate experimental conditions apparent activation barrier (eV).
(a)

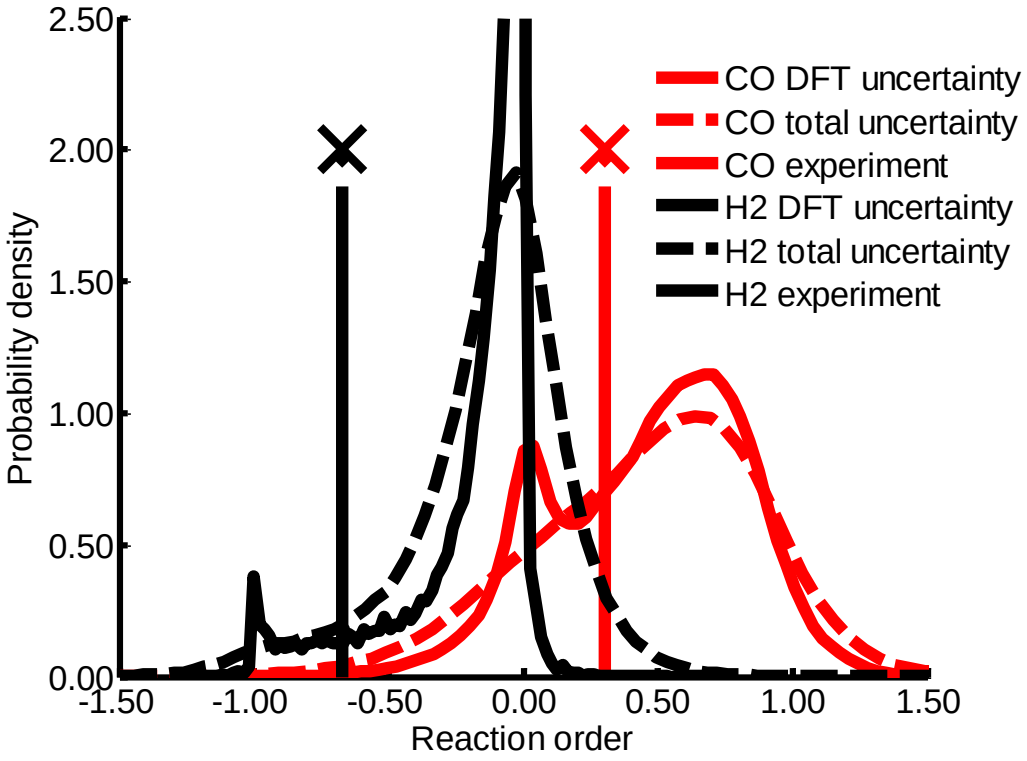
2.50
2.00
1.50
1.00
0.50
0.00
Probability density
-1.50
-1.00
-0.50
0.00
0.50
1.00
1.50
Reaction order
CO DFT uncertainty
CO total uncertainty
CO experiment
H2 DFT uncertainty
H2 total uncertainty
H2 experiment

(b)

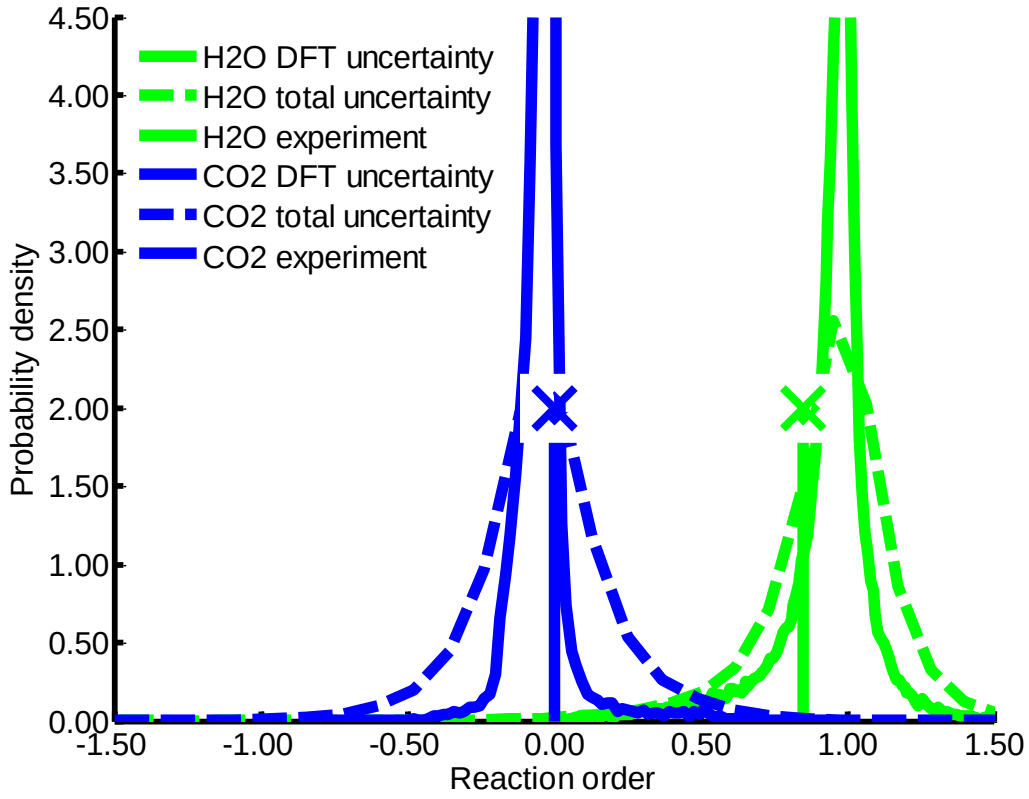

Figure 4.5 Edge verification at separate experimental conditions reaction orders. T = 573 (K), P_{CO} = 0.1 (atm), P_{H2O} = 0.2, P_{CO2} = 0.1, P_{H2} = 0.4.[42]

APPENDIX A – SUPPORTING INFORMATION FOR CHAPTER 4

A.1 TERRACE ACTIVE SITE MODEL

All DFT energies and a microkinetic model are summarized below following the reaction mechanisms studied by Grabow et al.[1] for Pt(111). This study uses the Perdew-Burke-Ernzerhof (PBE)[2] functional for all DFT calculations. All calculations have been performed with the Vienna ab initio Simulation Package (VASP).[3,4] Climbing image nudged elastic band and dimer methods are used to locate first order saddle points, i.e., the transition states.[5-7] Transition state theory and collision theory are used to calculate elementary step rate constants. Transition state theory is expressed as

$$k = \frac{k_B T}{h} \exp\left(-\frac{\Delta G^{\ddagger}}{k_B T}\right) \quad (1)$$

where k is the rate constant, k_B is Boltzmann's constant, h is Planck's constant, T is temperature, and $\Delta G^{\ddagger}$ is the free energy activation barrier. Lateral interactions due to two abundant surface intermediates, CO and H, are applied to all intermediates and transition states (see below). A 3x4x4 slab model of 48 Pt atoms is used for all DFT calculations. The top two layers are relaxed and the bottom two layers are fixed in the calculations. Calculated lattice constants are $a = 8.4342$ Å, $b = 9.7389$ Å, $c = 22.0000$ Å. A kinetic energy cutoff of 400 eV and a Gaussian smearing is 0.1 eV have been used in the DFT calculations.

Equations (2)-(16) summarize the elementary reaction steps considered in a microkinetic model used to solve for turnover frequency (TOF s^{-1}), reaction orders, and apparent activation barrier (eV).

$$* + CO \leftrightarrow CO^* \quad (2)$$

$$* + H_2O \leftrightarrow H_2O^* \quad (3)$$

$$* + H_2O^* \leftrightarrow H^* + OH^* \quad (4)$$

$$* + OH^* \leftrightarrow H^* + O^* \quad (5)$$

$$OH^* + OH^* \leftrightarrow H_2O^* + O^* \quad (6)$$

$$CO^* + O^* \leftrightarrow CO_2^* + * \quad (7)$$

$$* + COOH^* \leftrightarrow CO_2^* + H^* \quad (9)$$

$$COOH^* + O^* \leftrightarrow CO_2^* + OH^* \quad (10)$$

$$COOH^* + OH^* \leftrightarrow CO_2^* + H_2O^* \quad (11)$$

$$HCOO^* + * \leftrightarrow CO_2^* + H^* \quad (12)$$

$$HCOO^* + O^* \leftrightarrow CO_2^* + OH^* \quad (13)$$

$$HCOO^* + OH^* \leftrightarrow CO_2^* + H_2O^* \quad (14)$$

$$2H^* \leftrightarrow H_2 + 2* \quad (15)$$

$$CO_2^* \leftrightarrow CO_2 + * \quad (16)$$

$$HCO^* + * \leftrightarrow CO^* + H^* \quad (17)$$

Asterisks, *, refers to an adsorbed species or a vacant surface site if the asterisk is unaccompanied by a chemical species. Species without an asterisk are present in the gas phase. Table A.1 summarize the DFT results for water-gas shift (WGS) on Pt(111).

Table A.1. Activation barriers (eV) and reaction energies (eV) for elementary steps of the water-gas shift (WGS) reaction on Pt(111).

Reaction	Activation barrier (eV)	Reaction energy (eV)
$CO+^{*}\leftrightarrow CO^{*}$	0.0	-1.76
$H_2O+^{*}\leftrightarrow H_2O^{*}$	0.0	-0.14
$H_2O^{*}+^{*}\leftrightarrow H^{*}+OH^{*}$	0.76	0.42
$OH^{*}+^{*}\leftrightarrow H^{*}+O^{*}$	1.03	-0.15
$OH^{*}+OH^{*}\leftrightarrow H_2O^{*}+O^{*}$	0.0	0.43
$CO^{*}+O^{*}\leftrightarrow CO_2^{*}+^{*}$	1.05	-0.18
$CO^{*}+OH^{*}\leftrightarrow COOH^{*}+^{*}$	0.40	-0.11
$COOH^{*}+^{*}\leftrightarrow CO_2^{*}+H^{*}$	0.74	-0.22
$COOH^{*}+O^{*}\leftrightarrow CO_2^{*}+OH^{*}$	0.33	-0.07
$COOH^{*}+OH^{*}\leftrightarrow CO_2^{*}+H_2O^{*}$	0.0	-0.66
$HCOO^{*}+^{*}\leftrightarrow CO_2^{*}+H^{*}$	1.11	-0.57
$HCOO^{*}+O^{*}\leftrightarrow CO_2^{*}+OH^{*}$	1.44	-0.45
$HCOO^{*}+OH^{*}\leftrightarrow CO_2^{*}+H_2O^{*}$	1.06	-1.01
$2H^{*}\leftrightarrow H_2+2^{*}$	0.0	0.96
$CO_2^{*}\leftrightarrow CO_2+^{*}$	0.0	-0.05
$HCO^{*}+^{*}\leftrightarrow CO^{*}+H^{*}$	0.22	-1.15

A.2 LATERAL INTERACTION MODEL

The lateral interaction effects on surface intermediates and transition states due to the most abundant surface intermediates, CO and H, are considered. Without considering lateral interaction effects, the Pt(111) WGS microkinetic model becomes poisoned with CO (greater than 99.9% CO on the surface) and the activity is approximately 9 orders of magnitude less than with lateral interactions. Due to the nature of the catalyst model for the corner and edge active those models incorporate lateral interaction effects already.

In this section first we begin with an explanation of lateral interaction effects for Pt(111) including a comparison of the relative free energy pathways with and without lateral interaction effects. Next, Campbell's degree of rate control (DRC)[8-12] is explained and the sum of the DRC for all the elementary steps is shown to be one for Pt(111) with lateral interaction effects. Finally, a comparison with WGS on Pt(111) by Stamatakis, et al.[13] is conducted.

Figures A.1 and A.2 are examples of the lateral interaction effects due to CO and H. In fact, every intermediate and transition state includes lateral interaction effects due to CO and H such as those show in Figures A.1 and A.2. What Figures A.1 and A.2 show is a linear functional dependence on dimensionless surface coverage fraction of CO and H. This linear functional dependence is programmed into the microkinetic model.

(a)

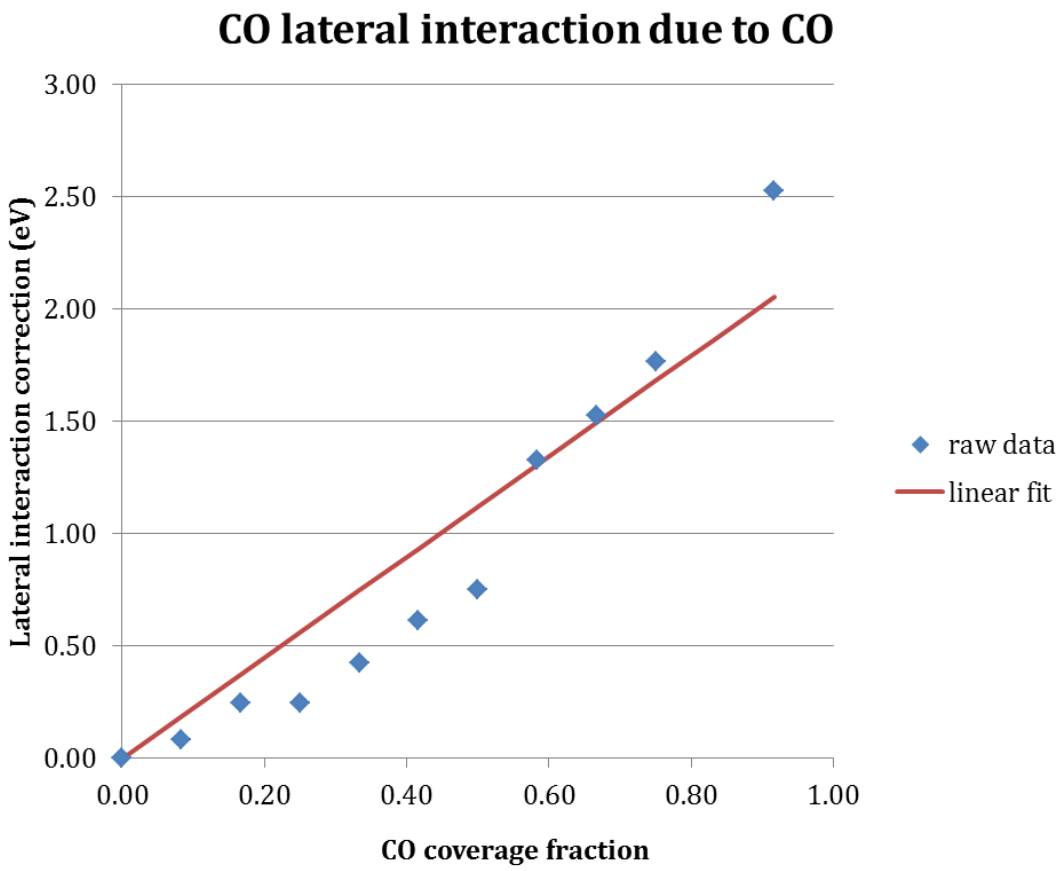
CO lateral interaction due to CO
Lateral interaction correction (eV)
3.00
2.50
2.00
1.50
1.00
0.50
0.00
0.00
0.20
0.40
0.60
0.80
1.00
CO coverage fraction
raw data
linear fit

(b)

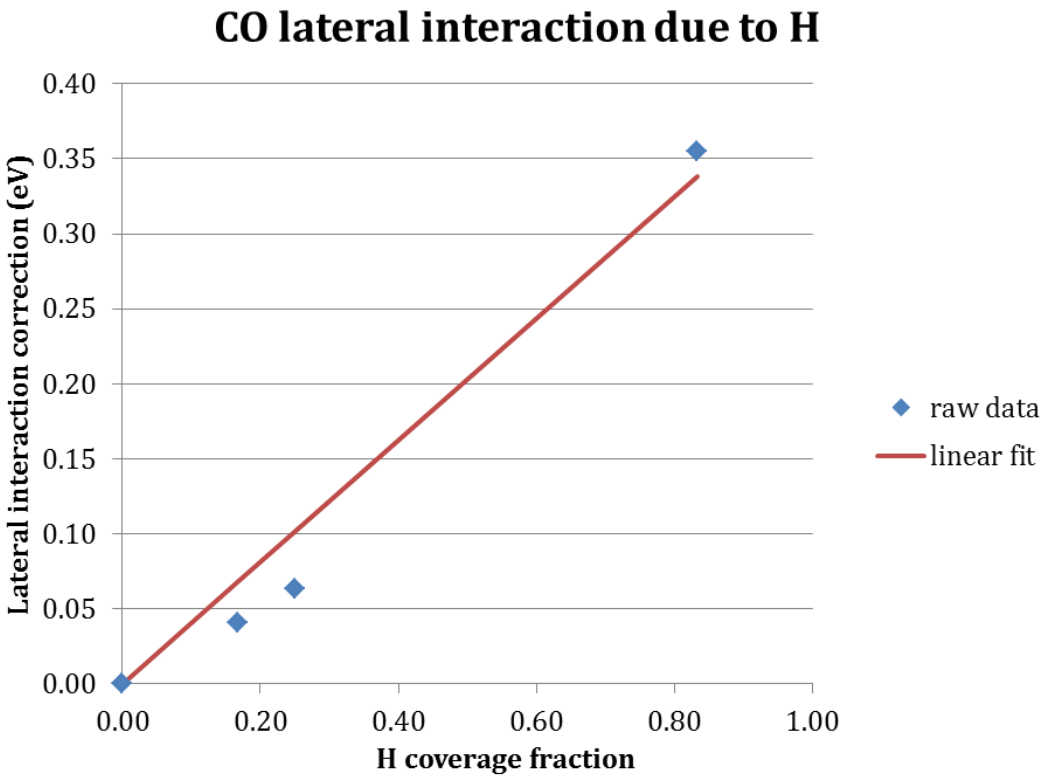

Figure A.1. Example lateral interaction effects (eV) on the CO surface intermediate. A linear functional dependence on CO and H dimensionless surface coverage fraction for lateral interaction effect (eV) is shown for the example of the CO surface intermediate. All surface intermediates and transition states have such a linear functional dependence. (a) CO lateral interaction due to CO. (b) CO lateral interaction due to H.

(a)

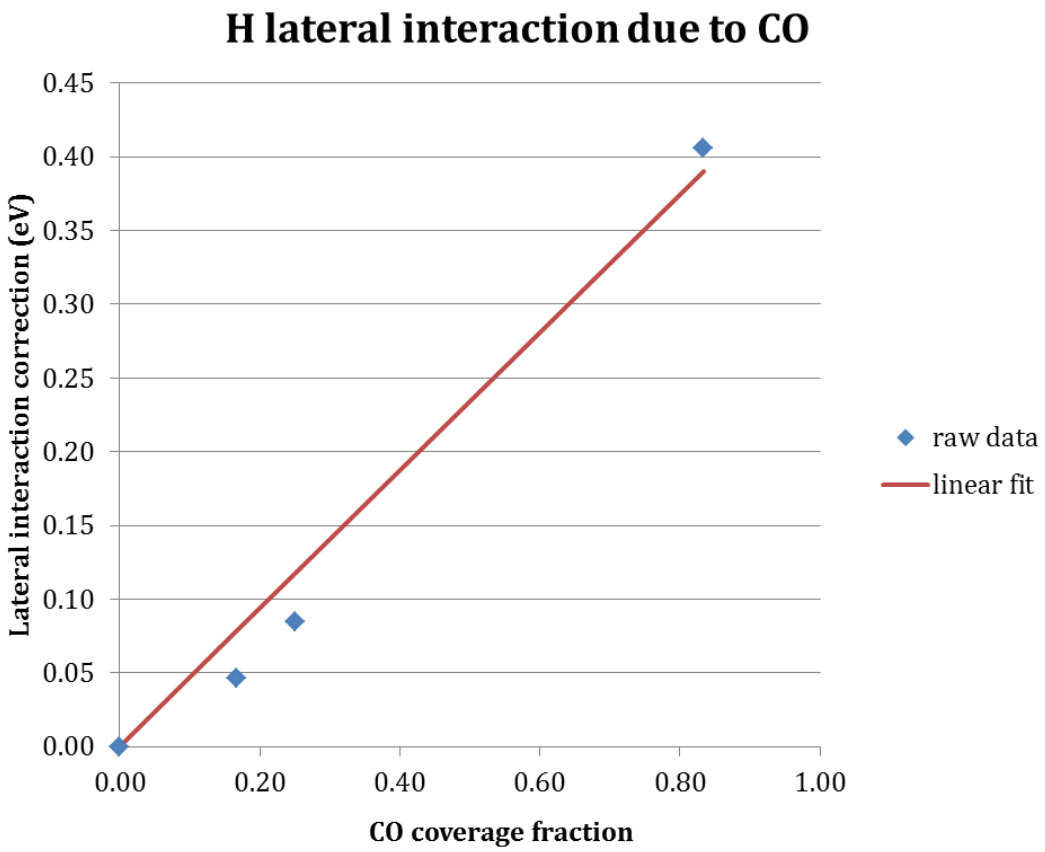
H lateral interaction due to CO
Lateral interaction correction (eV)
0.45
0.40
0.35
0.30
0.25
0.20
0.15
0.10
0.05
0.00
0.00
0.20
0.40
0.60
0.80
1.00
CO coverage fraction
raw data
linear fit

(b)

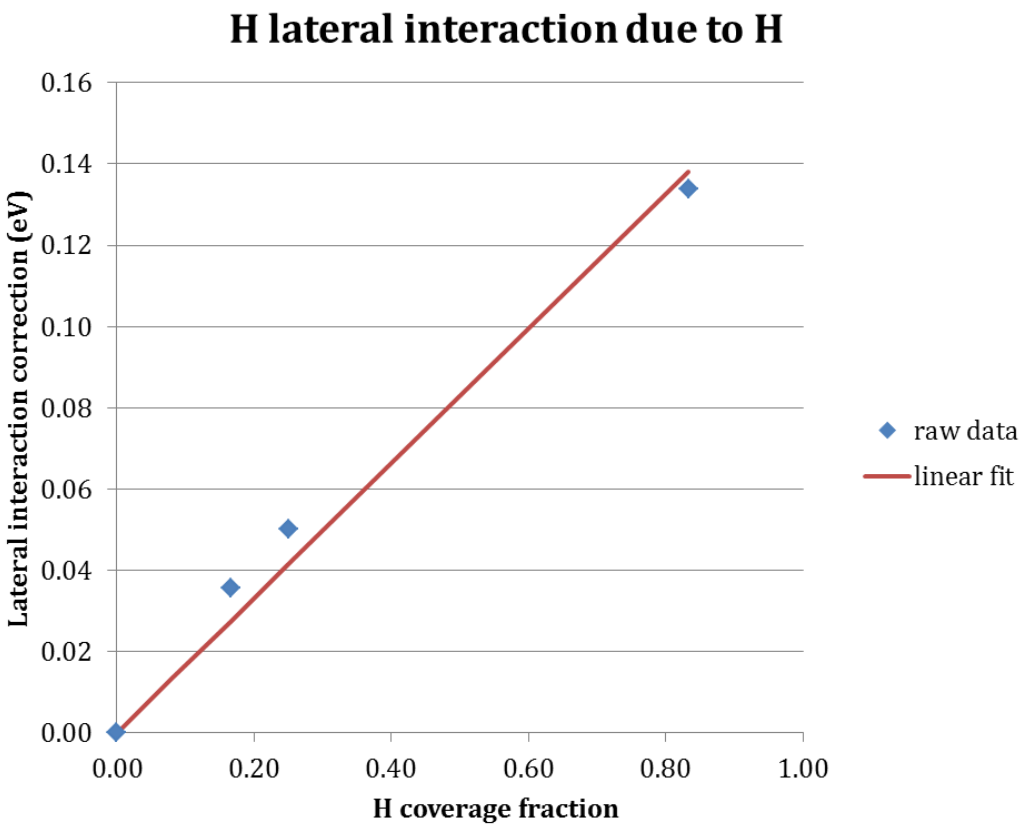

Figure A.2. Example lateral interaction effects (eV) on H surface intermediate. (a) H lateral interaction due to CO. (b) H lateral interaction due to H.

As stated above, all intermediates and transition states are affected by CO and H. The reason for considering all intermediates and transitions states is to not change the overall reaction thermodynamics. The free energy path of no lateral interactions and with lateral interactions are compared for the dominant (highest activity) reaction pathway in Figure A.3. The free energy paths represent the steady state achieved by the microkinetic model. As a confirmation of the thermodynamics not changing the last free energy are the same with and without lateral interactions. By maintaining thermodynamics were are enforcing consistency in the microkinetic model with the established thermodynamics of WGS.

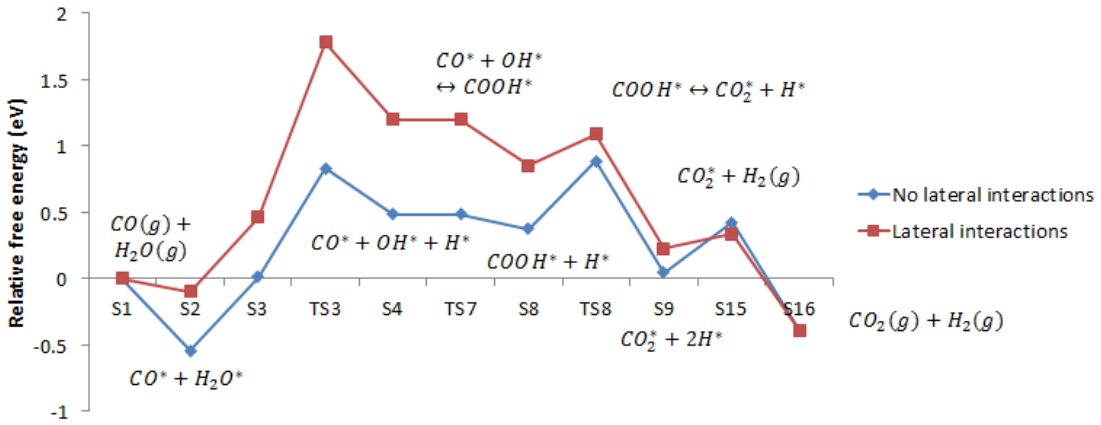

Figure A.3. Comparison of relative free energy paths for no lateral interactions and with lateral interactions. The free energy paths represent the steady state achieved by the microkinetic model. The overall reaction thermodynamics are not affected by the inclusion of lateral interactions, which is a verification of the implementation of lateral interaction effects. The dominant (most active) reaction pathway is displayed.

At this point we introduce the use of Campbell's DRC and apply it to Pt(111).[8-12] Campbell's DRC may be applied to any microkinetic model. Later in this work, for the edge active site model we analyze the uncertainty in DRC. The DRC for each elementary step for WGS on Pt(111) is listed in Table A.2. The formula for DRC is,[8-12]

$$X_{RC,i} = \left(\frac{\partial lnTOF}{\partial \frac{-G_i^{TS}}{k_B T}} \right)_{G_{j\neq i}^{TS}, G_m} \tag{18}$$

$X_{RC,i}$ is the degree of rate control for transition state i. Each individual transition state applies for a single elementary reaction step. G_i^{TS} is the relative free energy of transition state structure i. The temperature is held constant. All transition state relative free energies j (and intermediate relative free energies m) are held constant. It should be noted that a property of DRC is the sum of all DRC for a microkinetic model are one,[12,13]

$$\Sigma_i X_{RC,i} = 1 \tag{19}$$

This property holds true with the lateral interactions used is this work. The last row of Table A.2 shows the DRC summing to one.

Table A.2. Linear lateral interactions Campbell's degree of rate control (DRC) for each elementary step of WGS on Pt(111). These DRC correspond to the lateral interaction free energy pathway in Figure A.3. The last row shows the sum of all DRC for each elementary reaction step to be one, which is a verification for the implementation of the lateral interaction effects.

Elementary reaction step	Degree of rate control
$* + CO \leftrightarrow CO^*$	-3.5×10^{-12}
$* + H_2O \leftrightarrow H_2O^*$	-5.5×10^{-12}
$* + H_2O \leftrightarrow H^* + OH^*$	0.9995
$* + OH \leftrightarrow H^* + O^*$	-6.4×10^{-12}
$OH^* + OH^* \leftrightarrow H_2O^* + O^*$	0.0
$CO^* + O^* \leftrightarrow CO_2^* + *$	2.5×10^{-12}
$CO^* + OH^* \leftrightarrow COOH^* + *$	3.9×10^{-4}
$COOH^* + * \leftrightarrow CO_2^* + H^*$	1.3×10^{-6}
$COOH^* + O^* \leftrightarrow CO_2^* + OH^*$	1.1×10^{-11}
$COOH^* + OH^* \leftrightarrow CO_2^* + H_2O^*$	0.0
$HCOO^* + * \leftrightarrow CO_2^* + H^*$	1.1×10^{-11}
$HCOO^* + O^* \leftrightarrow CO_2^* + OH^*$	-5.5×10^{-12}
$HCOO^* + OH^* \leftrightarrow CO_2^* + H_2O^*$	-2.0×10^{-12}
$2H^* \leftrightarrow H_2 + 2^*$	-6.5×10^{-12}
$CO_2^* \leftrightarrow CO_2 + *$	3.5×10^{-12}
$HCO^* + * \leftrightarrow CO^* + H^*$	8.6×10^{-12}
Sum of all degrees of rate control	**0.99990**

Stamatakis, et al.[14] have found, using graph-theoretical kinetic monte carlo a higher TOF (s^{-1}) and lower apparent activation barrier than our microkinetic model. For comparison Table A.4 lists pre-exponential factors for rate constants and equilibrium constants. A is a pre-exponential factor. Using our zero-point corrected DFT energies and mean-field microkinetic model with the pre-exponential factors and lateral interactions affecting energies of Stamatakis, et al.[14] we obtain a TOF on the same order of magnitude at 650 K as Stamatakis, et al.[14] Therefore the cause for different TOF's is in the pre-exponential factors and lateral interactions.

Table A.3. T=650 K. †CO* + O* ↔ CO_2 + 2* is one reaction in Stamatakis, et al.[14]

Elementary step	A_{fwd} (s^{-1}) Stamatakis, et al.[1]	A_{fwd}/A_{bwd} Stamatakis, et al.[1]	A_{fwd} (s^{-1}) Walker, et al.	A_{fwd}/A_{bwd} Walker, et al.
$* + CO \leftrightarrow CO^*$	3.41×10^{5}	3.43×10^{-9}	1.34×10^{8}	2.85×10^{-8}
$* + H_2O \leftrightarrow H_2O^*$	7.20×10^{5}	1.69×10^{-7}	1.67×10^{8}	1.47×10^{-6}
$* + H_2O \leftrightarrow H^* + OH^*$	4.48×10^{12}	6.39	4.53×10^{12}	2.90×10^{-1}
$* + OH \leftrightarrow H^* + O^*$	2.36×10^{13}	19.8	3.49×10^{13}	5.20×10^{-1}
$OH^* + OH^* \leftrightarrow H_2O^* + O^*$	3.09×10^{11}	3.09	1.27×10^{13}	1.27
$CO^* + O^* \leftrightarrow CO_2^* + *$	1.17×10^{12}†	1.77×10^{7}†	4.42×10^{13}	8.25
$CO^* + OH^* \leftrightarrow COOH^* + *$	4.58×10^{11}	3.90×10^{-2}	2.73×10^{13}	8.91×10^{-1}
$COOH^* + * \leftrightarrow CO_2^* + H^*$	5.28×10^{14}	8.96×10^{9}	1.31×10^{14}	1.31×10^{1}
$COOH^* + O^* \leftrightarrow CO_2^* + OH^*$	6.93×10^{11}	4.53×10^{8}	1.88×10^{13}	8.40
$COOH^* + OH^* \leftrightarrow CO_2^* + H_2O^*$	1.04×10^{13}	1.40×10^{9}	5.55×10^{12}	1.76
$HCOO^* + * \leftrightarrow CO_2^* + H^*$	5.97×10^{13}	1.54×10^{10}	4.29×10^{13}	3.63
$HCOO^* + O^* \leftrightarrow CO_2^* + OH^*$	1.19×10^{12}	7.76×10^{8}	1.35×10^{13}	4.19×10^{-1}
$HCOO^* + OH^* \leftrightarrow CO_2^* + H_2O^*$	6.30×10^{12}	2.40×10^{9}	7.61×10^{13}	5.19
$2H^* \leftrightarrow H_2 + 2^*$	6.17×10^{12}	2.15×10^{5}	7.76×10^{14}	1.55×10^{6}
$CO_2^* \leftrightarrow CO_2 + *$	1.17×10^{12}†	1.77×10^{7}†	6.44×10^{16}	6.04×10^{8}
$HCO^* + * \leftrightarrow CO^* + H^*$	8.42×10^{12}	4.26×10^{1}	1.35×10^{13}	4.70×10^{-1}

A.3 BAYESIAN STATISTICS

This section introduces the proposed Bayesian framework for determining the active site. The Pt(111) model features reactions occurring on metal only and the other models feature pathways occurring at a TPB of Pt and a reducible oxide support, TiO_2. Even if uncertainty in results spans orders of magnitude a probability may be assigned to which model better explains experimental data. This comparison could provide an insight to the mechanism driving WGS. A first step in model selection is to calibrate each active site model, i.e. perform a Bayesian *inverse problem* on each active site model. The posterior distribution $p(\theta|D,M)$ corresponding to the parameters of one of the three models, i.e. $M = M_{corner}$, is obtained using Bayes' formula.

$$p(\theta|D,M) = \frac{p(D|\theta,M)p(\theta|M)}{p(D|M)} \tag{20}$$

The parameters θ are the corrections to all intermediate and transition state relative free energies from DFT as well as hyperparameters and corrections to gas molecule free energies. The posterior joint probability distribution represents the desired estimate of the parameters with quantified uncertainties given the experimental data D, and all prior information for the corresponding model. The prior information is encoded in the prior $p(\theta|M)$, which contains all the uncertainty settings including correlations and thermodynamics corrections as presented in Heyden, et al.[15]

The likelihood function $p(D|\theta,M)$ provides the likelihood of observing the experimental data D given the particular values of the parameters and the uncertainty in the model and experiment. Each experimental data set D consists of six individual measurements.

$$D = \{TOF, \alpha_{CO}, \alpha_{H_2O}, \alpha_{CO_2}, \alpha_{H_2}, E_{app}\} \quad (21)$$

Here α $(s^{-1}atm^{-1})$ is the reaction order and E_{app} (eV) is apparent activation energy and CO, H_2O, CO_2, H_2 correspond to carbon monoxide, water, carbon dioxide and hydrogen.

The six individual measurements are assumed to be independent given model parameters. This translates in the following factorization of the likelihood function.

$$p(D|\theta, M)$$
$$= p(TOF|\theta, M)p(\alpha_{CO}|\theta, M)p(\alpha_{H_2O}|\theta, M)p(\alpha_{CO_2}|\theta, M)p(\alpha_{H_2}|\theta, M)p(E_{app}|\theta, M) \quad (22)$$

Each individual likelihood function is defined by the discrepancy between the model simulations, i.e. E^*_{app} and experimental data, i.e. E_{app}. This discrepancy is due to unaccounted model errors and unknown experimental errors. Namely it is assumed that the discrepancy is normally distributed with zero mean and unknown variance, i.e. $\sigma^2_{E_{app}}$.

$$E_{app} = E^*_{app} + \epsilon_{E_{app}} \quad (23)$$

Therefore, the fully expanded likelihood function for the WGS calibration, is

$$p(D|\theta, M) = \frac{1}{\sqrt{2\pi\sigma^2_{TOF}}} \exp\left(-\frac{1}{2}\frac{(log_{10}TOF - log_{10}TOF^*)}{\sigma^2_{TOF}}\right) \frac{1}{\sqrt{2\pi\sigma^2_{\alpha_{CO}}}} \exp\left(-\frac{1}{2}\frac{(\alpha_{CO}-\alpha^*_{CO})^2}{\sigma^2_{\alpha_{CO}}}\right) \times$$
$$\frac{1}{\sqrt{2\pi\sigma^2_{\alpha_{H_2O}}}} \exp\left(-\frac{1}{2}\frac{(\alpha_{H_2O}-\alpha^*_{H_2O})^2}{\sigma^2_{\alpha_{H_2O}}}\right) \frac{1}{\sqrt{2\pi\sigma^2_{\alpha_{CO_2}}}} \exp\left(-\frac{1}{2}\frac{(\alpha_{CO_2}-\alpha^*_{CO_2})^2}{\sigma^2_{\alpha_{CO_2}}}\right) \times$$
$$\frac{1}{\sqrt{2\pi\sigma^2_{\alpha_{H_2}}}} \exp\left(-\frac{1}{2}\frac{(\alpha_{H_2}-\alpha^*_{H_2})^2}{\sigma^2_{\alpha_{H_2}}}\right) \frac{1}{\sqrt{2\pi\sigma^2_{E_{app}}}} \exp\left(-\frac{1}{2}\frac{(E_{app}-E^*_{app})^2}{\sigma^2_{E_{app}}}\right) \quad (24)$$

The hyperparameters σ_{TOF}^2, $\sigma_{\alpha_{CO}}^2$, $\sigma_{\alpha_{H_2O}}^2$, $\sigma_{CO_2}^2$, $\sigma_{H_2}^2$, $\sigma_{E_{app}}^2$ are calibrated along with DFT and gas molecules corrections. The standard deviations of discrepancies are given prior inverse gamma pdfs, which allows them to extend to infinity, however with most of the probability concentrated around a prior value.

Note, that in all models, there is a constraint on the parameters such that the activation barrier for any elementary step is guaranteed to be non-negative.

When N experimental data sets are available, $\{D\}_{i=1..N}$ then they are assumed to be independent and identically distributed, yielding the following likelihood function.

$$p(\{D\}_{i=1..N}|\theta, M) = \prod_{i=1}^{N} p(D_i|\theta, M) \tag{25}$$

The marginal likelihood $p(D|M)$ acts as both a normalization constant as well as a key quantity in model comparison. It is a natural formulation of Occam's razor, providing an automatic trade-off between goodness-of-fit and model complexity. The evidence can be used to calculate the posterior model probabilities using Bayes' rule as well.

$$p(M|D) = \frac{p(D|M)p(M)}{p(D)} \tag{26}$$

In the absence of information regarding which model is better at describing the physics of interest, the prior model probabilities are set to $p(M_{edge}) = p(M_{corner}) = p(M_{terrace}) = \frac{1}{3}$. Note, that in this case the evidence can be used directly to compare the proposed models.

The evidence can be written as the difference between the expected log-likelihood of the data and the Kullback-Leibler[16,17] (KL) divergence between posterior and prior pdf of

model parameters. The expected log-likelihood quantifies how well the model fits the data, and the KL divergence quantifies model complexity. A large divergence between the posterior and prior pdfs suggest over-fitting of experimental data. Therefore, a complex model is penalized meaning it might not be selected over a simpler model that does not explain the data as well. KL divergence has been previously used[15] to determine the distance of two catalytic cycle TOF (s^{-1}) pdf's divergence from overall TOF (s^{-1}). Thus, KL divergence served as a formalization of dominant pathway.

Once both the TPB models and the Pt(111) model are calibrated using the same data, the evidences, $p(D|M)$, of each calibration can be divided to produce a Bayes' factor.

$$B_{edge/corner} = \frac{p(D|M_{edge})}{p(D|M_{corner})} \tag{27}$$

The Bayes' factor can be judge using Jeffrey's scale to determine whether there is significant difference between two model evidences.

In general, sampling from the posterior probability density, $p(\theta|D,M)$ and approximating the model evidence, $p(D|M)$ is not a trivial task. Here, we are using the multilevel sampling algorithm in the statistical library QUESO.[18,19] The multilevel algorithm reduces two potential drawbacks of MCMC algorithms. First, the MCMC may take too small steps and either not arrive at the high-probability region of the parameter space or the chain may be inside the high probability region but not sample all of it. Second, the steps may be too large that they skip over the high probability region entirely. A sequence of intermediate distributions are sampled on the way to the final

target distribution. The first sampled pdf is flattened and becomes more like the prior pdf. This is achieved by the following factorization of the likelihood.

$$p(\theta|D,M) = \frac{\prod_{j=1}^{L} p(D|\theta,M)^{\alpha_j} p(\theta|M)}{p(D|M)} \quad (28)$$

$$\sum_{j=1}^{L} \alpha_j = 1 \quad (29)$$

The overall log evidence is the sum of the log evidences at each level of the multilevel sampling where j is the level and L is the total number of levels.[19-21]

A.4 FOUR FUNCTIONAL CALCULATIONS FOR TERRACE AND CORNER SITES

The same approach which was applied to the edge active site is applied to the corner site[22] and a newly-calculated from DFT Pt(111). In the case of the edge active site, the CO-promoted redox cycle was determined to be dominant up to 650 K at which point the two cycles are competitive and after which classical redox is dominant.[15] In this work we will evaluate CO-promoted redox versus associated carboxyl redox for the corner site[22] and a formate pathway versus carboxyl pathway for Pt(111). Pt(111) has a mean-field reaction on the surface instead of catalytic cycles. Table S10 is the relative free energies as calculated by four functionals. The results of the Bayesian inverse in the free energy parameter space are visualized in Figures A.12-A.13. The verification of the edge posterior at 50K higher temperature and separate pressure conditions are shown in Figure A.14.

Previously, Heyden, et al.[15] four functionals were calculated to obtain a prior (before Bayesian inverse) uncertainty. The same four functionals which were calculated for the to the edge active site[15] are calculated for the the corner active site[22] and the Pt(111) active site. Tables A.4-A.5 list the relative free energies as calculated by four

functionals for Pt(111). The results of the Bayesian inverse in the free energy parameter space are visualized in Figures A.4-A.5.

Table A.4. Relative free energies as calculated by four functionals[2,23-27] for Pt(111).

	ΔG (eV)			
Reaction	**PBE**	**RPBE**	**M06L**	**HSE**
vacancy	0.000	0.000	0.000	0.000
$CO(g)+^{*}\leftrightarrow CO^{*}$	0.000	0.000	0.000	0.000
CO^{*}	-1.820	-1.421	-1.486	-1.811
$H_2O(g)+^{*}\leftrightarrow H_2O^{*}$	0.000	0.000	0.000	0.000
H_2O^{*}	-0.241	-0.017	-0.258	-0.355
$H_2O^{*}\leftrightarrow H^{*}+OH^{*}$	0.669	1.041	0.964	0.886
H^{*}	-0.980	-0.645	-0.343	-1.217
OH^{*}	-2.266	-1.853	-1.920	-1.997
$OH^{*}\leftrightarrow\ H^{*}+O^{*}$	-1.242	-0.794	-0.582	-0.553
$O*$	-4.579	-4.088	-3.601	-3.527
$OH^{*}+OH^{*}\leftrightarrow H_2O^{*}+O^{*}$	-4.531	-3.707	-3.840	-3.994
$CO^{*}+\ O^{*}\leftrightarrow CO_2^{*}\ +*$	-5.236	-4.466	-4.072	-3.950
CO_2^{*}	-0.020	-0.006	-0.042	-0.014
$CO^{*}+OH^{*}\leftrightarrow\ COOH^{*}+*$	-3.596	-2.895	-3.018	-0.993
$COOH*$	-2.291	-1.947	-2.307	-2.294
$COOH^{*}+*\leftrightarrow CO_2^{*}+\ H^{*}$	-1.401	-1.947	-1.298	-2.018
$COOH^{*}+O^{*}\leftrightarrow CO_2^{*}+OH^{*}$	-6.510	-5.626	-5.540	-5.463
$COOH^{*}+OH^{*}\leftrightarrow CO_2^{*}+H_2O^{*}$	-4.557	-3.800	-2.370	-4.291
$HCOO^{*}+*\leftrightarrow CO_2^{*}+H^{*}$	-1.262	-0.770	-1.356	-1.569
$HCOO*$	-2.375	-1.913	-2.486	-2.750
$HCOO^{*}+O^{*}\leftrightarrow CO_2^{*}+OH^{*}$	-5.447	-4.596	-4.408	-4.263
$HCOO^{*}+OH^{*}\leftrightarrow CO_2^{*}+H_2O^{*}$	-3.403	-2.519	-2.945	-3.105
$2H^{*}\leftrightarrow H_2+2*$	0.000	0.000	0.000	0.000
$CO_2^{*}\leftrightarrow CO_2+*$	0.000	0.000	0.000	0.000

$HCO^* + * \leftrightarrow CO^* + H^*$	-2.077	-1.731	-1.877	-1.978
HCO^*	-2.372	-2.098	-2.332	-2.312

Table A.5. Relative free energies as calculated by four functionals for the interface corner active site.[22]

Reaction	**ΔG (eV)**			
	PBE	**RPBE**	**HSE**	**M06L**
$*_{Pt}$ (IM1) + $2CO_{(g)}$ + $H_2O_{(g)}$	0.000	0.000	0.000	0.000
$*_{Pt}$ (IM1) + $2CO_{(g)}$ + $H_2O_{(g)}$→ CO_{Pt} (IM2) + $CO_{(g)}$ + $H_2O_{(g)}$	0.000	0.000	0.000	0.000
CO_{Pt} (IM2) + $*_{Ti}$ + $CO_{(g)}$ + $H_2O_{(g)}$	-0.468	-0.194	-0.469	-0.014
CO_{Pt} (IM2) + $*_{Ti}$ + $CO_{(g)}$ + $H_2O_{(g)}$→CO_{Pt}-H_2O_{Ti} (IM3) + $CO_{(g)}$	-0.468	-0.194	-0.469	-0.014
CO_{Pt}-H_2O_{Ti} (IM3) + O_b + $CO_{(g)}$	0.072	0.604	0.072	0.237
CO_{Pt}-H_2O_{Ti} (IM3) + O_b + $CO_{(g)}$→CO_{Pt}-OH_{Ti}-O_bH (IM4) + $CO_{(g)}$	0.305	0.971	0.326	0.624
CO_{Pt}-OH_{Ti}-O_bH (IM4) + $CO_{(g)}$	0.266	0.856	0.188	0.261
CO_{Pt}-OH_{Ti}-O_bH (IM4) + $CO_{(g)}$ → $COOH_{(Pt-Ti)}$-O_bH (IM5) + $CO_{(g)}$	0.818	1.589	0.810	0.958
$COOH_{(Pt-Ti)}$-O_bH (IM5)+ O_s+ $CO_{(g)}$	0.707	1.495	0.646	0.955
$COOH_{(Pt-Ti)}$-O_bH (IM5)+ O_s+ $CO_{(g)}$ →$CO_{2(Pt-Ti)}$-O_bH-O_sH (IM6) + $CO_{(g)}$	1.204	2.093	1.296	1.949
$CO_{2(Pt-Ti)}$-O_bH-O_sH (IM6) + $CO_{(g)}$	1.178	2.086	1.196	1.497
$CO_{2(Pt-Ti)}$-O_bH-O_sH (IM6) + $CO_{(g)}$ → $*_{Pt}$-O_bH-O_sH (IM7) + $*_{Ti}$ + $CO_{(g)}$ + $CO2_{(g)}$	1.178	2.086	1.196	1.497
$*_{Pt}$-O_bH-O_sH (IM7) + $*_{Pt}$ + $CO_{(g)}$ + $CO2_{(g)}$	0.529	0.987	1.078	0.505
$*_{Pt}$-O_bH-O_sH (IM7) + $*_{Pt}$ + $CO_{(g)}$ + $CO2_{(g)}$ → $*_{Pt}$-H_{Pt}-O_bH (IM8) + O_s+ $CO_{(g)}$ + $CO2_{(g)}$	0.754	1.196	1.601	1.241
$*_{Pt}$-H_{Pt}-O_bH (IM8) + O_s+ $CO_{(g)}$ + $CO2_{(g)}$	-0.161	0.173	-0.015	0.068
$*_{Pt}$-H_{Pt}-O_bH (IM8) + O_s + $CO_{(g)}$ + $CO2_{(g)}$→ $*_{Pt}$-H_{Pt}-O_sH (IM9) + O_b+ $CO_{(g)}$ + $CO2_{(g)}$	0.433	0.817	0.686	1.341
$*_{Pt}$-H_{Pt}-O_sH (IM9) + $CO_{(g)}$ + $CO2_{(g)}$	0.366	0.713	0.552	0.953
$*_{Pt}$-H_{Pt}-O_sH (IM9) + $CO_{(g)}$ + $CO2_{(g)}$ → $2H_{Pt}$ (IM10) + O_s+ $CO_{(g)}$ + $CO2_{(g)}$	0.556	0.880	0.881	1.450
$2H_{Pt}$ (IM10) + $CO_{(g)}$ + $CO2_{(g)}$	-0.272	-0.009	-0.210	0.345
$2H_{Pt}$ (IM10) + $CO_{(g)}$ + $CO2_{(g)}$→ $*_{Pt}$ (IM1) + $*_{Pt}$+ $CO_{(g)}$ + $CO2_{(g)}$ + $H_{2(g)}$	-0.272	-0.009	-0.210	0.345

$*_{Pt}$ (IM1) + $*_{Pt}$+ $CO_{(g)}$ + $CO2_{(g)}$ + $H_{2(g)}$	-0.638	-0.590	-0.440	-0.772
CO_{Pt} (IM2) + $CO_{(g)}$ + $H_2O_{(g)}$→ $(CO,CO)_{Pt}$ (IM11) + $H_2O_{(g)}$	-0.468	-0.194	-0.469	-0.014
$(CO,CO)_{Pt}$ (IM11) + O_i + $H_2O_{(g)}$	-0.834	-0.775	-0.699	-1.131
$(CO,CO)_{Pt}$ (IM11) + O_i + $H_2O_{(g)}$→ $(CO,CO_2)_{Pt\text{-}Oi}$ (IM12) + $H_2O_{(g)}$	-0.307	-0.037	-0.113	-0.547
$(CO,CO_2)_{Pt\text{-}Oi}$ (IM12) + $H_2O_{(g)}$	-0.432	-0.152	-0.205	-0.685
$(CO,CO_2)_{Pt\text{-}Oi}$ (IM12) + $H_2O_{(g)}$→ CO_{Pt}-V_i (IM13) + $H_2O_{(g)}$+ $CO_{2(g)}$	0.900	1.038	2.083	0.256
CO_{Pt}-V_i (IM13) + $H_2O_{(g)}$+ $CO_{2(g)}$	-0.466	-0.633	0.824	-1.026
CO_{Pt}-V_i (IM13) + $H_2O_{(g)}$+ $CO_{2(g)}$→ CO_{Pt}-H_2O_i (IM14) + $CO_{2(g)}$	-0.466	-0.633	0.824	-1.026
CO_{Pt}-H_2O_i (IM14) + $*_{Pt}$ + $CO_{2(g)}$	-0.287	-0.114	0.842	-0.617
CO_{Pt}-H_2O_i (IM14) + $*_{Pt}$ + $CO_{2(g)}$ → CO_{Pt}-H_{Pt}-O_iH (IM15) + $CO_{2(g)}$	-0.253	-0.108	0.518	-0.550
CO_{Pt}-H_{Pt}-O_iH (IM15) + $CO_{2(g)}$	-1.114	-0.896	-0.886	-1.338
CO_{Pt}-H_{Pt}-O_iH (IM15) + $CO_{2(g)}$→ $(CO,H)_{Pt}$-H_{Pt} (IM16) + O_i + $CO_{2(g)}$	-1.051	-0.842	-0.774	-1.096
$(CO,H)_{Pt}$-H_{Pt} (IM16) + $CO_{2(g)}$	-1.246	-1.152	-1.120	-1.445
$(CO,H)_{Pt}$-H_{Pt} (IM16) + $CO_{2(g)}$ → CO_{Pt} (IM2) + $*_{Pt}$+ $CO_{2(g)}$ + H_2(g)	-1.246	-1.152	-1.120	-1.445
CO_{Pt} (IM2) + $*_{Pt}$+ $CO_{2(g)}$ + H_2(g)	-1.324	-1.245	-1.030	-2.101

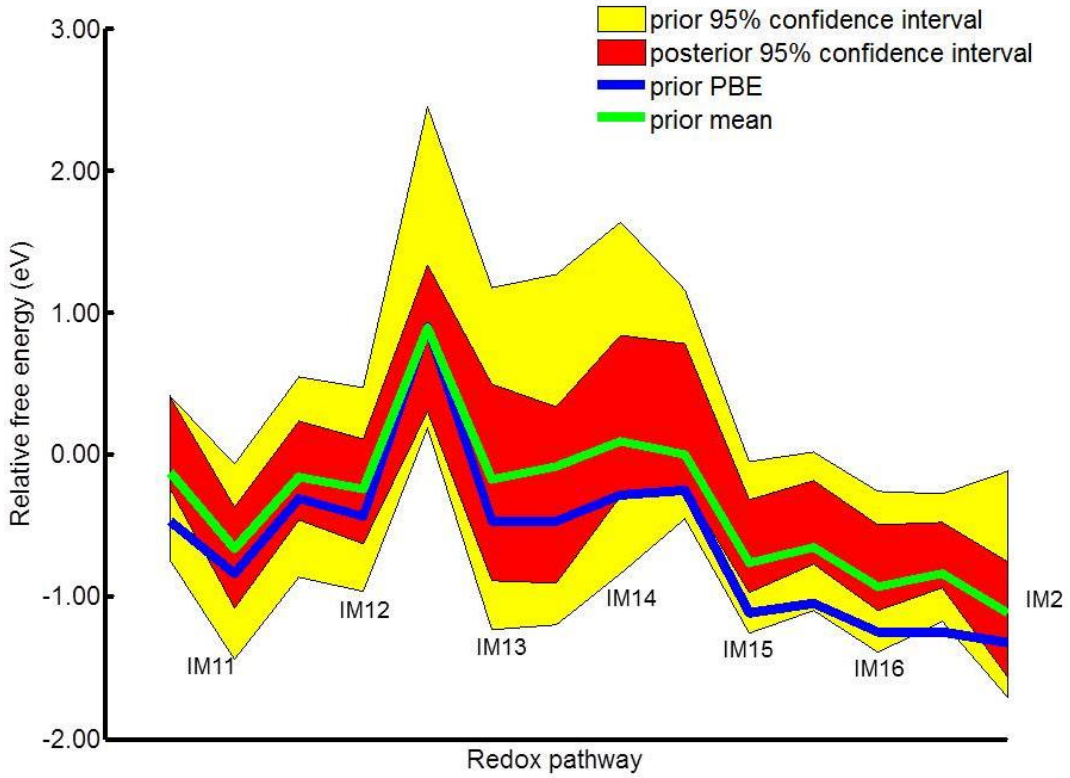

Figure A.4. Prior and posterior uncertainty in the dominant free energy path for the corner active site. The experiment used in the Bayesian inverse is from Kalamaras, et al.[28] which is at the conditions T=523 (K), $P_{CO} = 0.03$ (atm), $P_{H_2O} = 0.1$, $P_{CO_2} = 0.06$, $P_{H_2} = 0.2$.

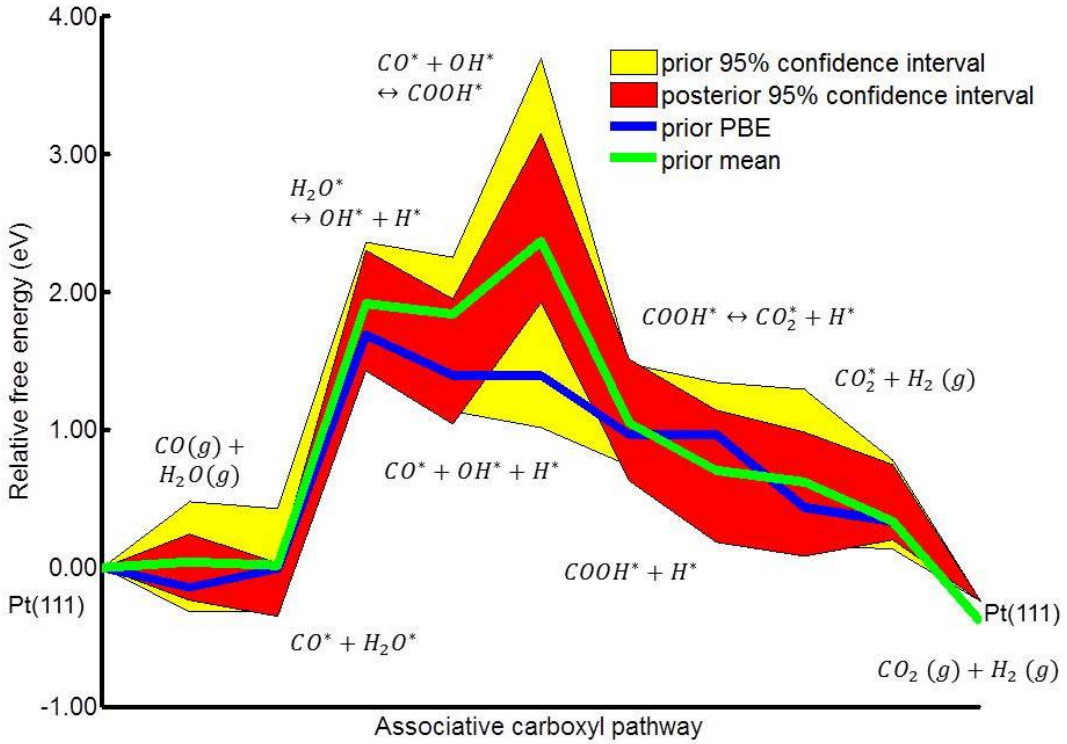

Figure A.5. Prior and posterior uncertainty in the dominant free energy path for the terrace Pt(111) active site. The experiment used in the Bayesian inverse is from Kalamaras, et al.[28] which is at the conditions T=523 (K), $P_{CO} = 0.03$ (atm), $P_{H_2O} = 0.1$, $P_{CO_2} = 0.06$, $P_{H_2} = 0.2$.

A.5 ACTIVE SITE SELECTION

This section presents details concerning the active site selection which are not presented in the main text. First, discrepancy model standard deviations, σ, in Equation 24 require a prior uncertainty because they are tuned during the Bayesian inverse. The prior uncertainty is an inverse gamma probability density function with the α,β listed in Table A.6. These settings in Table A.6. Next, the DRC of the edge active site model under uncertainty are displayed. Finally, the Bayesian inverse results for the corner and edge active site model are reported (results from the selected edge active site model are present in the main text).

Table A.6. Discrepancy model standard deviations inverse gamma priors. These hyperparameters are given a prior uncertainty because they are tuned during the Bayesian inverse. Inverse gamma is a probability density function.

$TOF\ (s^{-1})$		α_{CO}		α_{H_2O}		α_{CO_2}		α_{H_2}		$E_{act}\ (eV)$	
α	β	α	β	α	β	α	β	α	β	α	β
3	4	3	0.4	3	0.4	3	0.4	3	0.4	3	0.8

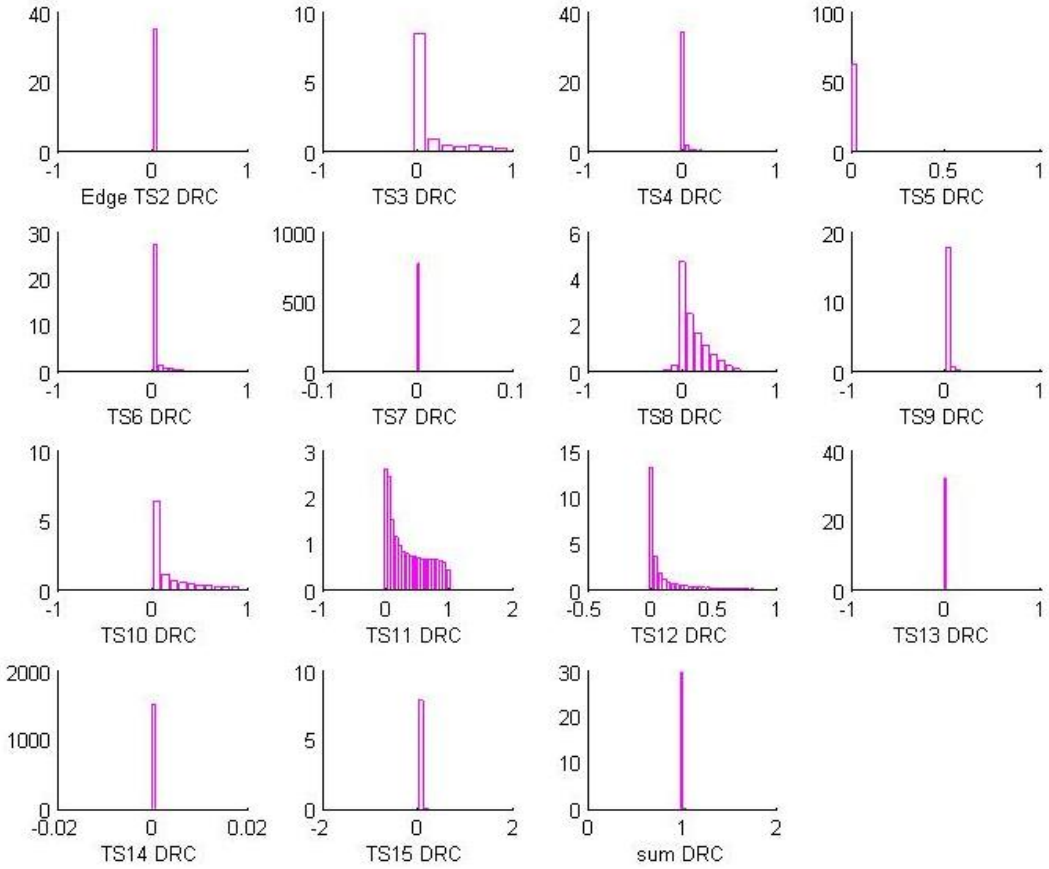

Figure A.6. Degrees of rate control for classical and CO-promoted pathways for edge active sites posterior.

(a)

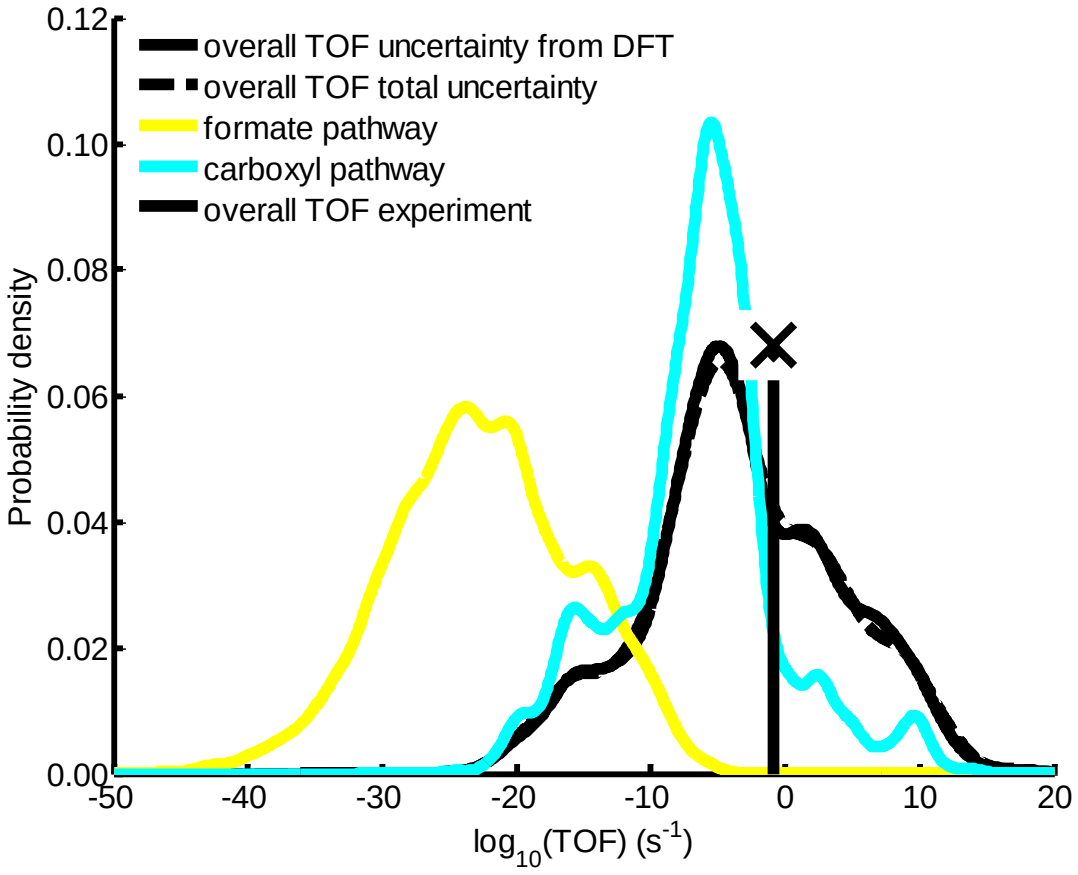

Figure A.7. Terrace Pt(111) posterior TOF (s^{-1}). The experiment used for obtaining the posterior is from Kalamaras, et al.[28] which is at the conditions T=523 (K), $P_{CO} = 0.03$ (atm), $P_{H_2O} = 0.1$, $P_{CO_2} = 0.06$, $P_{H_2} = 0.2$. For the terrace site the overall large uncertainties are due to the search for a higher-evidence region of the parameter space which is not obtained but instead the limit of log-likelihood of 100 is constant while the uncertainty increases.

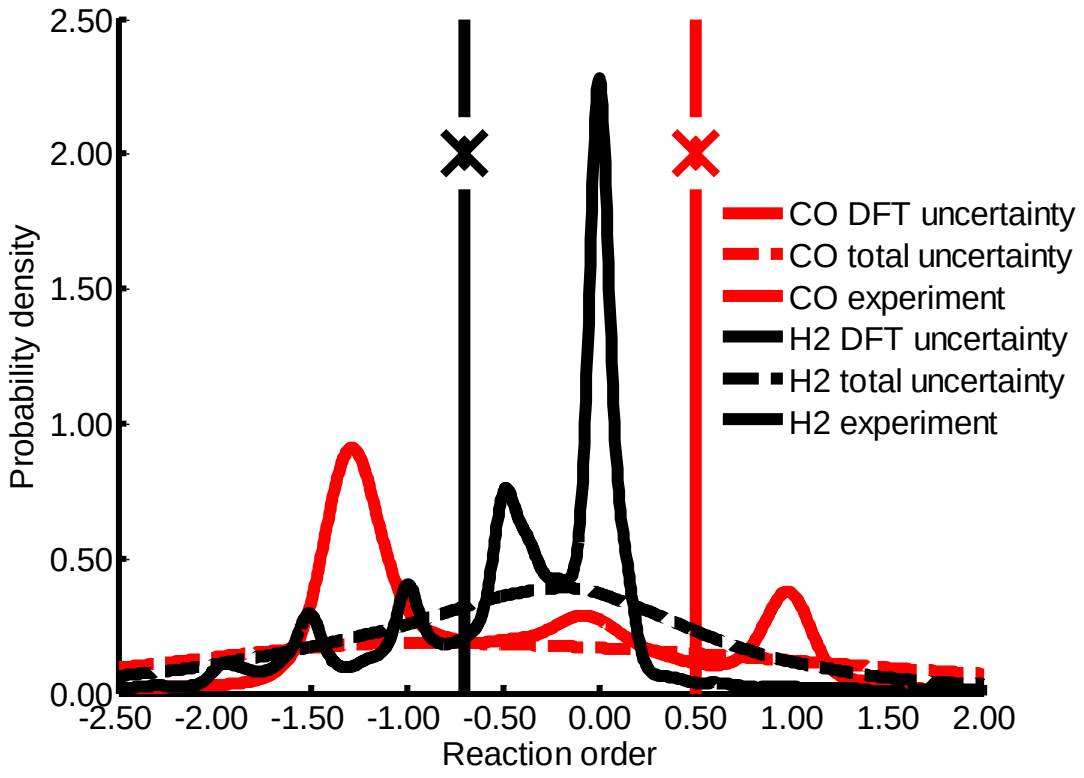

Figure A.8. Terrace Pt(111) posterior reaction orders CO and H_2. The experiment used for obtaining the posterior is from Kalamaras, et al.[28] which is at the conditions T=523 (K), $P_{CO} = 0.03$ (atm), $P_{H_2O} = 0.1$, $P_{CO_2} = 0.06$, $P_{H_2} = 0.2$.

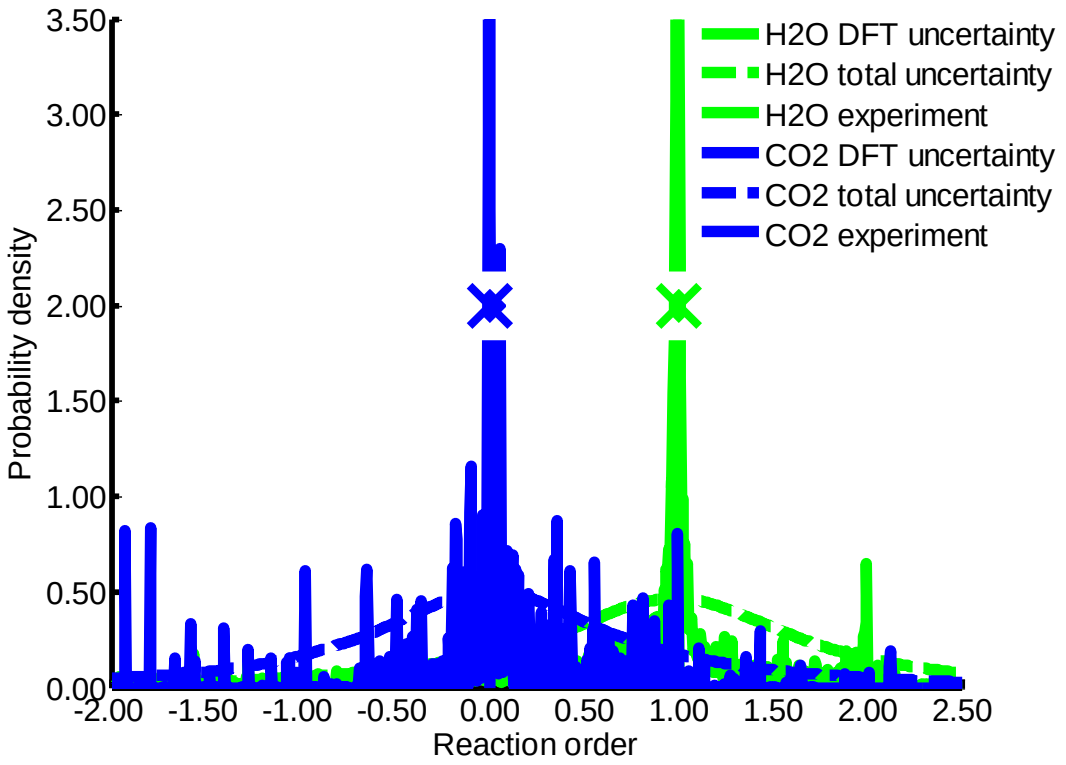

Figure A.9. Terrace Pt(111) posterior reaction orders H_2O and CO_2. The experiment used for obtaining the posterior is from Kalamaras, et al.[28] which is at the conditions T=523 (K), $P_{CO} = 0.03$ (atm), $P_{H_2O} = 0.1$, $P_{CO_2} = 0.06$, $P_{H_2} = 0.2$.

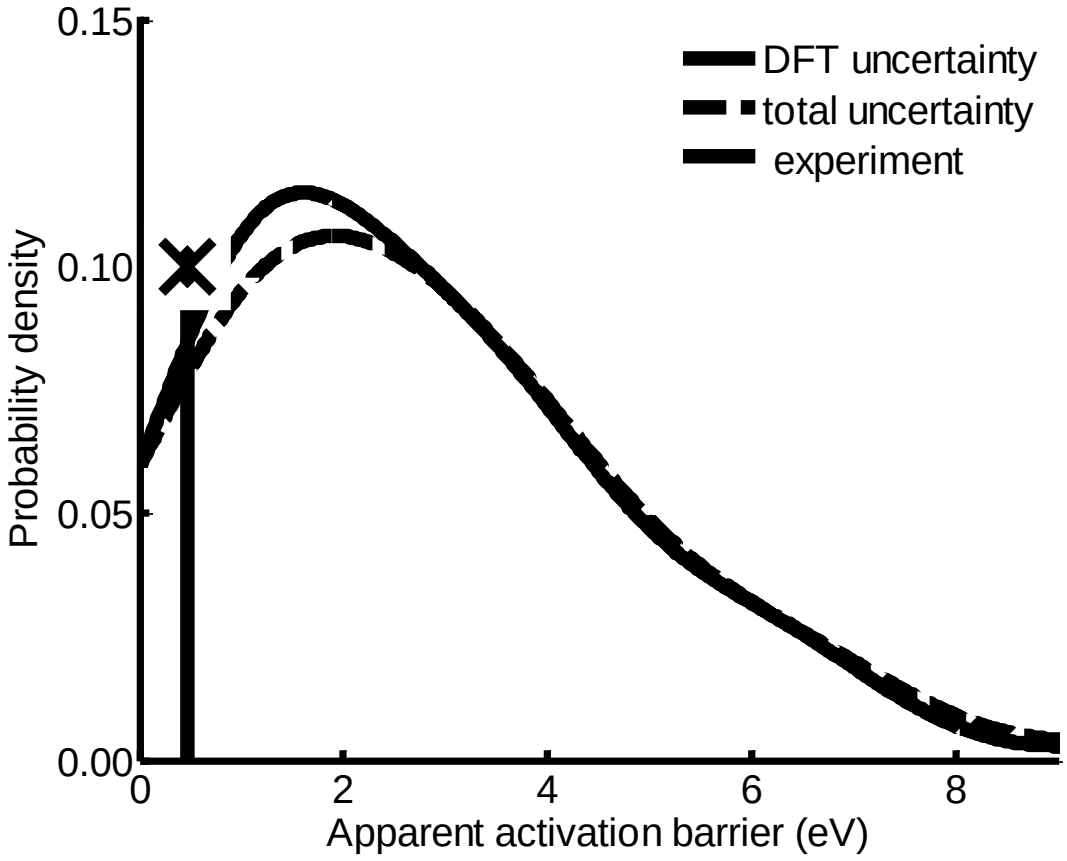

Figure A.10. Terrace Pt(111) posterior apparent activation barrier (eV). The experiment used for obtaining the posterior is from Kalamaras, et al.[28] which is at the conditions T=523 (K), $P_{CO} = 0.03$ (atm), $P_{H_2O} = 0.1$, $P_{CO_2} = 0.06$, $P_{H_2} = 0.2$.

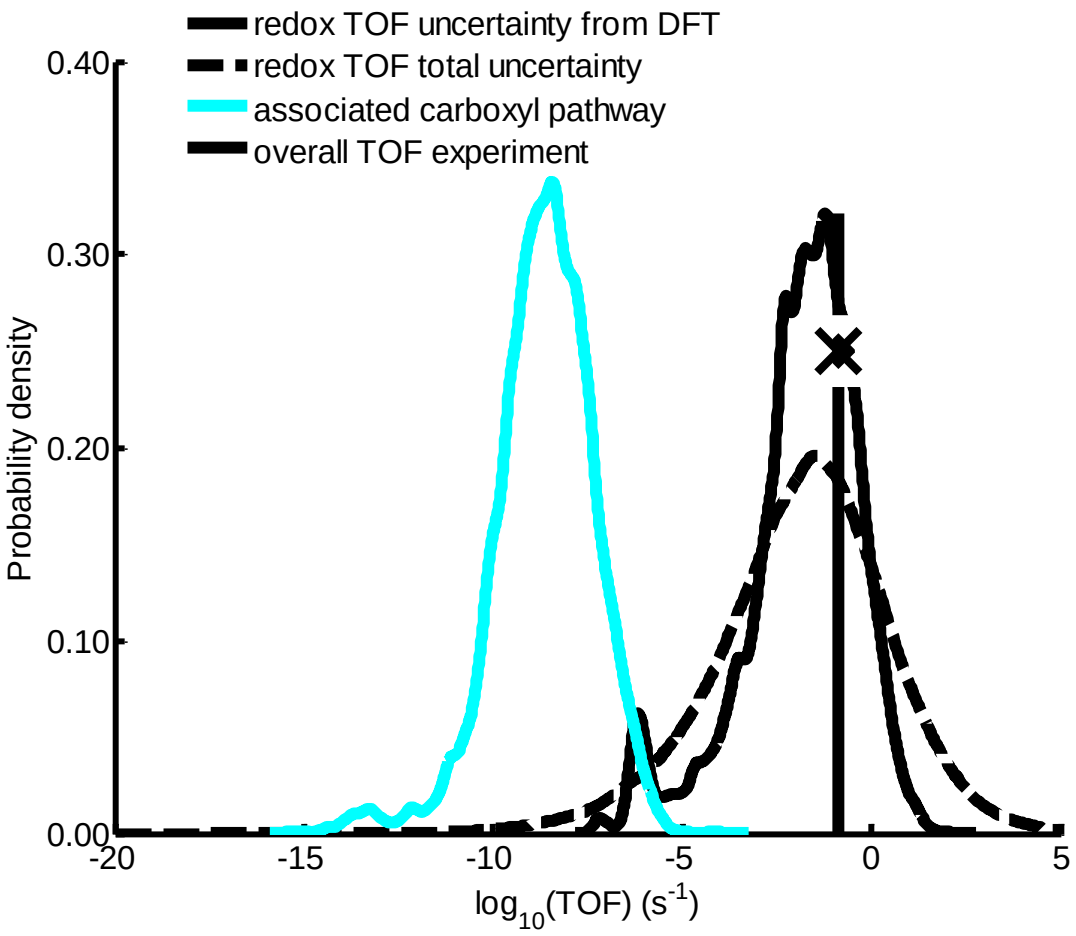

Figure A.11. Corner active site posterior TOF (s^{-1}). The experiment used for obtaining the posterior is from Kalamaras, et al.[28] which is at the conditions T=523 (K), $P_{CO} = 0.03$ (atm), $P_{H_2O} = 0.1$, $P_{CO_2} = 0.06$, $P_{H_2} = 0.2$.

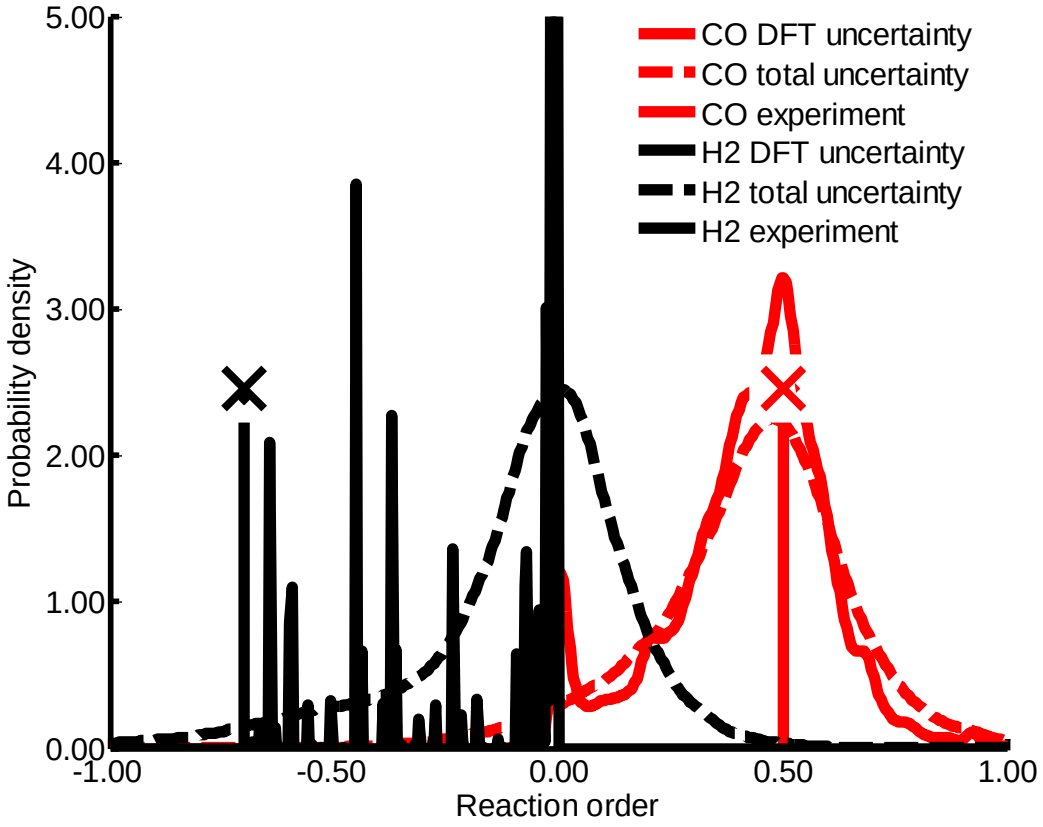

Figure A.12. Corner active site posterior reaction orders CO and H_2. The experiment used for obtaining the posterior is from Kalamaras, et al.[28] which is at the conditions T=523 (K), $P_{CO} = 0.03$ (atm), $P_{H_2O} = 0.1$, $P_{CO_2} = 0.06$, $P_{H_2} = 0.2$.

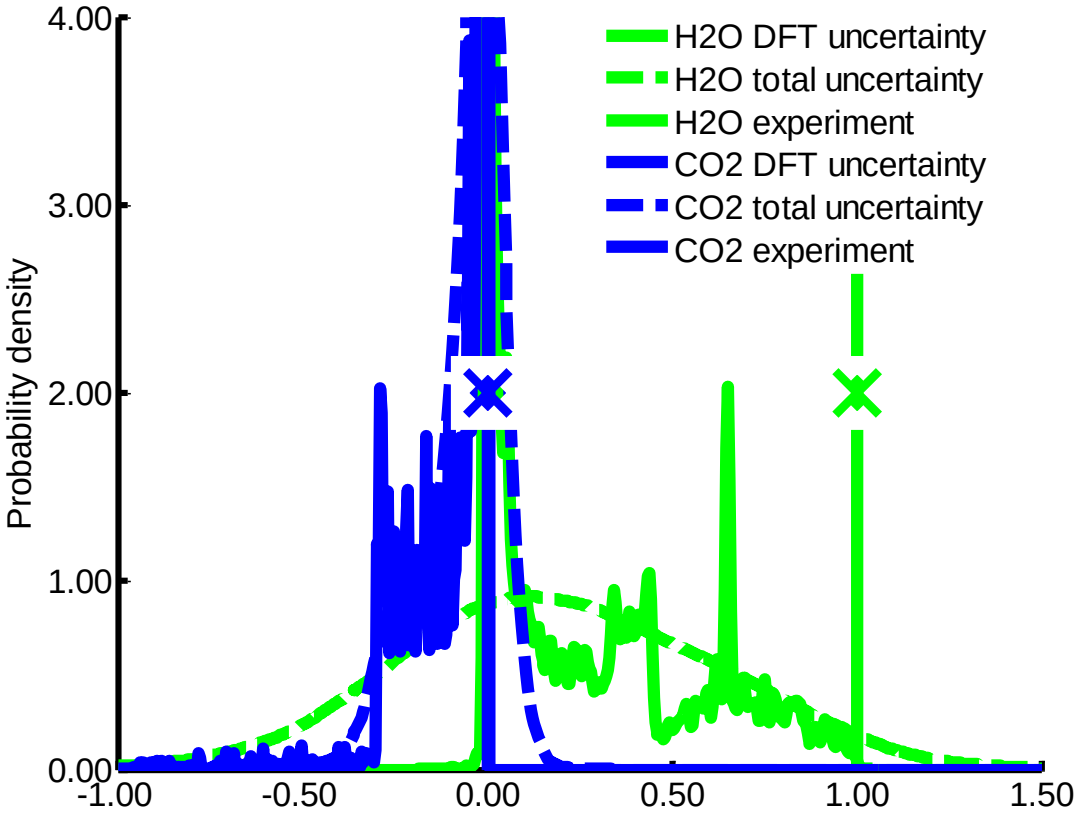

Figure A.13. Corner active site posterior reaction orders H_2O and CO_2. The experiment used for obtaining the posterior is from Kalamaras, et al.[28] which is at the conditions T=523 (K), $P_{CO} = 0.03$ (atm), $P_{H_2O} = 0.1$, $P_{CO_2} = 0.06$, $P_{H_2} = 0.2$.

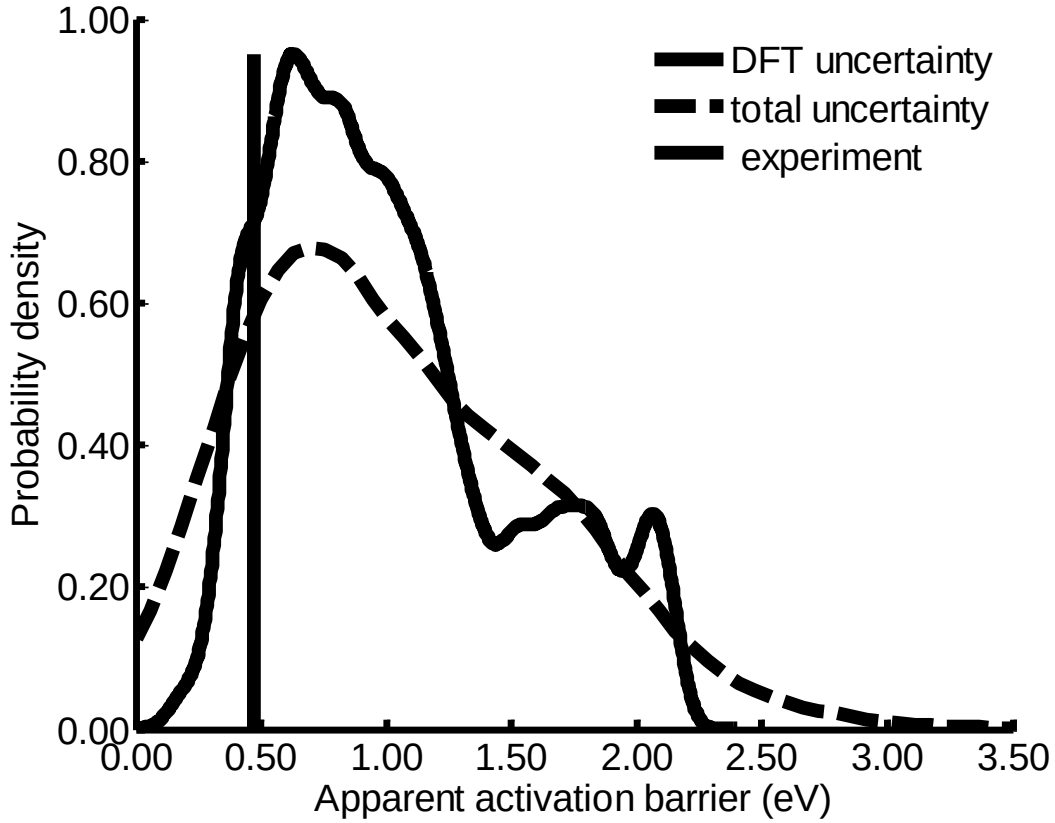

Figure A.14. Corner active site posterior apparent activation barrier (eV). The experiment used for obtaining the posterior is from Kalamaras, et al.[28] which is at the conditions T=523 (K), $P_{CO} = 0.03$ (atm), $P_{H_2O} = 0.1$, $P_{CO_2} = 0.06$, $P_{H_2} = 0.2$.

A.6 ALTERING GAS MOLECULE CORRECTION RANGE

In order to form a dirichlet probability density function for correcting thermodynamics as performed by Heyden, et al.[15], a range is necessary to set on the individual gas molecule corrections. Therefore, on the selected active site model, the edge active site, different gas molecule ranges are evaluated. The range $-0.6 \leq \zeta \leq 0.6\ (eV)$ was finally chosen. For the range $-0.2 \leq \zeta \leq 0.2\ (eV)$ the evidence is 1.23943e-05. Figures A.15-A.17 are the results with this range of gas molecule corrections for the edge active site. For the range $-0.6 \leq \zeta \leq 0.6\ (eV)$ the evidence is 0.00129728. Figures A.18-A.20 are the results with this range of gas molecule corrections. No qualitative change in conclusions results from a change in gas molecule correction range.

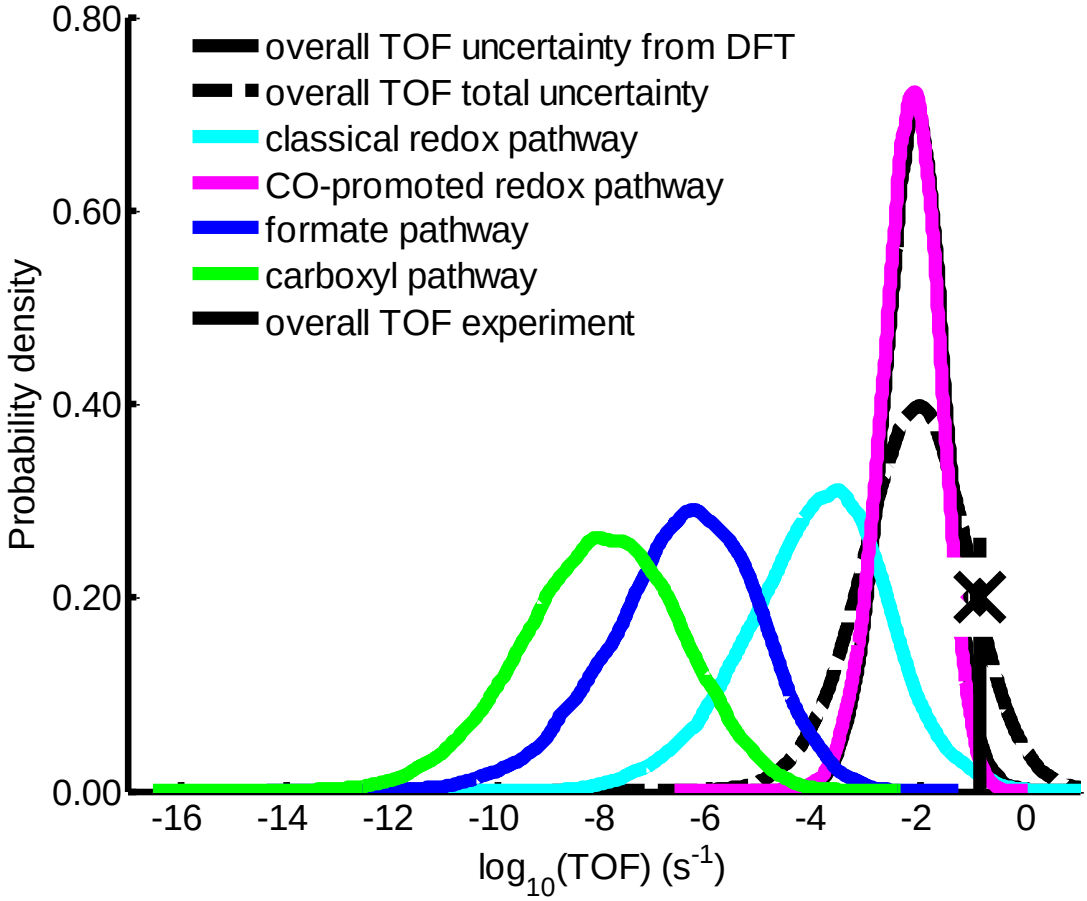

Figure A.15. TOF (s^{-1}) after Bayesian inverse using the gas molecule range $-0.2 \leq \zeta \leq 0.2\ (eV)$.

(a)

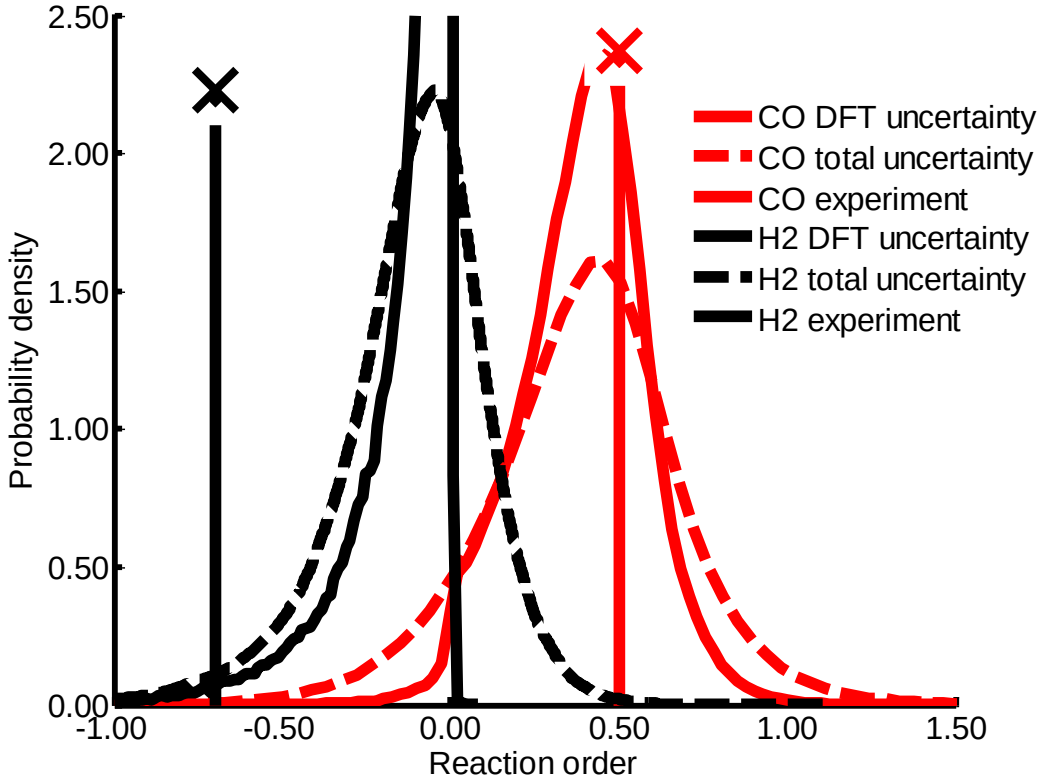
2.50
2.00
1.50
1.00
0.50
0.00
Probability density
-1.00
-0.50
0.00
0.50
1.00
1.50
Reaction order
CO DFT uncertainty
CO total uncertainty
CO experiment
H2 DFT uncertainty
H2 total uncertainty
H2 experiment

(b)

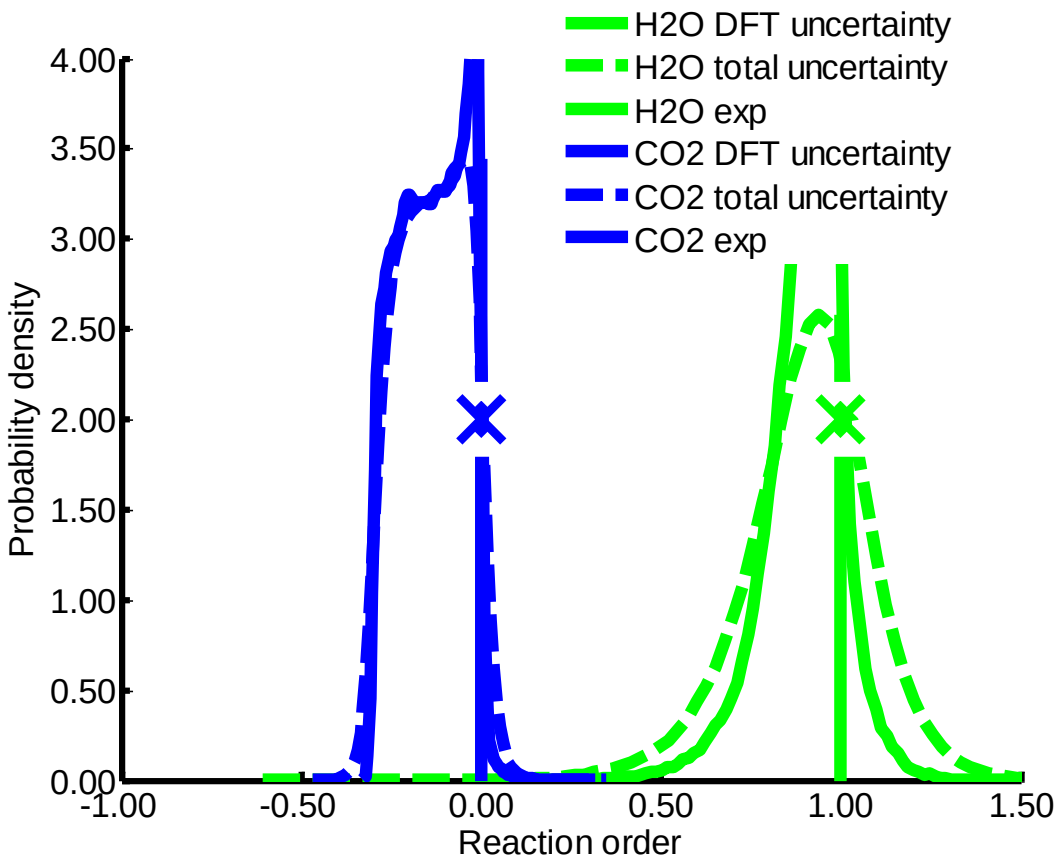

Figure A.16. Reaction orders after Bayesian inverse using the gas molecule correction range $-0.2 \leq \zeta \leq 0.2$ (eV).

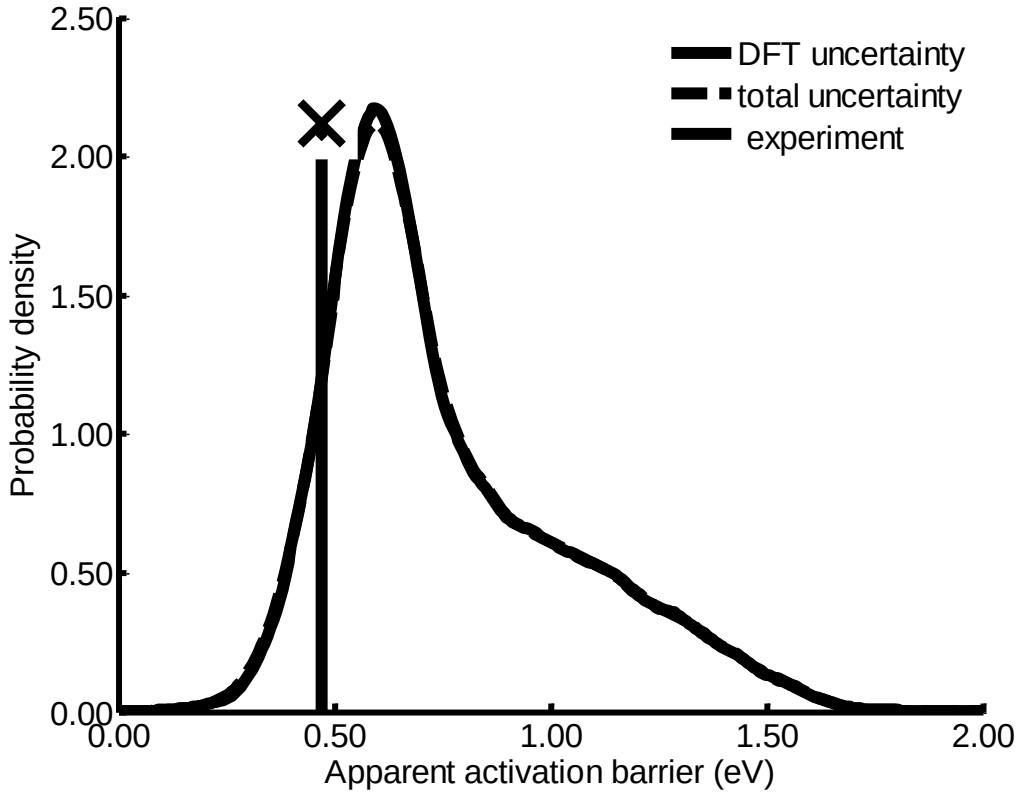

Figure A.17. Apparent activation barrier (eV) after Bayesian inverse using the gas molecule correction range $-0.2 \leq \zeta \leq 0.2$ (eV).

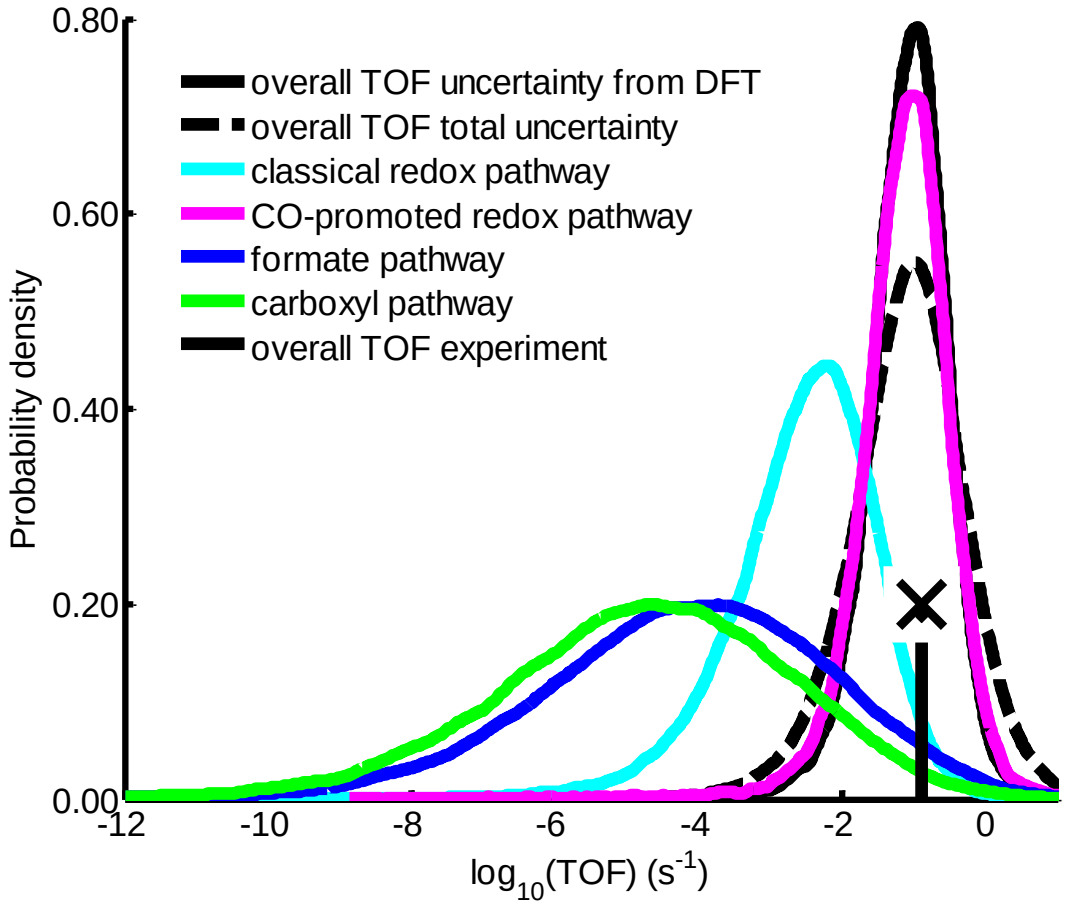

Figure A.18. TOF (s^{-1}) after Bayesian inverse using the gas molecule correction range $-0.6 \leq \zeta \leq 0.6\ (eV)$.

(a)

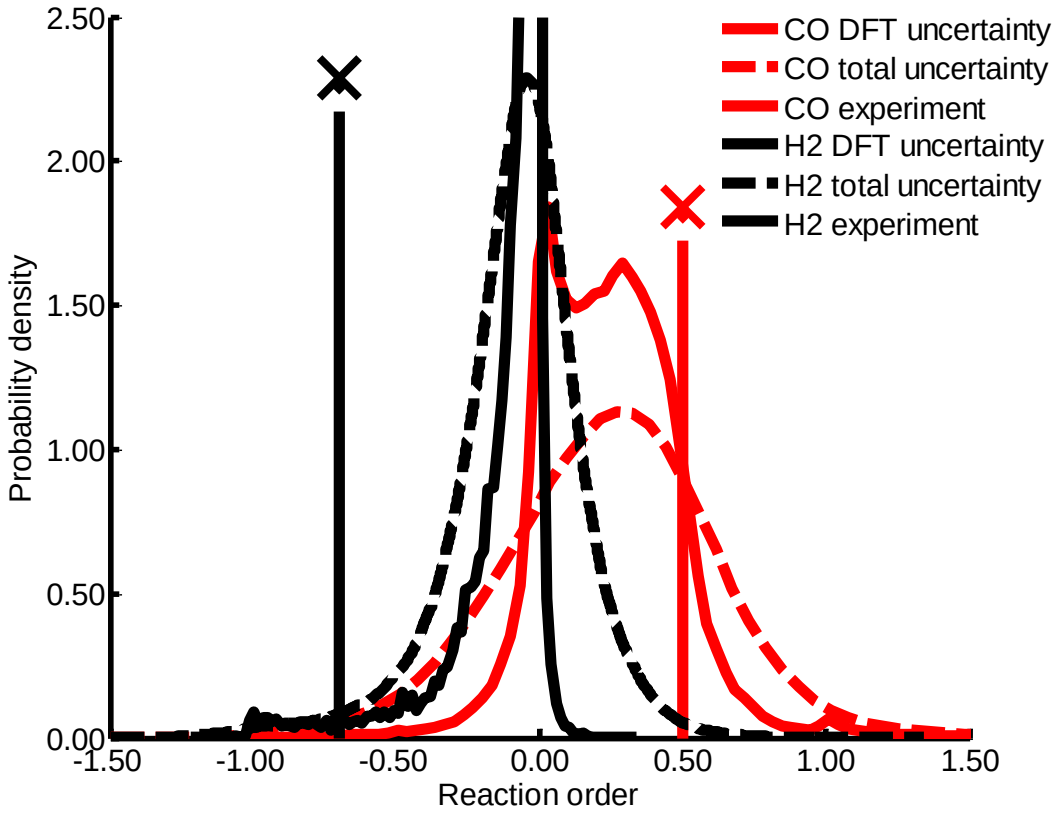
CO DFT uncertainty
CO total uncertainty
CO experiment
H2 DFT uncertainty
H2 total uncertainty
H2 experiment
Probability density
2.50
2.00
1.50
1.00
0.50
0.00
-1.50
-1.00
-0.50
0.00
0.50
1.00
1.50
Reaction order

(b)

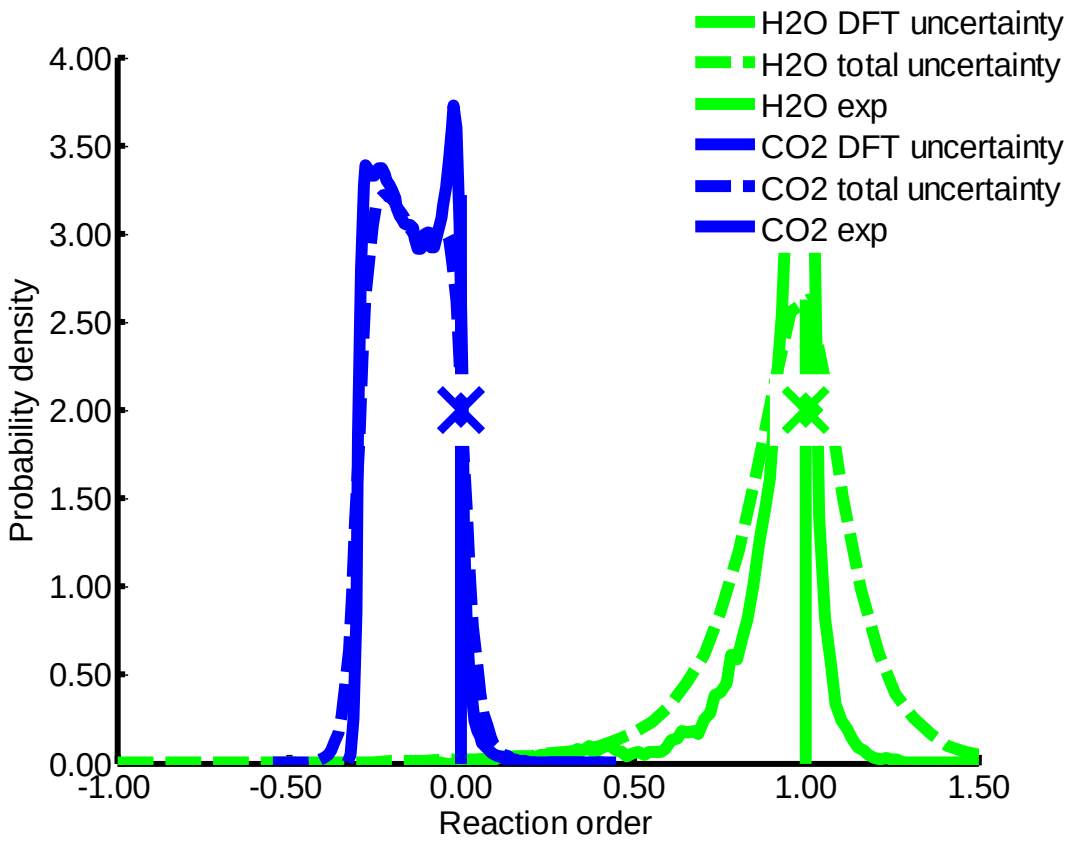

Figure A.19. Reaction orders after Bayesian inverse using the gas molecule correction range $-0.6 \leq \zeta \leq 0.6\ (eV)$.

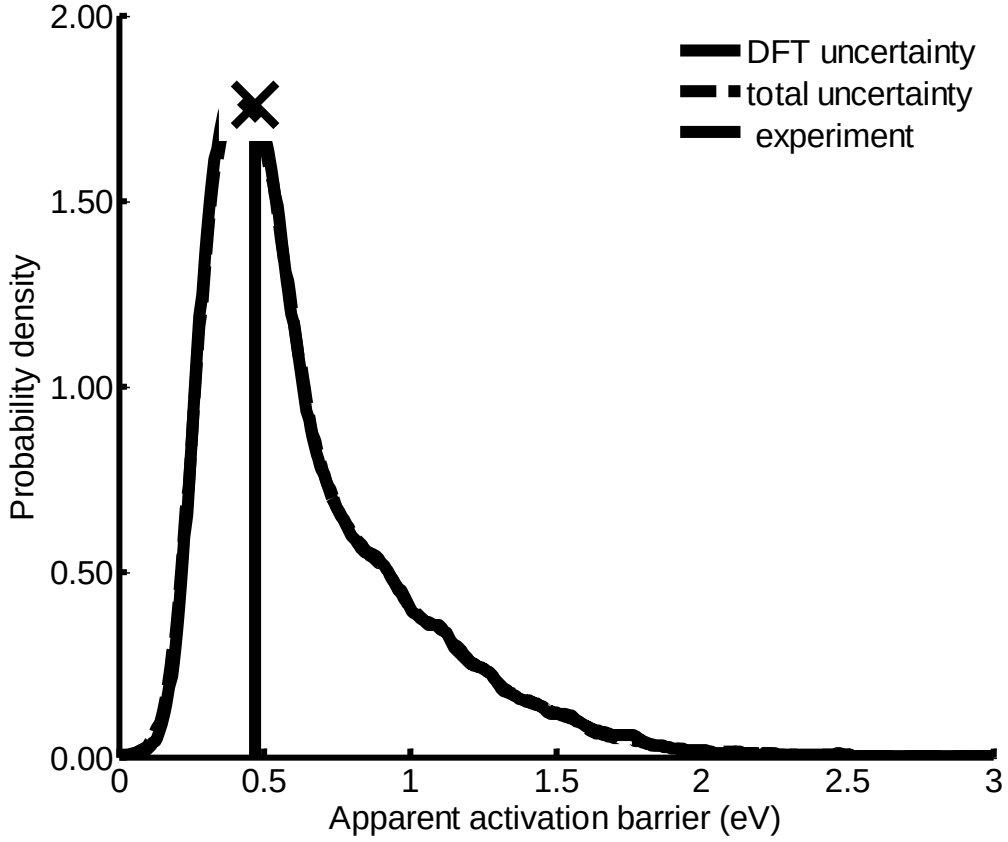

Figure A.20. Apparent activation barrier (eV) after Bayesian inverse using the gas molecule correction range $-0.6 \leq \zeta \leq 0.6\ (eV)$.

A.7 ORDER OF DATA POINTS FOR BAYESIAN INVERSE

In order to select models, Jeffreys scale[29] shown in Table A.7 is used. Due to the dependence of the model evidence on the prior model error settings, combinations of the three experimental data points are used in different orders and the evidences are listed in Tables A.8-A.10. One experimental set of data is used to gain a prior model error which is at first uninformative (inverse gamma $\alpha = 3$, $\beta = 4$ for $\log_{10}$TOF, $\beta = 0.4$ for reaction orders, $\beta = 0.8$ for apparent activation barrier (eV)). A second experimental data point is used to compute the evidence using the prior from the first experimental data point. This sequential evidence calculation may be achieved with

$$p(\theta|D_1) = \frac{p(D_1|\theta)p(\theta)}{p(D_1)} \tag{S31}$$

$$p(\theta|D_2, D_1) = \frac{p(D_2|\theta_1, D_1)p(\theta|D_1)}{p(D_2|D_1)} \tag{S32}$$

$$p(\theta|D_2, D_1) = \frac{p(D_2, D_1|\theta)p(\theta)}{p(D_2, D_1)} \tag{S33}$$

$$p(D_2, D_1|\theta) = p(D_2|\theta)p(D_1|\theta) \tag{S34}$$

$$p(\theta|D_2, D_1) = \frac{p(D_2|\theta, D_1)p(D_1|\theta)p(\theta)}{P(D_2, D_1)} \tag{S35}$$

$$p(\theta|D_2, D_1) = \frac{p(D_2|\theta, D_1)p(\theta|D_1)p(D_1)}{p(D_2 D_1)} \tag{S36}$$

$$p(\theta|D_2, D_1) = \frac{p(D_2|\theta, D_1)p(\theta|D_1)}{\frac{P(D_2, D_1)}{p(D_1)}} \tag{S37}$$

$$p(D_2|D_1) = \frac{p(D_2, D_1)}{p(D_1)} \tag{S38}$$

Table A.7. Jeffreys scale for Bayes factors.[29]

B_{12}	Evidence against M_2
1-3.2	Not worth more than a bare mention
3.2-10	Positive
10-100	Strong
>100	Very Strong

Table A.8. Edge evidences

$p(D_2, D_3)$	1.30553×10^{-06}
$p(D_2)$	2.1922×10^{-04}
$p(D_3)$	9.7553×10^{-04}
$p(D_1, D_3)$	1.85539×10^{-06}
$p(D_1)$	5.9889×10^{-03}
$p(D_1, D_2)$	1.3125×10^{-06}

Table A.9. Corner evidences.

$p(D_2, D_3)$	5.131×10^{-06}
$p(D_2)$	3.410×10^{-03}
$p(D_3)$	5.029×10^{-03}
$p(D_1, D_3)$	3.374×10^{-06}
$p(D_1)$	6.117×10^{-03}
$p(D_1, D_2)$	5.651×10^{-06}

Table A.10. Bayes factor between edge and corner for different order Bayesian inverse.

	Corner	**Edge**	**Bayes factor edge against corner**
$\boldsymbol{p(D_3\|D_2)}$	1.50×10^{-03}	5.96×10^{-03}	3.96
$\boldsymbol{p(D_2\|D_3)}$	1.02×10^{-03}	1.34×10^{-03}	1.31
$\boldsymbol{p(D_3\|D_1)}$	5.52×10^{-04}	3.10×10^{-04}	0.56
$\boldsymbol{p(D_1\|D_3)}$	6.71×10^{-04}	1.90×10^{-03}	2.83
$\boldsymbol{p(D_2\|D_1)}$	9.24×10^{-04}	2.19×10^{-04}	0.24
$\boldsymbol{p(D_1\|D_2)}$	1.66×10^{-03}	5.99×10^{-03}	3.61

A.8 REFERENCES

[1] Grabow, L. C., Gokhale, A. A., Evans, S. T., Dumesic, J. A., Mavrikakis, M. *J. Phys. Chem. C.* Mechanism of the Water Gas Shift Reaction on Pt: First Principles, Experiments, And Microkinetic Modeling. **112**, 4608-4617 (2008).

[2] Perdew, J. P., Burke, K., Ernzerhof, M. Generalized Gradient Approximation Made Simple. *Phys. Rev. Lett.* **77**, 3865-3868 (1996).

[3] Kresse, G., Hafner, J. Abinitio Molecular-Dynamics for LiquidMetals. *Phys. Rev. B: Condens. Matter Mater. Phys.* **47**, 558−561 (1993).

[4] Kresse, G., Furthmuller, J. Efficiency of Ab-Initio Total Energy Calculations for Metals and Semiconductors Using a Plane-Wave Basis Set. *Comput. Mater. Sci.* **6**, 15−50 (1996).

[5] Henkelman, G., Uberuaga, B. P., Jonsson, H. A Climbing Image Nudged Elastic Band Method for Finding Saddle Points and Minimum Energy Paths. *J. Chem. Phys*. **113**, 9901 (2000).

[6] Heyden, A., Bell, A. T., Keil, F. J. Efficient Methods for Finding Transition States in Chemical Reactions: Comparison of Improved Dimer Method and Partitioned Rational Function Optimization Method. *J. Chem. Phys*. **123**, 224101 (2005).

[7] Olsen, R. A., Kroes, G. J., Henkelman, G., Arnaldsson, A., Jonsson, H. Comparison of Methods for Finding Saddle Points without Knowledge of the Final States. *J. Chem. Phys.***121**, 9776-9792 (2004).

[8] Kozuch, S., Shaik, S. A Combined Kinetic-Quantum Mechanical Model for Assessment of Catalytic Cycles: Application to Cross Coupling and Heck Reactions. *J. Am. Chem. Soc.* **128**, 3355-3365 (2006).

[9] Kozuch, S., Shaik, S. Kinetic-Quantum Chemical Model for Catalytic Cycles: The Haber Bosch Process and the Effect of Reagent Concentration. *J. Phys. Chem. A* **112**, 6032-6041 (2008).

[10] Campbell, C. T. Micro- and Macro-Kinetics: Their Relationship in Heterogeneous Catalysis. *Top. Catal.* **1**, 353−366 (1994).

[11] Campbell, C. T. Finding the Rate-Determining Step in a Mechanism - Comparing Dedonder Relations with the "Degree of Rate Control". *J. Catal.* **204**, 520-524 (2001).

[12] Stegelmann, C., Andreasen, A., Campbell, C. T. Degree of Rate Control: How Much the Energies of Intermediates and Transition States Control Rates. *J. Am. Chem. Soc.* **131**, 8077−8082 (2009).

[13] Dumesic, J. A. Reply to Finding the Rate-Determining Step in a Mechanism: Comparing DeDonder Relations with the "Degree of Rate Control" *J. Catal.* **204**, 525-529 (2001).

[14] Stamatakis, M., Vlachos, D. G. A Graph-Theoretical Kinetic Monte Carlo Framework for On-Lattice Chemical Kinetics. *J. Chem. Phys.* **134**, 214115 (2011).

[15] Walker, E., Ammal, S. C., Terejanu, G. A., Heyden, A. Uncertainty Quantification Framework Applied to the Water-Gas Shift Reaction over Pt-based Catalysts. *J. Phys. Chem C.* **120**, 10328-10339 (2016).

[16] Kullback, S., Leibler, R. A. On Information and Sufficiency. *Ann. Math. Statist.* **22**, 79-86 (1951).

[17] Terejanu, G., Upadhyay, R. R., Miki, K. Bayesian Experimental Design for the Active Nitridation of Graphite by Atomic Nitrogen. *Exp. Therm. Fluid Sci.* **36**, 178-193 (2012).

[18] J. Beck, S. Au. Bayesian Updating of Structural Models and Reliability using Markov Chain Monte Carlo Simulation. *J. Eng. Mech.* **128**, 380-391 (2002).

[19] Prudencio, E. E., Schulz, K. The parallel C++ statistical library 'QUESO': Quantification of Uncertainty for Estimation, Simulation and Optimization, Proc. of the Workshops of the Euro-Par 2011 Conference, Lecture Notes in Computer Science Series, Vol. 7155, Springer, 2011.

[20] Ching, J., Chen, Y. Transitional Markov Chain Monte Carlo Method for Bayesian Model Updating, Model Class Selection, and Model Averaging. *J. Eng. Mech.* **133**, 816-832 (2007).

[21] Prudencio, E., Cheung, S. Parallel Adaptive Multilevel Sampling Algorithms for the Bayesian Analysis of Mathematical Models. *Int. J. Uncertainty Quantification.* **2**, 215-237 (2012).

[22] Ammal, S. C, Heyden, A. Water-Gas Shift Catalysis at Corner Atoms of Pt Clusters in Contact with a TiO_2 (110) Support Surface. *ACS Catal.* **4**, 3654-3662 (2014).

[23] Huang, S. C., Lin, C. H., Wang, J. H. Trends of Water Gas Shift Reaction on Close-Packed Transition Metal Surfaces. *J. Phys. Chem. C.* **114**, 9826-9834 (2010).

[24] Hammer, B., Hansen, L. B., Norskov, J. K. Improved Adsorption Energetics within Density- Functional Theory Using Revised Perdew-Burke-Ernzerhof Functionals. *Phys. Rev. B.* **59**, 7413-7421 (1999).

[25] Zhang, Y., Yang, W. Comment on "Generalized Gradient Approximation Made Simple". *Phys. Rev. Lett.* **80**, 890 (1998).

[26] Heyd, J., Scuseria, G. E., Ernzerhof, M. Hybrid Functionals Based on a Screened Coulomb Potential. *J. Chem. Phys.* **118**, 8207 (2003).

[27] Zhao, Y., Truhlar, D. G. A New Local Density Functional for Main-Group Thermochemistry, Transition Metal Bonding, Thermochemical Kinetics, and Noncovalent Interactions. *J. Chem. Phys.* **125**, 194101 (2006).

[28] Kalamaras, C.M.; Panagiotopoulou, P.; Kondarides, D. I.; Efstathiou., A. M., *J. Catal.* **264**, 117–129 (2009).

[29] Jeffreys, H. The Theory of Probability. (Oxford University Press, 1961).

APPENDIX B – COPYRIGHT PERMISSIONS

Copyright Clearance Center RightsLink®

Home | Create Account | Help

ACS Publications
Most Trusted. Most Cited. Most Read.

Title: Mechanism of Sulfur Poisoning of Sr2Fe1.5Mo0.5O6-δ Perovskite Anode under Solid Oxide Fuel Cell Conditions

Author: Eric Walker, Salai Cheettu Ammal, Suwit Suthirakun, et al

Publication: The Journal of Physical Chemistry C

Publisher: American Chemical Society

Date: Oct 1, 2014

Copyright © 2014, American Chemical Society

LOGIN

If you're a copyright.com user, you can login to RightsLink using your copyright.com credentials. Already **a RightsLink user** or want to learn more?

PERMISSION/LICENSE IS GRANTED FOR YOUR ORDER AT NO CHARGE

This type of permission/license, instead of the standard Terms & Conditions, is sent to you because no fee is being charged for your order. Please note the following:

- Permission is granted for your request in both print and electronic formats, and translations.
- If figures and/or tables were requested, they may be adapted or used in part.
- Please print this page for your records and send a copy of it to your publisher/graduate school.
- Appropriate credit for the requested material should be given as follows: "Reprinted (adapted) with permission from (COMPLETE REFERENCE CITATION). Copyright (YEAR) American Chemical Society." Insert appropriate information in place of the capitalized words.
- One-time permission is granted only for the use specified in your request. No additional uses are granted (such as derivative works or other editions). For any other uses, please submit a new request.

BACK | CLOSE WINDOW

Copyright © 2016 Copyright Clearance Center, Inc. All Rights Reserved. Privacy statement. Terms and Conditions.
Comments? We would like to hear from you. E-mail us at customercare@copyright.com

Title: Uncertainty Quantification Framework Applied to the Water–Gas Shift Reaction over Pt-Based Catalysts

Author: Eric Walker, Salai Cheettu Ammal, Gabriel A. Terejanu, et al

Publication: The Journal of Physical Chemistry C

Publisher: American Chemical Society

Date: May 1, 2016

PERMISSION/LICENSE IS GRANTED FOR YOUR ORDER AT NO CHARGE

This type of permission/license, instead of the standard Terms & Conditions, is sent to you because no fee is being charged for your order. Please note the following:

- Permission is granted for your request in both print and electronic formats, and translations.
- If figures and/or tables were requested, they may be adapted or used in part.
- Please print this page for your records and send a copy of it to your publisher/graduate school.
- Appropriate credit for the requested material should be given as follows: "Reprinted (adapted) with permission from (COMPLETE REFERENCE CITATION). Copyright (YEAR) American Chemical Society." Insert appropriate information in place of the capitalized words.
- One-time permission is granted only for the use specified in your request. No additional uses are granted (such as derivative works or other editions). For any other uses, please submit a new request.

BACK | CLOSE WINDOW